Observation of Non-Collinear Magnetoresistance by Scanning Tunneling Spectroscopy on Skyrmions in PdFe/Ir(111)

Dissertation zur Erlangung des Doktorgrades

an der Fakultät für
Mathematik, Informatik und Naturwissenschaften
Fachbereich Physik
der Universität Hamburg

vorgelegt von

Christian Hanneken

aus Lingen (Ems)

Hamburg, 2015

Folgende Gutachter haben die Dissertation zur Annahme empfohlen:
Prof. Dr. Roland Wiesendanger
Prof. Dr. Hans-Peter Oepen

Tag der Disputation: 26.11.2015

Mitglieder der Prüfungskommission:
Prof. Dr. Michael Thorwart (Vorsitz)
Prof. Dr. Roland Wiesendanger (einfaches Mitglied)
Prof. Dr. Hans-Peter Oepen (einfaches Mitglied)
Prof. Dr. Ulrich Merkt (einfaches Mitglied)
Prof. Dr. Markus Drescher (einfaches Mitglied)

"Physics is like sex: sure, it may give some practical results,
but that's not why we do it."

attributed to Richard Phillips Feynman

Abstract

Magnetic skyrmions are non-collinear spin arrangements with an axial symmetry and a fixed rotational sense as e.g. described in [1–22]. This fixed rotational sense implies a topology leading to an elevated stability of skyrmions against external perturbations which qualifies skyrmions as potential candidates for the application in spintronic devices as e.g. described in [10, 19, 23–25]. In this work, the electronic structure of isolated magnetic skyrmions in PdFe/Ir(111) is investigated by means of *non*–spin-polarized scanning tunneling microscopy and spectroscopy, and the interaction of skyrmions with native in-layer defects, Co adatoms and Co clusters is studied [9, 26]. In the first part, the significant difference between the vacuum local density of states measured on a collinear (ferromagnetic) and a non-collinear magnetic environment (skyrmion center) is investigated. A new type of magnetoresistive effect called non-collinear magnetoresistance (NCMR) is described [26]. This effect allows the detection of a complex non-collinear spin structure without the necessity of spin-polarized electrodes similar to a change by the tunneling anisotropic magnetoresistance effect, but much larger in magnitude [27]. In the second part, a proof-of-principle type study on the interaction of skyrmions with in-layer defects, Co adatoms and Co clusters on top of the surface is performed. The controlled writing and deleting of individual skyrmions is demonstrated as well as the movement of an isolated skyrmion which is induced by moving a cluster with the tip of a scanning tunneling microscope [9]. This study demonstrates an important step towards an application of skyrmions in future devices.

Inhaltsangabe

Magnetische Skyrmionen sind nicht-kollineare Spin-Anordnungen mit einer axialen Symmetrie und einem festen Drehsinn wie z.B. in [1–22] beschrieben. Dieser Drehsinn hat eine Topologie zur Folge, welche zu einer erhöhten Stabilität von Skyrmionen gegenüber externen Störungen führt. Durch diese Eigenschaft eignen sich Skyrmionen für die zukünftige Verwendung in spintronischen Bauteilen, z.B. [10, 19, 23–25]. Im Rahmen der hier vorgelegten Arbeit wird die elektronische Struktur isolierter magnetischer Skyrmionen in PdFe/Ir(111) mit Hilfe der *nicht*–spinpolarisierten Rastertunnelmikroskopie (STM) und -spektroskopie untersucht, sowie die Wechselwirkung von Skyrmionen mit nativen Defekten innerhalb der Pd-Lage und Co Adatomen und Co Clustern auf der Pd-Lage

studiert [9, 26]. Im ersten Teil wird die Variation der lokalen Vakuumzustandsdichte von magnetischen Momenten in einer kollinearen (Ferromagnet) und einer nicht-kollinearen (Skyrmionzentrum) Umgebung untersucht. Ein neuer magnetoresistiver Effekt, genannt nicht-kollinearer Magnetowiderstand (NCMR), wird beschrieben [26]. Dieser Effekt erlaubt eine Detektion von komplexen nicht-kollinearen Spinstrukturen ohne die Verwendung von spinpolarisierten Elektroden, ähnlich dem tunnelanisotropen Magnetowiderstand (TAMR) [27]. Der zweite Teil beschreibt eine qualitative Machbarkeitsstudie über die Wechselwirkung von Skyrmionen mit Defekten in und Co Atomen und Clustern auf der Pd-Lage. Das kontrollierte Schreiben und Löschen einzelner Skyrmionen sowie die kontrollierte Bewegung eines isolierten Skyrmions mit Hilfe eines Clusters und der STM-Spitze wird gezeigt [9]. Diese Studie stellt einen wichtigen Schritt in Richtung technischer Anwendung magnetischer Skyrmionen dar.

Symbols

$\alpha_{ij}(\vec{r}, B)$	angle between nearest neighbor spins i and j
$\alpha_c(B) = \alpha_{i=c,j}(B)$	angle between the central spin c of a skyrmion and its nearest neighbor spin j
$\langle\alpha\rangle = \langle\alpha_i(\vec{r}, B)\rangle = \frac{1}{6}\sum_{j=1}^{6}\alpha_{ij}(\vec{r}, B)$	mean angle between a central moment i and its six nearest neighbors $j = 1...6$ which is used to describe the non-collinearity in this work
B_{ext}	external magnetic field, in all measurements of this work perpendicular to the surface (positive value: pointing towards the reader)
$\Delta E(\vec{r}, B)$	energy shift of the higher energy peak in the vacuum LDOS at position $\vec{r}$ and magnetic field B
$\Delta I(\vec{r}, B)$	intensity change of the higher energy peak in the vacuum LDOS at position $\vec{r}$ and magnetic field B
$\Delta I_{+700\,\mathrm{mV}}(\vec{r}, B)$	intensity change at the fixed sample bias of $+700\,\mathrm{mV}$ at position $\vec{r}$ and magnetic field B
I_{T}	tunneling current
I_{stab}	initial stabilization current before the start of a point STS measurement with an open feedback loop
$\vec{m}(\vec{r}, B)$	local spin at position $\vec{r}$ and magnetic field B
$\sigma_{<\alpha>} = \sigma_{<\alpha_i(\vec{r},B)>}$	standard deviation of $\langle\alpha\rangle$ which is used to describe the anisotropy of the non-collinearity in this work
θ	polar angle of the local magnetization relative to the surface normal
U_{B}	sample bias
U_{stab}	initial sample bias before the start of a point STS measurement with an open feedback loop

Abbreviations

1D	one dimension
2D	two dimensions
3D	three dimensions
DFT	density functional theory
DM interaction, DMI	Dzyaloshinsky-Moriya interaction
DOS	density of states
fcc-PdFe	face centered cubical stacking of Pd on fcc stacking of Fe
fcc-Fe	face centered cubical stacking of Fe
FM	ferromagnet; ferromagnetic
hcp-PdFe	hexagonal closed packed stacking of Pd on fcc stacking of Fe
LDOS	local density of states
LT-STM	low-temperature STM
NCMR	non-collinear magnetoresistance (effect)
Sk	skyrmion
SkC	skyrmion center
SP-STM	spin-polarized scanning tunneling microscopy
SpS	spin spiral
STM	scanning tunneling microscopy/microscope
STS	scanning tunneling spectroscopy
TAMR	tunneling anisotropic magnetoresistance effect
TB model	tight-binding model
TMR	tunneling magnetoresistance effect
UHV	ultra-high vacuum ($p < 1 \times 10^{-9}$ mbar)

Contents

List of Figures

1. Introduction

Over the last decades, technology has evolved with an enormous speed. A good example are today's mobile phones which are not only used for making phone calls anymore as it was their main purpose in the early 1990's, but are also used, e.g. for navigation, as a photo and video camera, a reader for electronic books, a portable game console and as a movie player. This evolution was only possible due to the advancement and miniaturization of electronics and the improvement of non-volatile memory technologies. To continue this progress, novel physical phenomena which are suitable for the employment as bit of information in future devices are needed.

One promising example are magnetic skyrmions which are particle-like non-collinear spin textures with an axial symmetry and a fixed rotational sense as e.g. described in [1–22, 28]. The concept of skyrmions was originially applied in the context of particle physics [29, 30] and was later used in many other fields of physics as e.g. in [4, 9, 11, 23, 24, 31–40] or as described in the collection in [41]. Magnetic skyrmions are distinct from the ferromagnetic background in which they are embedded due to their non-trivial topology. Their topological charge can be used as bit of information as e.g. suggested in [6, 8]. This particular topology increases the skyrmion's stability which makes it especially promising for non-volatile memory devices and spintronic applications as e.g. described in [10, 16, 19, 23–25, 42]. Up to now, magnetic skyrmions have been discovered in non-centrosymmetric bulk crystals like e.g. in MnSi as e.g. described in [4, 43–45], and ultrathin transition metal films like e.g. $Fe_{0.5}Co_{0.5}Si$, FeGe, Fe/Ir(111) and PdFe/Ir(111) as e.g. described in [5, 7, 9, 14, 35, 36, 39, 40, 46–51]. Both classes of physical systems show an inversion symmetry breaking, either due to the crystalline structure or interface induced which leads to the Dzyaloshinsky-Moriya interaction [52, 53] and which plays a crucial role in the formation of skyrmions as e.g. described in [2, 5, 7, 28, 54].

Current research on skyrmions focuses on e.g. the controlled creation and annihilation, the spatial control and the search for a simple detection scheme as e.g. described in [8–10, 15, 25, 26, 37, 38]. All these qualities represent important requirements for a future technical application. For using skyrmions as bit of information, one needs to be able to controllably create and delete and to move them from a writing to a read-out position, e.g. in racetrack-type devices as mentioned e.g. in [23–25, 42]. Several studies have demonstrated the controlled creation and annihilation of skyrmions like e.g. at edges or notches [16], by a conversion of a domain-wall pair into a skyrmion [19], by photo-irradiation [17] and by using vertical tunnel currents [9]. In addition, skyrmion movement was studied using lateral currents as e.g. described in [8, 10, 11, 43, 51]. The advantage of moving skyrmions compared to magnetic domain walls is the 5 to 6 orders of magnitude lower current density which is needed to move a skyrmion. The much lower current density makes skyrmions

highly interesting for the application in the above mentioned energy efficient racetrack-type memory devices as e.g. suggested in [8].

Over the last decades, several magnetoresistive effects were discovered and used for the detection of collinear and non-collinear magnetic states. For example, the coupling between two magnetic layers may lead to the emergence of the giant and/or tunnel magnetoresistive effect (GMR and TMR) [55–58] or the (tunnel) anisotropic magnetoresistance effect (T)AMR [59–61] which is a consequence of spin-orbit coupling and is directly linked to the material properties. Besides these effects, electron transport measurements through (non-collinear) magnetic domain walls also show a resistive effect and lead to a different value compared to the FM case as e.g. studied in [62–65]. However, due to the averaging nature of the measurements, neither contributing effects can be discriminated nor the role of the magnetic non-collinearity can exactly be determined. Besides these magnetoresistive effects, skyrmions have been studied with various techniques like e.g. Lorentz microscopy as e.g. described in [35, 39, 50, 51], neutron scattering experiments as e.g. used in [4, 44, 45], or spin-polarized scanning tunneling microscopy (SP-STM) and scanning tunneling spectroscopy (STS) as e.g. described in [7, 9, 14, 26, 66]. Especially the last two techniques present powerful tools due to their high spatial resolution capabilities and the large variety of accessible sample properties as e.g. described in [67], section 1.13, pages 142-157, and [68], chapter 14, pages 295-312: (SP-)STS allows spectroscopic studies with a high energy and spatial resolution on the surface and can easily access the LDOS of the sample as e.g. in [69, 70]. In addition, SP-STM is capable of performing detailed studies on non-collinear spin structures as e.g. described in [7, 13, 58, 66, 71–79]. A unique ability of the STM is the precise movement and positioning of single atoms or clusters as e.g. in [80–85], and the STM tip can even be used to induce chemical reactions on the single molecular level as e.g. studied in [86–88]. These atom manipulation capabilities can be combined with (SP-)STM and (SP-)STS measurements and allow a wide range of unique experiments at the atomic level as e.g. investigated in [83–85, 89–94].

The variety of features of (SP-)STM and STS motivate the employment of these techniques for the study of skyrmions in this work. Chapter 2 starts with a brief characterization of skyrmions followed by the description of the physical effects which lead to the formation of skyrmions. A short review of (SP-)STM and STS is given together with a brief description of the physical system PdFe/Ir(111) which was used during this entire study. Chapter 3 describes the instrumental setup and the preparation method of the ultrathin film system. Chapter 4 presents the results of spatially resolved STS measurements on both skyrmions and the spin spiral and reports on the discovery of a new type of magnetoresistive effect which is called non-collinear magnetoresistance (NCMR). Chapter 5 presents a proof-of-principle type study on the pinning of isolated skyrmions to defects within the surface and adatoms and clusters on top of the surface. The controlled writing and deleting of skyrmions is demonstrated as well as the distortion of the skyrmion shape and the controlled movement of an isolated skyrmion by the assistance of an adsorbate. Finally, chapter 6 summarizes the results and discusses their future implications.

2. A brief theoretical introduction

This section gives a short characterization of magnetic skyrmions and the interactions which lead to their formation in PdFe/Ir(111). In addition, the fundamental principles of scanning tunneling microscopy and spectroscopy are briefly described. Finally, the main properties of PdFe/Ir(111) are presented. More detailed explanations of the magnetic interactions and scanning tunneling microscopy can be found in standard text books, like e.g. [67, 68, 95, 96].

2.1. Magnetic skyrmions

The theoretical concept of skyrmions was developed by Tony Skyrme in 1961 [29, 30] in the framework of particle physics and later on transfered to other fields of physics like e.g. cosmology [33], Bose-Einstein condensates [31], electron gases [32] and non-collinear magnetism as e.g. described in [4, 9, 11, 23, 24, 34–40]. In the context of magnetism, skyrmions are particle-like, localized spin arrangements with a fixed rotational sense and an axial symmetry as e.g. described in [1–22, 28]. Magnetic skyrmions have been found in various systems like e.g. in MnSi as e.g. studied in [4, 36, 44, 45], $Fe_{1-x}Co_xSi$ as e.g. in [5, 34], FeGe as e.g. in [35, 47], Fe/Ir(111) [7, 66] and PdFe/Ir(111) as e.g. in [9, 14, 26] in both bulk and thin films. Furthermore, these studies have been performed using a broad variety of experimental techniques like, e.g. neutron scattering as e.g. used in [4, 43, 45], electron holography as studied in [46], short optical laser pulses as in [17], Lorentz transmission electron microscopy (Lorentz TEM) as e.g. in [5, 39, 48, 50, 51] and spin-polarized scanning tunneling microscopy (SP-STM) as e.g. used in [7, 9, 14, 26, 66]. The main focus in these studies are the creation of skyrmions as studied e.g. in [9, 10, 15], their movement as e.g. investigated in [8, 10, 24, 25, 39, 43, 51] and their potential application in e.g. racetrack devices as e.g. in [23, 24]. The physical origin of magnetic skyrmions is typically a competition between the Heisenberg exchange interaction, which usually tries to align all magnetic moments parallel, and the Dzyaloshinsky-Moriya interaction (DMI), which tries to align the moments perpendicularly, e.g. see [1–3, 54]. The Dzyaloshinsky-Moriya interaction itself is a consequence of a strong spin-orbit coupling and becomes relevant in systems with a lack of inversion symmetry as it is found in non-centrosymmetric bulk crystals or at interfaces and surfaces [8, 52, 53, 97]. In addition, the DMI implies a fixed rotational sense to the spin texture, thereby leading to an energy barrier between the complex spin state and the FM state. This energy barrier is infinite in continuous systems which leads to a true topological protection of the skyrmion; the skyrmion can not be continuously unwind and destroyed in this case [2]. If the magnetization within a skyrmion is discrete as it is on an atomic lattice, the energy barrier is finite. External perturbations, like e.g. an external magnetic field can

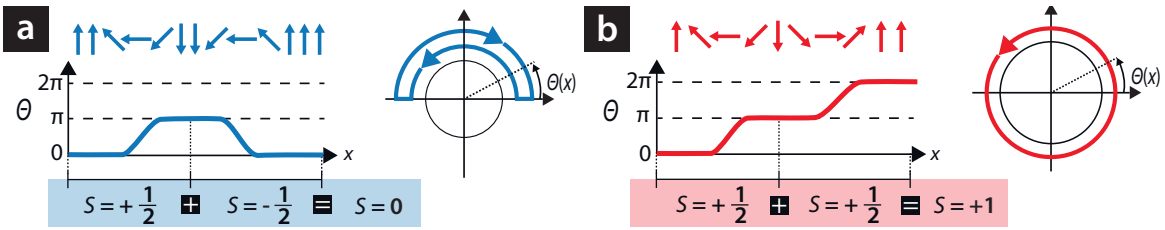

Figure 2.1.: Schematic illustrating the topology of a 1D spin system. **a**, Dependence of the polar angle θ on the distance of two 180° domain walls with opposite rotational sense. With increasing distance, θ gains and loses an additional phase of 180°. **b**, Same as **a**, but for two domain walls with the same rotational sense as it is the case along a symmetry direction of a 2D skyrmion. In contrast to **a**, θ gains an additional phase of 360° in **b**. The sketch is according to Fig. 0.1 of [98].

destroy a skyrmion once the energy barrier is overcome [1]. The topological winding can be characterized by the skyrmion number S [3]

$$S = \frac{1}{4\pi}\int_A \vec{m}(\vec{r})\cdot\left(\frac{\partial\vec{m}(\vec{r})}{\partial x}\times\frac{\partial\vec{m}(\vec{r})}{\partial y}\right)\mathrm{d}\vec{r} \tag{2.1}$$

$$\overset{1D}{=} \frac{1}{2\pi}\int_C \frac{\mathrm{d}\theta}{\mathrm{d}x}\mathrm{d}x \tag{2.2}$$

with $\vec{m}(\vec{r})$ as the normalized local magnetization, θ as the polar angle of the magnetization and the integration extends over the whole skyrmion's surface A and length C, respectively. The spin rotation within the skyrmion can be simply explained for the 1D case as illustrated in Fig. 2.1. In case of two 180° domain walls with opposite rotational sense, the spins within the domain walls gain and subsequently lose an additional phase of 180°, the total phase shift amounts to 0° and therefore the skyrmion number results to $S = 0$ (cf. Fig. 2.1 **a**). This is different for two domain walls with the same rotational sense which is the representation of a 2D skyrmion along one of its symmetry directions (cf. Fig. 2.1 **b**). With increasing distance, the spins pick up an additional phase which is 360° in total, and therefore $S = 1$.

2.2. Magnetic interactions

The system of PdFe on Ir(111) can be described by the Hamiltonian

$$H = H_{\mathrm{exch}} + H_{\mathrm{DM}} + H_{\mathrm{MA}} + H_{\mathrm{Zeem}} \tag{2.3}$$

with H_{exch} as the Heisenberg exchange interaction, H_{DM} the Dzyaloshinsky-Moriya interaction, H_{MA} the magnetic anisotropy and H_{Zeem} as the Zeeman energy [12]. The terms are shortly explained in the following. Further information can be found in [12, 95, 96, 99].

2.2.1. Heisenberg exchange interaction

The Heisenberg exchange interaction results from the interplay between the electrostatic Coulomb force and the quantum mechanical Pauli exclusion principle as described e.g. in [95], section 4.2.1 on pages 74-76. The Coulomb force tries to separate two electrons due to their like charge, the Pauli exclusion principle states that no indistinguishable identical fermions like, e.g. electrons can be identical in all quantum numbers. As a consequence, two electrons can not be at the same position in space with the same spin orientation. The simplest case are two free electrons. Their total joint wave function needs to be anti-symmetric. This means that the spins of two electrons are either anti-parallel and close together (antisymmetric spin part and symmetric spatial part of the joint wave function), or the two electron spins align parallel in which case the electrons need to be spatially separated (symmetric spin part and antisymmetric spatial part of the joint wave function). The quantity which describes which of the two states is favored is the exchange integral J which is defined as the difference between the energy of the singlet state E_{S} (symmetric spatial state) and the energy of the triplet state E_{T} (anti-symmetric spatial state)

$$J = \frac{E_{\mathrm{S}} - E_{\mathrm{T}}}{2}. \tag{2.4}$$

The exchange integral describes whether the coupling is anti-ferromagnetic ($J>0$) or ferromagnetic ($J<0$). Using the exchange integral, the Hamiltonian for two spins $\vec{m}_1$ and $\vec{m}_2$ is given by

$$H_{\mathrm{exch}} = -2J\vec{m} \cdot \vec{m}_2 \tag{2.5}$$

which becomes

$$H_{\mathrm{exch}} = -\sum_{i,j} J_{ij}\vec{m}_i \cdot \vec{m}_j \tag{2.6}$$

if H_{exch} is generalized to a many-body system with $\vec{m}_i$ and $\vec{m}_j$ as the ith and jth spin and J_{ij} the exchange integral between atom i and j [95], section 4.2.1 on pages 74-76. In case of PdFe/Ir(111), the exchange interaction favors a parallel alignment of the magnetic moments [12].

2.2.2. Dzyaloshinsky-Moriya interaction

The Dzyaloshinsky-Moriya interaction (DMI) is a consequence of a large spin-orbit coupling and an inversion symmetry breaking as it occurs in non-centrosymmetric crystals or at interfaces involving a heavy element [8, 52, 53, 97]. In PdFe/Ir(111) the interface between

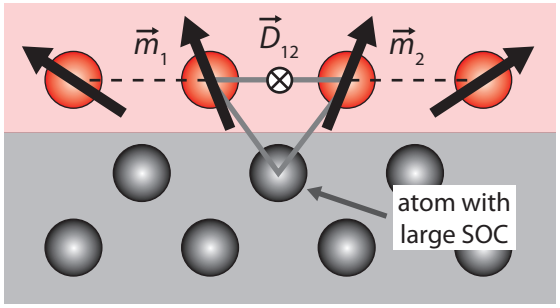

Figure 2.2.: Schematic illustrating interfacial DMI. The magnetic moments of two atoms in the top layer (red) are indirectly coupled by an atom with a large spin-orbit coupling (grey). The resulting DM vector $\vec{D}_{12}$ points away from the reader. The sketch is according to [8].

Fe and Ir contributes the most to the DMI in this system [12]. The physical origin is an indirect three-site exchange mechanism which involves two magnetic moments m_1 and m_2 and an atom with a large spin-orbit coupling as shown in Fig. 2.2 [8, 97]. The corresponding first order Hamiltonian H_{DM} is given by

$$H_{\mathrm{DM}} = -\sum_{ij} \vec{D}_{ij} \left(\vec{m}_i \times \vec{m}_j\right) \tag{2.7}$$

with the strength of the DM interaction D_{ij} between moment $\vec{m}_i$ and $\vec{m}_j$ at positions $\vec{r}_i$ and $\vec{r}_j$, respectively, and the sum extending over all atoms i and j. In the case of PdFe/Ir(111), the DM vector D_{ij} lies in the surface plane [12]. According to this expression, the energy is minimized if two neighboring moments are perpendicular to each other.

2.2.3. Magnetocrystalline anisotropy

The magnetocrystalline anisotropy is the result of the coupling of electrons to the surrounding electric field. This so called crystal field arises from the charge of the electrons in the orbitals of the surrounding atoms. The crystal field's symmetry therefore reflects the crystalline structure. Due to spin-orbit coupling, the magnetic moments of the electron is tied to the crystal field and therefore to the crystal symmetry as e.g. described in [95], section 6.7.2, pages 128-129 and section 3.1.2, pages 48-50. In the simplest case of a uniaxial anisotropy and its treatment in the first order, the energy is minimized if the magnetic moments are aligned along the so called easy axis of the anisotropy

$$H_{\mathrm{MA}} = \sum_i K \left(m_i^z\right)^2 \tag{2.8}$$

with K as the uniaxial magnetocrystalline anisotropy constant, m_i^z the z-component of the i-th moment due to an easy axis along z (perpendicular to the surface) and the sum running

over all moments i. For the case of PdFe/Ir(111), the magnetocrystalline anisotropy tends to align the magnetic moments perpendicular to the surface [12].

2.2.4. Zeeman energy

The Zeeman effect describes the change of an electron's energy levels in an external magnetic field. As a consequence, the electron spin aligns to the magnetic field. The Zeeman contribution for spins in a magnetic field along the z-axis is given by

$$H_{\mathrm{Zeem}} = -\sum_i B\, m_i^{\mathrm{z}} \tag{2.9}$$

with m_i^{z} as the z-component of the i-th spin in an external magnetic field with strength B which is oriented along the z-axis (perpendicular to the surface) and the sum extends over all magnetic moments i.

2.3. Scanning tunneling microscopy techniques

This section briefly describes the fundamental principles of scanning tunneling microscopy (STM) and its different modes of operation like scanning tunneling spectroscopy (STS) and atom manipulation. In addition, the relevant effects which are important for the understanding and interpretation of spin-polarized STM data are briefly explained. Further information can be found in standard text books e.g. in [67, 68].

2.3.1. Scanning tunneling microscopy (STM)

The scanning tunneling microscope was invented by Binnig und Rohrer [100]. Its underlying physical effect is the quantum mechanical tunnel effect. This effect enables the electron wave function to penetrate a potential barrier which would be classically forbidden. The theoretical concept of the tunnel effect was first used in planar tunnel junctions [101] and later on applied to an STM geometry using different approximations of the tip wave function [102–105]. In the common Tersoff-Hamann model, the tunnel current is given to first order for low temperatures and low bias for an s-type tip wave function by

$$\begin{aligned} I(E_{\mathrm{F,s}}) &\propto U \rho_{\mathrm{t}} \mathrm{e}^{2\kappa R} \cdot \sum_a |\psi_a(\vec{r}_{\mathrm{t}})|^2\, \delta(E_a - E_{\mathrm{F,s}}) \\ &\propto U \rho_{\mathrm{t}} \mathrm{e}^{2\kappa R} \cdot \rho_{\mathrm{s}}(\vec{r}_{\mathrm{t}}, E_{\mathrm{F,s}}) \end{aligned} \tag{2.10}$$

with $\vec{r}_\mathrm{t}$ as the position of the tip apex with radius R, U as the sample bias, $\rho_\mathrm{t} = \rho_\mathrm{t}(E_\mathrm{F,s})$ as the tip LDOS, $\rho_\mathrm{s}(\vec{r}_\mathrm{t}, E_\mathrm{F,s}) = \sum_a |\psi_a(\vec{r}_\mathrm{t})|^2 \, \delta(E_a - E_\mathrm{F,s})$ as the sample LDOS with $\psi_a(\vec{r}_t)$ as the wave function of sample atom a, the sum runs over all atoms a, and $E_\mathrm{F,s}$ as the sample's Fermi energy [103]. Equation 2.10 states that the tunnel current is directly proportional to the integrated LDOS of the sample. Since the sample wave function decays exponentially into the vacuum, one can substitute $|\psi_a(\vec{r}_\mathrm{t})|^2 \propto \mathrm{e}^{-2\kappa(R+d)}$ in Eq. 2.10. Now, the tunnel current becomes

$$I \propto \mathrm{e}^{-2\kappa d} \tag{2.11}$$

with the inverse decay length $\kappa = \sqrt{2m\phi/\hbar^2}$ of electrons with mass m and work function Φ, $\hbar$ as the reduced Planck constant and and the distance d between tip and surface [103]. This exponential dependence of the tunnel current on the tip-sample distance allows a high spatial resolution down to the sub-atomic level.

The STM can be operated using different imaging modes. The most common mode is the constant-current mode, which was used during this entire study for imaging the surface as e.g. described in [67], section 1.11.1, pages 109-128: while moving the tip along the surface, the tunnel current is continuously measured and compared to a set point of a feedback loop. A deviation of the measured tunnel current from the set point leads to a change of the distance between tip and sample. If the current is too low, the tip is approached, if the current is too high, the tip is retracted. The constant-current mode prevents the tip apex from a mechanical contact with the surface. Referring to Eq. 2.10, the constant-current mode images a contour map of constant surface LDOS in the vacuum which is typically interpreted as the topography of the surface [103]. A different operational mode is the constant-height mode which keeps the tip-sample distance fixed and measures the spatial variation of the tunnel current as e.g. described in [67], section 1.11.1, pages 128-130. If the tip height is not carefully chosen in the constant-height mode, the tip might potentially crash into a surface protrusion which should be avoided. This is why the constant-current mode is typically favored over the constant height mode.

2.3.2. Spin-polarized STM

Section 2.3.1 gives a definition of the tunnel current I_T which solely depends on the LDOS of the tip and the sample and the applied sample bias. If both sample and tip are magnetic, i.e. both show a spin-polarization around E_F, the definition of the tunnel current needs to be extended by the contributions from the tunneling magnetoresistance effect (TMR) I_SP and the tunneling anisotropic magnetoresistance effect (TAMR) I_TAMR. In the independent orbital approximation, [68], section 6.4, pages 159-163, the tunnel current is [27, 106]

$$
\begin{aligned}
I_{\mathrm{SPSTM}}(\vec{r}_{\mathrm{t}}, U) &= I_{\mathrm{T}}(\vec{r}_{\mathrm{t}}, U) + I_{\mathrm{SP}}(\vec{r}_{\mathrm{t}}, U) + I_{\mathrm{TAMR}}(\vec{r}_{\mathrm{t}}, U) \\
&\propto \sum_a [1 + P_{\mathrm{t}}(E_{\mathrm{F,t}}) P_{\mathrm{s}}(E_{\mathrm{F,s}} + eU) \cos(\alpha_a) \\
&\qquad + \gamma f(\Phi_a, \theta_a)] \cdot \mathrm{e}^{(-2\kappa|\vec{r}_{\mathrm{t}} - \vec{r}_a|)}
\end{aligned} \tag{2.12}
$$

with $\vec{r}_{\mathrm{t}}$ and $\vec{r}_a$ as the positions of tip and surface atom a, $P_{\mathrm{t}}(E_{\mathrm{F,t}})$ and $P_{\mathrm{s}}(E_{\mathrm{F,s}} + eU)$ as the sample bias dependent tip and sample polarizations, α_a the angle between the tip and the surface atom magnetization directions, θ_a and Φ_a as the polar and azimuth angle of the spin of atom a relative to the spin quantization axis, respectively, $\kappa = \sqrt{2m\phi/\hbar^2}$ as the inverse decay length with m as the electron mass, ϕ as the work function of the surface and $\hbar$ as the reduced Planck constant. The additional terms I_{SP} and I_{TAMR} will be explained in the following.

Tunneling magnetoresistance effect (TMR)

The tunneling magnetoresistance effect (TMR) characterizes the resistance between two ferromagnets which are separated by a thin insulator through which electrons can tunnel from one ferromagnet to the other [57]. In the simplest case of the same DOS for both ferromagnets, a parallel magnetization of the ferromagnets leads to a low resistance. If the magnetizations are anti-parallel, the resistance is large as e.g. in [57, 107]. The physical reason is as follows: the exchange interaction of the ferromagnets leads to a spin-split density of states (DOS) with a non-zero spin polarization at the Fermi energy as shown in Fig. 2.3 for the case of the same electrode's DOS. The spin-polarization P is defined as

$$
P(E) = \frac{\rho_\uparrow(E) - \rho_\downarrow(E)}{\rho_\uparrow(E) + \rho_\downarrow(E)} \tag{2.13}
$$

with $\rho_\uparrow(E)$ and $\rho_\downarrow(E)$ as the energy E dependent DOS of the spin-$\uparrow$ and spin-$\downarrow$ channel. If a sample bias U is applied, electrons tunnel through the insulating barrier from one electrode into another. This tunnel current strongly depends on the spin orientation: assuming the conservation of spin, only $\uparrow$-electrons can tunnel into $\uparrow$-states and $\downarrow$-electrons can only tunnel into $\downarrow$-states. If the magnetizations of the electrodes are parallel (and no polarization inversion is present at E_{F} of the sample), many electrons with the majority spin type (majority electrons) tunnel into many free majority states and few electrons with the minority spin type (minority electrons) tunnel into few minority states as illustrated in Fig. 2.3 **a**. The spin-polarized current is therefore large. If the electrode magnetizations are anti-parallel, majority electrons can only tunnel into few minority states of the second electrode (but with the same spin type) and few minority electrons can tunnel into many majority states as depicted in Fig. 2.3 **b**. The result is a low spin-polarized tunnel current. By using this effect in STM geometry, one can combine the detection of the local magnetization

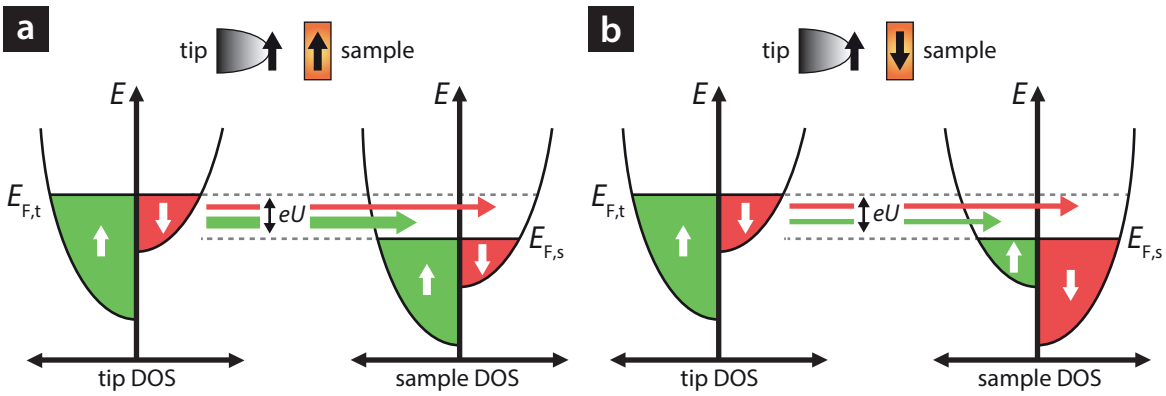

Figure 2.3.: Illustration of the tunnel magnetoresistance effect. **a**, Spin-dependent tunnel current in case of a parallel alignment of tip and sample electrode. **b**, Tunnel current for an anti-parallel alignment of the electrodes. The schematic is based on a schematic on Fig. 3.7 in [110].

and the high spatial resolution of the STM [75, 78, 108, 109]. In this case, the tunnel current is extended by an additional term I_{SP} [109]

$$I_{SP}(\vec{r}_{\mathrm{t}}, U) \propto \sum_{\mathrm{a}} \left[P_{\mathrm{t}}(E_{\mathrm{F,t}}) P_{\mathrm{s}}(E_{\mathrm{F,s}} + eU) \cos\left(\angle\left[\vec{m}_{\mathrm{t}}, \vec{m}_{\mathrm{s}}(\vec{r}_{\mathrm{a}})\right]\right)\right] \cdot \mathrm{e}^{(-2\kappa|\vec{r}_{\mathrm{t}} - \vec{r}_a|)} \tag{2.14}$$

with $\vec{r}_{\mathrm{t}}$ and $\vec{r}_a$ as the positions of the tip and sample atom a, U the sample bias, $P_{\mathrm{t}}(E_{\mathrm{F,t}})$ and $P_{\mathrm{s}}(E_{\mathrm{F,s}} + eU)$ the energy dependent tip and sample polarization, e the electron charge, $E_{\mathrm{F,t}}$ and $E_{\mathrm{F,s}}$ as the Fermi energy of tip and sample, respectively, and $\vec{m}_{\mathrm{t}}$ and $\vec{m}_{\mathrm{s}}$ the magnetization directions of tip and sample and the exponential term as above. The sum runs over all sample atoms a.

Tunneling anisotropic magnetoresistance effect (TAMR)

The tunneling anisotropic magnetoresistance (TAMR) is a consequence of the spin-orbit coupling which, in general, is a small effect and can be treated as a perturbation. Due to the origin in the spin-orbit interaction, the TAMR effect becomes important if heavy substrates like, e.g. Ir or W are used. Approximated to the first order, the spin-orbit coupling leads to a mixing of states with different orbital character [27, 60]. The TAMR effect introduces an additional contribution to the (spin-averaged) LDOS of atom a which depends on the direction of the magnetic moment of atom a. As a result, the definition of the tunnel current needs to be extended since it crucially depends on the LDOS at position $\vec{r}_a$ [27]

$$I_{\mathrm{TAMR}} \propto \sum_{a} \gamma f\left(\Phi_a, \theta_a\right) \cdot \mathrm{e}^{(-2\kappa|\vec{r}_{\mathrm{t}} - \vec{r}_a|)} \tag{2.15}$$

with γ as a scaling constant, $f(\Phi_a, \theta_a)$ as the angle dependent contribution of the LDOS of atom a, Φ_a and θ_a as the azimuth and polar angles relative to the local spin quantization axis of atom a and $\kappa = \sqrt{2m\phi/\hbar^2}$ as the inverse decay constant, the sum extends over all atoms a. This additional current contribution allows the detection of a magnetic signal by an electrical measurement. However, the effect typically amounts only to a few percent due to its origin from spin-orbit coupling [60, 61].

2.3.3. Scanning tunneling spectroscopy (STS)

The STM can also be used for the measurement of the vacuum local density of states (LDOS). The differential conductance at the tip position $\vec{r}_\mathrm{t}$ is proportional to the sample LDOS at energy $E_\mathrm{F,s} + eU$ if Eq. 2.10 is differentiated [102]

$$\frac{\mathrm{d}I_\mathrm{T}(\vec{r}_\mathrm{t}, U)}{\mathrm{d}U} \propto \rho_\mathrm{t}\rho_\mathrm{s}(\vec{r}_\mathrm{t}, E_\mathrm{F,s} + eU) \tag{2.16}$$

with $\vec{r}_\mathrm{t}$ as the tip position, ρ_t and $\rho_\mathrm{s}(\vec{r}_\mathrm{t}, E_\mathrm{F,s} + eU)$ as the density of states of tip and sample, respectively, $E_\mathrm{F,s}$ as the Fermi energy of the sample, and eU as the electron energy at sample bias U. Note that Eq. 2.16 is only valid if eU is much smaller than the sample's work function ϕ. The differential conductance is usually obtained by using lock-in technique due to the better signal-to-noise ratio compared to a numerical derivation of the tunnel current. Using the first derivative of the tunnel current allows a direct access to the sample LDOS.

In this work, the differential conductance was measured in two different ways: a local measurement in which the height and the position of the tip above the sample is fixed and the sample bias is varied (single point spectroscopy) and a mapping mode in which the height and position is varied and the sample bias is fixed ($\mathrm{d}I/\mathrm{d}U$ map). Single point spectra were typically recorded as follows: the tip was moved to the measurement position and initial parameters, the so called stabilization parameters I_stab and U_stab, were applied. In a next step, the feedback loop was opened and the sample bias was varied, thereby recording the differential conductance $\mathrm{d}I/\mathrm{d}U$. Afterwards, the imaging parameters were restored. Maps of differential conductance were recorded in constant-current mode simultaneously to the sample topography.

The stabilization parameters for single point spectroscopy need to be carefully chosen and must be the same for a set of spectra if they should be compared afterwards. According to [102, 103], the tunnel current I_stab is proportional to the integrated LDOS up to the applied sample bias U_stab. If two spectra are measured at two different positions which show a different LDOS in the interval between 0 and U_stab, e.g. a flat LDOS and an LDOS with a strong peak, the resulting stabilization height at I_stab and U_stab is different although the tunnel current I_stab is the same. This initial difference in height results to different measured intensities while recording the spectra since the height is kept fixed during the measurement. The intensity variation could be misinterpreted as inherent sample features rather than measurement artefacts [111]. This is why the stabilization voltages U_stab in

this work were carefully chosen to contain only flat parts of the sample LDOS for both ferromagnetic regions and the skyrmion center (and all spectra between these points). This flat LDOS was always found in the negative sample bias regime.

2.3.4. Atom manipulation

In general, there are two different modes of atom manipulation: vertical and lateral, as e.g. described in [112]. In this work, only lateral manipulation was used. Lateral movement of atoms and clusters can be done in pulling mode (attractive tip-adsorbate interaction), pushing mode (repulsive tip-adsorbate interaction) and sliding mode (adsorbate is directly bound below the tip) as e.g. in [80, 112–114]. Besides the sliding mode, the manipulation mode typically depends on the species of the tip apex atom and the surface adsorbate. Lateral manipulation is typically done as follows[1]: the STM is operated in constant-current mode. The steps of the procedure are illustrated in Fig. 2.4: the tip is positioned above the atom and subsequently lowered (**1.**), thereby establishing a chemical bond between the tip's apex atom and the surface adatom. The tip is moved sideways, thereby following the contour of the adatom in order to maintain the set-point of the tunnel current (**2.**). While following the adatoms's contour and moving sideways, the interaction strength between the tip and the adatom exceeds the binding force to the surface. At a certain point, the adatom moves one atomic site towards the tip (the adatom 'jumps'). Due to the new position of the adatom closer to the tip, the tunnel current increases. The feedback loop instantaneously retracts the tip and the set-point of the tunnel current is restored (**3.**). This leads to a characteristic tip movement signal while doing lateral atom manipulation (inset of Fig. 2.4). Using this procedure, complex single atom arrangements can be realized e.g. as in [81, 84]. Furthermore, this technique can be combined with SP-STM which allows the study of artificial magnetic nanostructures e.g. as in [83–85, 89].

2.4. Short overview of the properties of PdFe/Ir(111)

The physical system PdFe on Ir(111) and its properties are briefly described in this section. This system was used during this entire study. The results shown in the following were taken from [9, 115].

2.4.1. The different magnetic phases

Figure 2.5 shows SP-STM images of the different magnetic phases of PdFe on Ir(111) at a temperature of $T = 8\,\mathrm{K}$ [9]. At $B_{\mathrm{ext}} = 0\,\mathrm{T}$, the system shows a magnetic spin spiral (Fig. 2.5

[1] description for pulling mode; pushing mode is similar but with a repulsive interaction

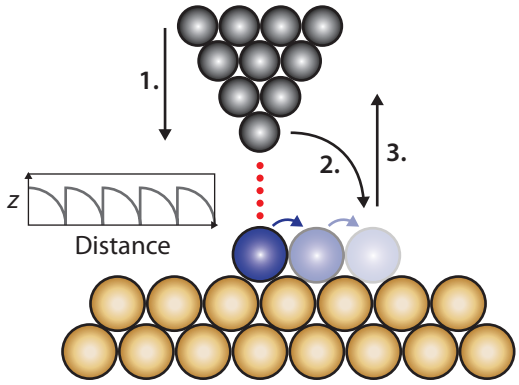

Figure 2.4.: Illustration of the tip movement during lateral atom manipulation (pulling mode). 1., The tip approaches the atom. **2.**, The tip moves along the atom's contour until the atom jumps to the next lattice site due to a stronger interaction between tip and adatom than between adatom and surface. **3.**, The tip immediately retracts. The result is a z curve as found in the inset. Schematic based on [112].

d) with a period of ∼6 nm as can be seen by the alternating bright-dark contrast on the PdFe in Fig. 2.5 **d**. Fig. 2.5 **a** shows a sketch of a spin spiral. The application of a moderate external magnetic field of $B_{\text{ext}} = +1\,\text{T}$ leads to a phase transition: the spin spiral evolves to axisymmetric skyrmions as shown in Fig. 2.5 **e**. A sketch of skyrmions is shown in Fig. 2.5 **b**. At this low external field, both magnetic states can coexist. This transition regime is left at a magnetic field of $B_{\text{ext}} = +1.4\,\text{T}$: the PdFe island solely shows a hexagonal arrangement of skyrmions (Fig. 2.5 **f**). At $+2\,\text{T}$, the ferromagnetic phase is reached and the system is saturated as shown in Fig. 2.5 **g** and **c**. In this regime, single skyrmions may still survive due to local perturbations within the potential landscape although free skyrmions as in the lattice phase are not found anymore.

2.4.2. Manipulating the magnetic state

The magnetic state of PdFe on Ir(111) can be manipulated using the SP-STM tip if the system is in a transition field regime either between the spin spiral and the skyrmion lattice or between the skyrmion lattice and the ferromagnet. This is shown in Fig. 2.6 [9]. The measurements were performed at a temperature of $T = 4.2\,\text{K}$, at which the magnetic states in PdFe/Ir(111) are metastable in contrast to the magnetic states at $T = 8\,\text{K}$. In Fig. 2.6 **a**, the system is at a field value at which the skyrmion lattice state is slightly favored over the spin spiral but due to metastability, an energy barrier prevents the transition to the skyrmion state. A magnetic change is induced by scanning the island with a high sample bias of $+1\,\text{V}$ (not shown). As a result, the island relaxes partly into the prefered skyrmion state as shown in Fig. 2.6 **b**.

The possibility to locally transform the magnetic state by high energy electrons is exploited in Fig. 2.6 **c** and **d**. The sample was first brought into the ferromagnetic state at $B_{\text{ext}} = +3\,\text{T}$,

at which all moments are aligned to the magnetic field (not shown). Afterwards, the field was lowered to $B_{\mathrm{ext}} = +1.8\,\mathrm{T}$ as shown in Fig. 2.6 **c**. At this field value, skyrmions are favored over the ferromagnet but an energy barrier prevents their formation (cf. Fig. 2.6 **f**, upper sketch). The system was locally relaxed into the skyrmion phase by injecting high energy electrons into the system: the tip was parked in the vicinity of an adsorbate within the surface and the sample bias was increased up to around +800 mV (feedback loop closed). The creation of a skyrmion can be observed in the recorded differential conductance [115]. Afterwards, the sample is imaged again to verify the creation of a single skyrmion Fig. 2.6 **d**. By locally injecting high energy electrons, it was possible to overcome the potential barrier which prevented a skyrmion formation. Using this scheme, the island can be gradually populated with skyrmions as shown in Fig. 2.6 **d**.

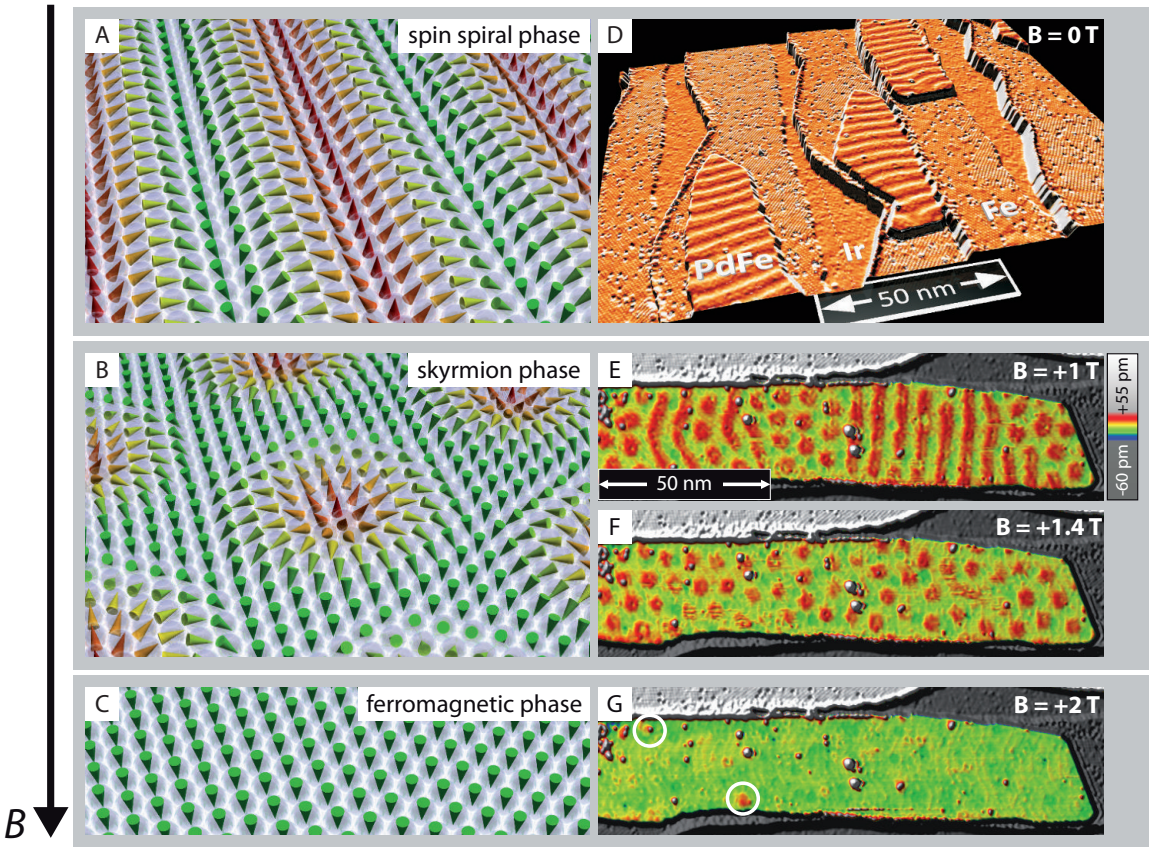

Figure 2.5.: Magnetic phases of PdFe/Ir(111) revealed by SP-STM images. a and **d**, At $B_{\mathrm{ext}} = 0\,\mathrm{T}$, the magnetic ground state is a spin spiral. **b**, **e** and **f**, The application of moderate magnetic fields leads to a transformation of the spin spiral phase into the skyrmion lattice phase (**f**) via a state in which both spiral and skyrmion structures coexist (**e**). **c** and **g**, At high magnetic fields, the sample is saturated and the ferromagnet becomes the ground state. The image parameters were $I_{\mathrm{T}} = 0.2\,\mathrm{nA}$, $U_{\mathrm{B}} = +50\,\mathrm{mV}$, $T = 8\,\mathrm{K}$. From Romming *et al.*, Science 09 Aug 2013, Vol. 341, Issue 6146, pp. 636-639 [9]. Reprinted with permission from AAAS.

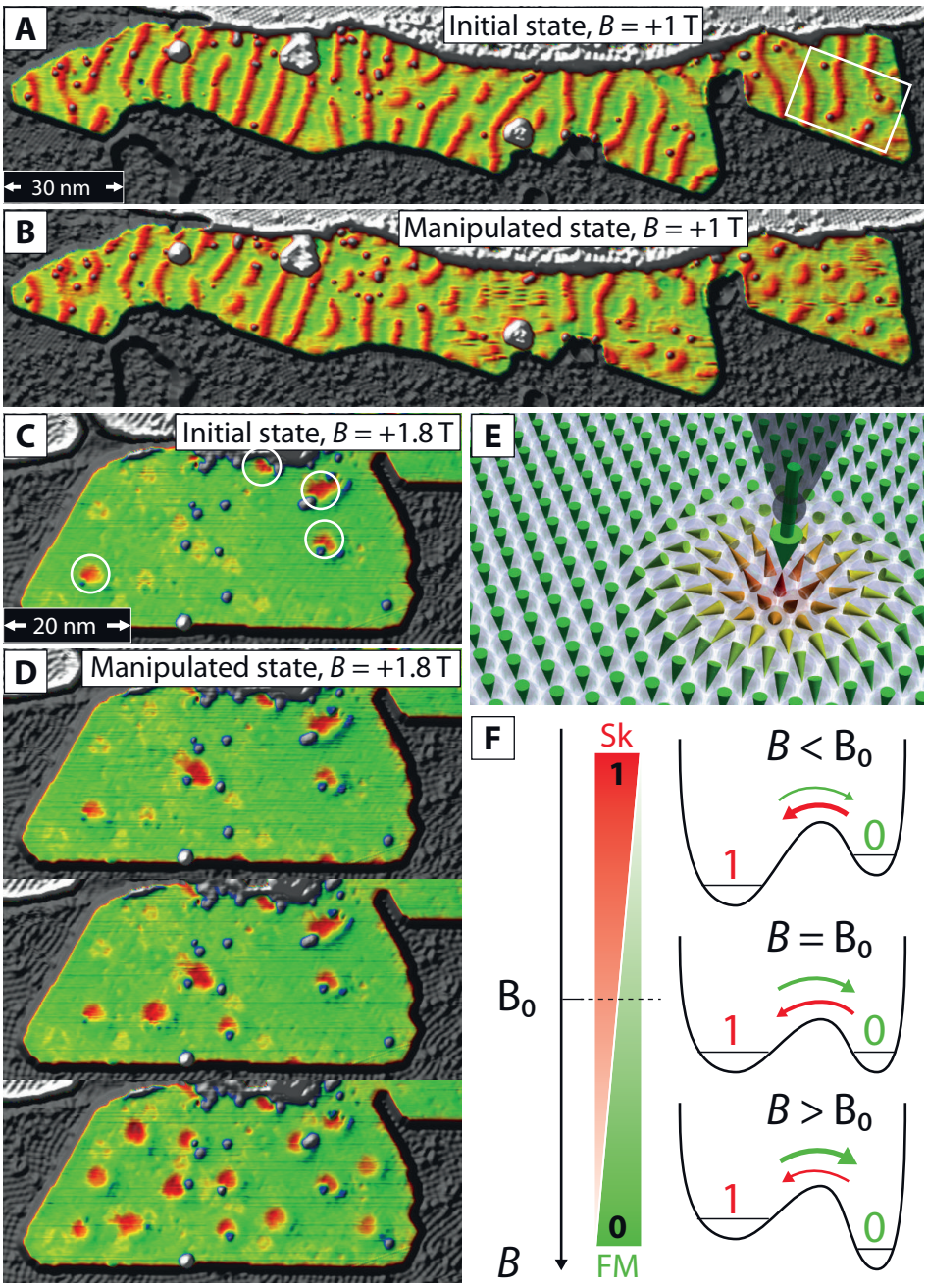

Figure 2.6.: Manipulation of the magnetic state of PdFe/Ir(111) by SP-STM. a and **b**, A PdFe island is imaged before (**a**) and after (**b**) a scan with a high sample bias of +1 V (not shown). As a result of the high energy scan, the magnetic state changes from the spin spiral to the skyrmion phase. **c** and **d**, A PdFe island is imaged after several local injections of high energy electrons. As a consequence, the island is subsequently populated with isolated skyrmions (**d**). **e**, Schematic of the local energy injection with the STM tip. **f**, Schematic of a simple two level model which depicts the effect of the external magnetic field on the switching probability between skyrmion and ferromagnet. The image parameters for **a** and **b** were $I_T = 0.5\,\text{nA}$, $U_B = +100\,\text{mV}$, $B_{ext} = +1\,\text{T}$; for **c** and **d** $I_T = 1\,\text{nA}$, $U_B = +100\,\text{mV}$, $B_{ext} = +1.8\,\text{T}$ after sweeping down from $B_{ext} = +3\,\text{T}$. All measurements were done at $T = 4.2\,\text{K}$. From Romming *et al.*, Science 09 Aug 2013, Vol. 341, Issue 6146, pp. 636-639 [9]. Reprinted with permission from AAAS.

3. Instrumentation and sample preparation

All results shown in this work were obtained using a unique multi-chamber ultra-high vacuum system (UHV system) which provides several surface analysis and thin film preparation techniques. The core pieces are two home-built low-temperature STMs which were used for the experiments in this work. The specific characteristics of the UHV system and the low-temperature STMs together with the sample preparation procedure are described in the following sections.

3.1. The ultra-high vacuum chamber system

The whole ultra-high vacuum chamber system (UHV system) consists of different chambers for sample and tip preparation and sample investigation as shown in Fig. 3.1. The base pressure of the system is between 1×10^{-10} mbar and 5×10^{-11} mbar which is maintained by getter pumps (diodes and triodes) and titanium sublimation pumps (fired in intervals between 4 and 8 hours). In addition, the microscope chambers are also pumped by non-evaporable getter pumps (NEG pumps) as e.g. in [116], chapter 2, pages 69-70. To reduce mechanical noise coupling via the building's foundation, the chamber system floats on a passive air-damped table which is located on a separate foundation within the building. In addition, the UHV system is located inside a room with an inner and an outer wall which reduces acoustic coupling from the surroundings. The central piece of the chamber system is a distribution chamber fabricated by Omicron [117] (Fig. 3.1, chamber **1**). Using this chamber, samples and tips can be moved to all other connected chambers by using the same transport system. A load-lock allows a quick exchange of new sample crystals as well as new STM tips (not shown). For individual sample and tip cleaning and preparation procedures, devices for (mass selective) ion sputtering (Fig. 3.1, chambers **2** and **7**), oxygen annealing (Fig. 3.1, chamber **7**) and heating by a high energy electron beam (Fig. 3.1, chamber **7**), resistive heating (Fig. 3.1, chambers **2, 6** and **7**) and a boron-nitride heater (Fig. 3.1, chamber **3**) are available. Metal thin films can be grown by molecular beam epitaxy (MBE) in chambers **2, 3** and **6** using a variety of high purity elements. For the determination of the sample quality, Auger electron spectroscopy (AES) and low-energy electron diffraction (LEED) can be done in the analysis chamber (Fig. 3.1, chamber **2**). A room-temperature STM is attached to the MBE chamber which allows detailed growth studies and a pre-characterization of the sample (Fig. 3.1, chamber **6**). Two low-temperature STMs at around 8 K and at 4.2 K are accessible via the central chamber and are used for (SP-)STM and (SP-)STS measurements (Fig. 3.1, chamber **4** and **5** respectively).

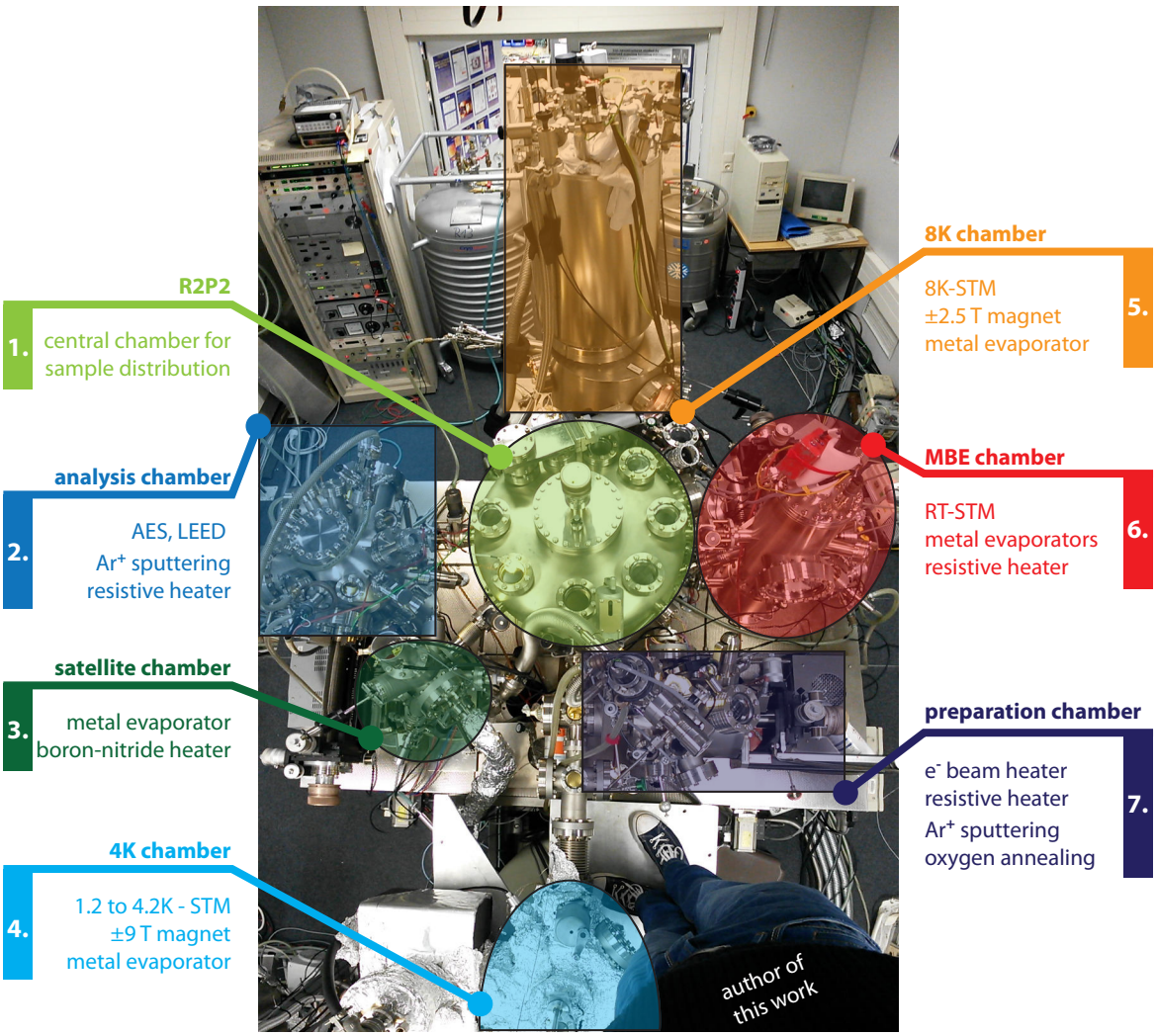

Figure 3.1.: Overview of the experimental setup which was used in this work. A central chamber (**1**) is connected to all other chambers of the UHV system. The setup provides various chambers for sample preparation (**2,3,6,7**) and for surface analysis (**2,6**). In addition, two low-temperature STMs are attached to the central chamber (**4,5**).

3.2. Low temperature scanning tunneling microscopes

Two different low-temperature STMs are connected to the UHV chamber system which is described in this section. Both microscope heads are shown in Fig. 3.2. The main difference is the access point of tip and sample which is either from the top (4K-STM in Fig. 3.2 **a**) or from the side (8K-STM in Fig. 3.2 **b**). Besides the different access ways, the design principle of both STMs is the same: a piezo tube is glued inside a hollow sapphire prism which again is mounted inside the housing. The piezo tube holds the STM tip and is utilized for the movement of the tip above the surface: by applying a voltage between the central

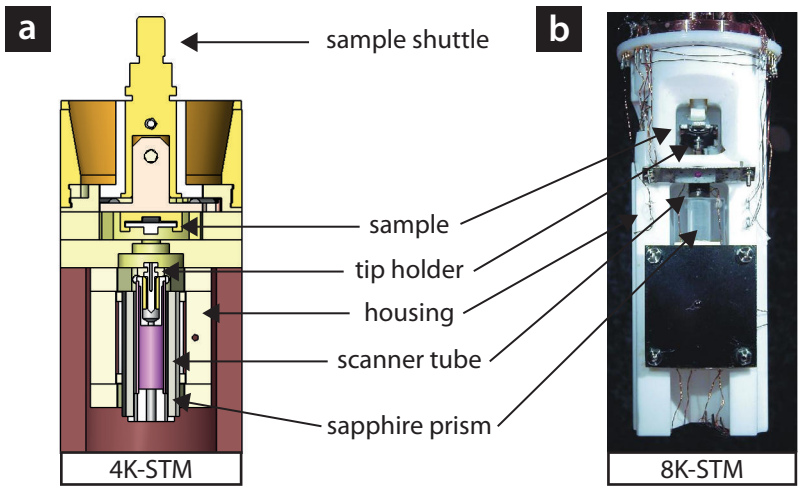

Figure 3.2.: STM heads of both 4K- and 8K-systems. **a**, Schematic of the 4K-STM head. The sample and tip access is from the top. **b**, Photography of the 8K-STM head. The tip and sample access is from the side. In both setups, the tip is mounted inside a piezo tube which is glued into a hollow sapphire prism. The prism can be moved towards the sample via piezo actuators (not visible). The STM in **b** is rotated by 180° for reasons of convenience and was taken from [110].

and an outer electrode, the tip moves in x and y direction. The coarse movement is realized by piezo stacks which are working in stick-slip mode as described e.g. in [110], section 3.2, pages 12-14. Both STMs have tip exchange mechanisms which is a crucial requisite for (SP-)STM. Typical tip materials are W tips for non–spin-polarized STM and Fe or Cr coated W tips and Cr bulk tips for SP-STM measurements [118, 119]. The choice of the tip material for SP-STM strongly depends on the desired experiment. If the sample magnetism does not respond to the external magnetic field, Fe coated tips are used. Depending on the thickness of the Fe layer, the tips show a magnetization which is dominantly in-plane at zero magnetic field. Since Fe is a ferromagnetic material, it aligns its magnetization according to the external field at strong magnetic fields. By using the magnetic field for the alignment of the tip magnetization, both in-plane and out-of-plane magnetizations can be accessed. Antiferromagnetic Cr tips are typically used for experiments in which the sample magnetism follows the external magnetic field and the tip magnetization needs to stay fixed. However, although the tip material is magnetic, sometimes, the tip does not have a spin-polarization which leads to a detectable magnetic contrast at the desired energy. In this case, the tip can be considered as non–spin-polarized.

The different access paths for tip and sample in the two STMs have wide-ranging consequences for the design of cryostats and magnets. The first difference is the coupling of the STMs to the liquid helium reservoir. Figure 3.3 **a** shows the indirect coupling of the 4K-STM: the microscope is mounted at the bottom part of a UHV insert which is located inside the cryostat insert. Due to the STM access from the top, the helium inside the cryostat can be isolated from the environment at room temperature by layers of superinsulation. This type of insulation is only usable, if a closed shielding around the cryostat is ensured (which

would not be the case for the 8K-STM with its access from the side). The UHV insert and the cryostat insert of the 4K-STM are mechanically not connected. The thermal coupling is achieved by introducing helium as a thermal exchange gas between the UHV insert and the cold cryostat insert (exchange gas section). This decoupling from the liquid helium bath is needed in order to reach temperatures below 4.2 K[1]. In the normal operational mode at 4.2 K, the thermal coupling is achieved by a suitable exchange gas pressure of a few 100 mbar. If lower temperatures around 1 K are required, the UHV insert is decoupled from the helium bath by evacuating the exchange gas section. Helium gas is pumped through a cold trap at liquid nitrogen temperatures into a capillary. The capillary coils around the UHV insert at 4.2 K in order to pre-cool the helium gas which runs through the capillary. The purpose of the cold trap is to clean the circulating helium gas from contamination gas species which might freeze inside the capillary and thereby clog it. Finally, the helium gas is expanded near the bottom of the cryostat insert from the outlet of the capillary. This expansion through a throttle leads to the Joule-Thomson effect thereby reducing the temperature of the helium below 4.2 K. This in turn cools the lower part of the UHV insert. In contrast to the 4K-STM setup, the 8K-STM is directly mounted to the helium cryostat (Fig. 3.3 **b**) and is cooled by thermal conduction. Since the access of the 8K-STM is from the side, the thermal shielding from the environment is done by an additional rotatable copper shield which is connected to a liquid nitrogen cryostat. With this setup, the minimal reachable temperature is around 8 K[2].

Another distinctive feature is the magnet system of both setups as shown in Fig. 3.3. Magnets are crucial for a wide range of SP-STM and SP-STS experiments. Again, the magnet design is determined by the access way to the STM: the magnet of the 4K-STM is a superconducting solenoid magnet with a maximal magnetic field perpendicular to the surface plane of ±9 T. The magnet of the 8K-STM is a superconducting magnet in a Helmholtz configuration which is needed in order to allow a tip exchange from the side of the STM. This magnet can reach a maximal magnetic field of ±2.5 T perpendicular to the surface plane. The pre-amplifiers are home-built differential amplifiers. Their signal is recorded by using a Specs Nanonis SPM controller [121]. A comparison of the technical details of the two STMs can be found in Tab. 3.1.

3.3. Sample preparation

The PdFe bilayer on Ir(111) is prepared in a two step procedure which consists of the substrate cleaning and the thin film preparation. Both parts need to be done carefully in order to avoid an accumulation of adsorbates. This is a crucial requirement for the STS

[1]The typical used operation temperature is 4.2 K. For reasons of convenience, this STM is called 4K-STM in this work.

[2]The typically reached temperature is 7.7(2) K. However, this STM is called 8K-STM in this work.

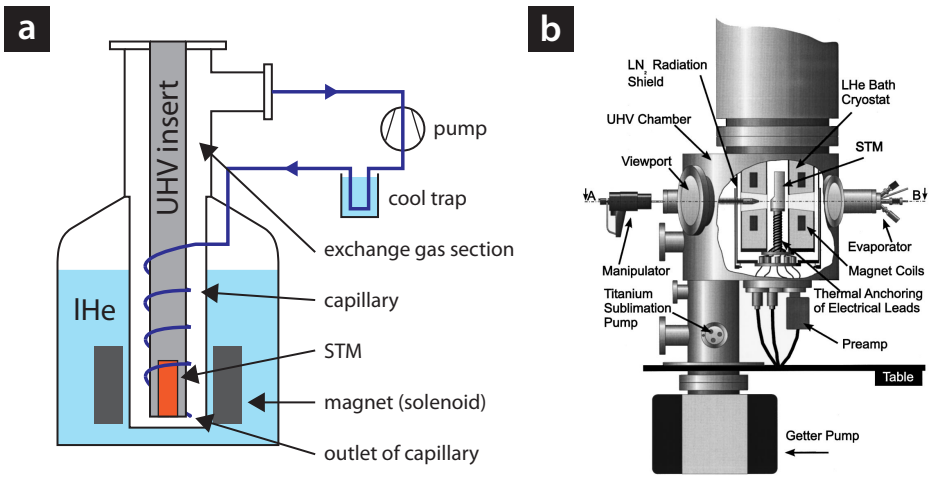

Figure 3.3.: Schematic of the cryostat of the 4K- and 8K-STM. **a**, Setup of the cryostat of the 4K-STM. The UHV insert is decoupled from the liquid helium reservoir by an insulating vacuum (exchange gas section). A thermal coupling is achieved if clean helium gas is introduced into the exchange gas section. The minimal reachable temperature in this mode is 4.2 K. In order to reach lower temperatures of ∼1 K, the cryostat is operated in Joule-Thomson mode: helium gas is let into the evacuated exchange gas section via a capillary which is coiled around the UHV insert (for pre-cooling) and which has its outlet at the bottom of the UHV insert. The gas expands after leaving the capillary and the gas temperature decreases due to the Joule-Thomson effect. **b**, Setup of the 8K-STM. The STM is directly mounted to the liquid helium reservoir. The thermal shielding is realized by an outside copper shield at liquid nitrogen temperature. The image in **b** was taken from [120].

study in Sec. 4 and the pinning experiments in Sec. 5. The procedure is described in the following.

3.3.1. Cleaning the Ir(111) surface

Several high purity Ir single crystals with a (111) surface orientation were used as a substrate for the experiments shown in this work. In order to remove several layers from the surface, the crystal was sputtered using Ar^+ ions with an acceleration voltage of +800 V. A subsequent annealing at ∼1500 K smooths the surface. Afterwards, the sample was annealed in an oxygen atmosphere in order to remove carbon contaminants by their oxidation to CO_x. During the oxygen annealing procedure, the oxygen pressure is lowered in steps from an initial pressure of $\sim 1 \times 10^{-6}$ mbar to a final pressure of $\sim 8 \times 10^{-8}$ mbar. The crystal underwent repeated heating ramps with a maximal temperature of around ∼1500 K. Each heating cycle took ∼3 min and was repeated between 4 to 12 times at each oxygen pressure level. Once the UHV conditions were restored, the sample was again heated to ∼1500 K for ∼60 s. This extended cleaning procedure was repeatedly done after several thin film preparations

Table 3.1.: Summary of technical features of the two low-temperature STMs.

Feature	8K-STM	4K-STM
tip/sample access	from the side	from the top
T_{base}	$\sim$13 K (open inner door) $\sim$8 K (closed inner door)	$\sim$4.2 K (standard mode) $\sim$1.2 K (Joule-Thomson)
cryostat	bath cryostat (liquid helium)	bath cryostat (liquid helium)
thermal shielding	outer cryostat (liquid nitrogen)	superinsulation
thermal contact	direct mounting to cryostat	via exchange gas
lHe refill interval	$\sim$2 d	$\sim$7 d
magnet design B_{ext}	Helmholtz coils $\pm$2.5 T, $\vec{B}_{\text{ext}} \| \vec{e}_z$	solenoid $\pm$9.0 T, $\vec{B}_{\text{ext}} \| \vec{e}_z$
T for single atom deposition	< 25 K (measured)	> 25 K (estimated)
scan range	$\sim 6 \times 6\,\mu\text{m}^2$	$\sim 0.7 \times 0.7\,\mu\text{m}^2$

depending on the concentration of contaminations and the quality of the thin film growth. For the preparations between the oxygen annealing, only the Ar^+ sputtering and annealing was applied in order to remove the old thin film from the surface.

3.3.2. Preparation of the PdFe bilayer on Ir(111)

After oxygen annealing and after restoring UHV conditions again, the crystal was again annealed at $\sim$1500 K for $\sim$30 s. Afterwards, less than one atomic layer of Fe was deposited from a 99.99 % pure, 2 mm thick rod [122] using a commercial electron beam evaporator by Omicron [117]. This was done in the MBE chamber (Fig. 3.1, chamber **6**). The deposition was started several minutes after the annealing (typically around 4 min to 5 min), so that the Ir crystal is believed to be moderately above room temperature at the time the Fe was evaporated. The exact temperature is unknown due to a lack of a suitable *in-situ* temperature measurement instrument. After the Fe deposition, the sample was moved to the satellite chamber for a subsequent Pd deposition in the sub-monolayer coverage regime (Fig. 3.1, chamber **3**). The Pd was evaporated from a 99.99 % pure, 2 mm thick rod [123] using a commercial Omicron electron beam evaporator [117]. The crystal was slightly heated ($<$65 °C) during the evaporation using a boralectric heating element [124]. Both Fe and Pd evaporators were at their final evaporation parameters before the sample was inserted into the chamber and until the sample had left the chamber. The deposition was always done under UHV conditions.

3.3.3. Single atom deposition

Both low temperature microscopes were used for the pinning experiments in Sec. 5. Single atoms were deposited in different ways. For the 4K-STM, the procedure was as follows: the cold sample was moved from the STM into the top chamber thereby crossing the beam of the running electron beam evaporator. The sample was inserted back into the STM directly after the deposition. The time of the sample in an environment at $T \sim 300\,\mathrm{K}$ was typically less than $\sim 6\,\mathrm{s}$. After the sample was inserted into the microscope, the STM temperature did usually not exceed 6.5 K. Nevertheless, the temperature was measured at the bottom of the STM body which is approximately 12 cm away from the sample. The real maximal sample temperature as well as the deposition temperature are therefore unknown. By comparing the single atom depositions of the 8K-STM and the 4K-STM, it is reasonable to estimate a lower boundary for the deposition temperature. The single atom deposition, which was done in the 4K-STM setup, typically showed a moderate formation of clusters. This was not observed for the deposition result of the 8K-STM with a maximal sample temperature of less than 25 K. Therefore, the minimal deposition temperature in the 4K-STM setup is estimated to be above 25 K.

The setup for single atom deposition in the 8K-STM is conceptually different to the setup of the 4K-STM. The single atom deposition scheme of the 8K-setup exploited the access to the sample from the side. In contrast to the 4K-setup, the sample was not removed from its cold environment inside the STM and its temperature could be monitored at all times. The single atom deposition was achieved by a rotatable sample stage and an openable hole in the thermal shields around the STM which gave the access for the atom beam to the sample surface. Before the deposition, the tip was retracted and the sample stage was slightly rotated using piezo actuators and a mechanical hand. The deposition started by rotating the outer thermal shield to the deposition position so that the running evaporator beam hit the surface. After the deposition was finished, the shield was closed and the sample stage was moved back to its initial horizontal position. The typical maximal sample temperature was around 22 K to 25 K. For the experiment in Sec. 5.2, the measurement without atoms was done on an already tilted sample. The deposition itself was executed as described above without the need to rotate the sample in the sample stage. This allowed an imaging of the same region before and after the deposition procedure.

4. Observation of the non-collinear magnetoresistance effect in PdFe/Ir(111)

As was shown in Sec. 2.4, the system PdFe/Ir(111) exhibits different magnetic phases. In order to learn more about the system, the sample is investigated by scanning tunneling spectroscopy (STS). Spatially resolved STS combined with the knowledge about the local magnetic orientation within the skyrmion and the spin spiral allow a detailed study of the vacuum local density of states (LDOS) in dependence of the local spin arrangement. For example, a possible contribution from the tunneling anisotropic magnetoresistance effect (TAMR) as found for other systems like the double layer of Fe on W(110) [60] could be identified, if present. This detailed study of the vacuum LDOS of the sample and its magnetic states is done in the following sections.

4.1. Scanning tunneling spectroscopy on magnetic skyrmions and the spin spiral

Isolated magnetic skyrmions in PdFe/Ir(111) are investigated by means of STS. Skyrmions exhibit interesting features: localization, magnetic non-collinearity embedded in a ferromagnetic surrounding and a size dependence for PdFe/Ir(111) which scales with the external magnetic field [9, 14]. The analysis in this section primarily focusses on the hcp stacking of Pd on an fcc stacking of Fe on Ir(111) (hcp-PdFe). A qualitatively similar effect is also observed for the fcc stacking of Pd on an fcc stacking of Fe on Ir(111) (fcc-PdFe), but is less pronounced.

4.1.1. Observation of magnetism with a non–spin-polarized tip

Figure 2.5 shows that the system PdFe/Ir(111) undergoes different magnetic phases which depend on the external magnetic field. Surprisingly, the magnetic phases can also be imaged with a non–spin-polarized Cr bulk tip using a sample bias of +700 mV as shown in Fig. 4.1. At zero and low magnetic field, the contrast resembles a TAMR contrast: the spin spiral appears with a periodicity being twice as large as the magnetic periodicity, whereas the skyrmion resembles a ring (Fig. 4.1 **a** and **b**). At higher fields, the contrast changes. Both spiral and skyrmion in Fig. 4.1 **c** exhibit a TMR-like contrast similar to Fig. 2.5 **f**, the

skyrmion has changed its appearance from a ring to a depression[1]. The observation of the different magnetic states with a non–spin-polarized tip is found for both stackings of hcp-PdFe and fcc-PdFe, but at different magnetic field regimes.

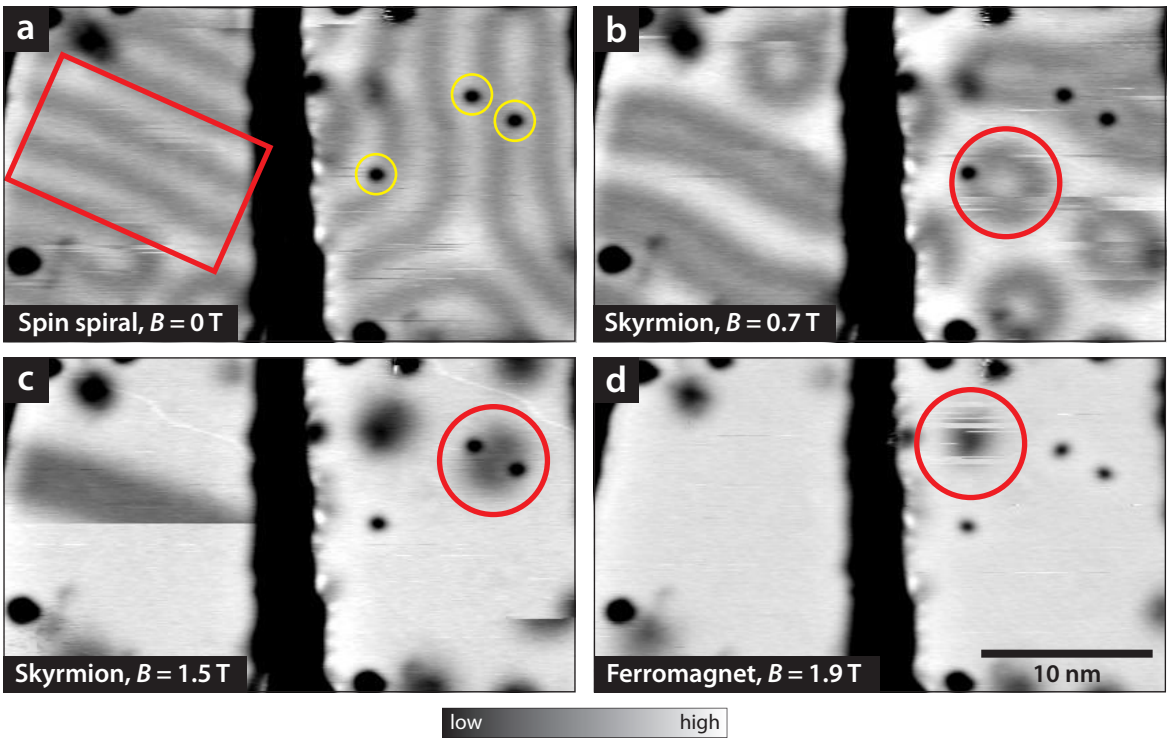

Figure 4.1.: Different magnetic phases of PdFe/Ir(111) imaged in $\mathrm{d}I/\mathrm{d}U$ maps with a non–spin-polarized tip. **a**, Spin spiral state at $B_{\mathrm{ext}} = 0\,\mathrm{T}$ (red box). The yellow circles indicate defects within the Pd layer. **b**, Transition regime between the spin spiral and the skyrmion phase (red circle) at $B_{\mathrm{ext}} = +0.7\,\mathrm{T}$. **c**, Only isolated skyrmions (red) can be stable at $B_{\mathrm{ext}} = +1.5\,\mathrm{T}$. **d**, At even higher fields of $B_{\mathrm{ext}} = +1.9\,\mathrm{T}$, skyrmions (red) become unstable. The imaging parameters were $I_{\mathrm{T}} = 1\,\mathrm{nA}$, $U_{\mathrm{B}} = +700\,\mathrm{mV}$, $U_{\mathrm{mod}} = 40\,\mathrm{mV}$ and $T = 4.2\,\mathrm{K}$. The measurement was done with a non- or weakly spin-polarized Cr bulk tip.

4.1.2. STS on skyrmions: Skyrmion center versus ferromagnet

Figure 4.2 **a** and **d** show an hcp-PdFe and an fcc-PdFe island on Ir(111) with isolated skyrmions (cf. Sec. A). All data were recorded using the same non– or low–spin-polarized Cr bulk tip. The arrows in the magnified panels of Fig. 4.2 **b** and **e** show the positions of the

[1] If the tip had a significant spin-polarization at this energy, the skyrmion would appear as a depression at all magnetic field values.

line sections in Fig. 4.2 **c** and **f**. At this magnetic field of $B_{\mathrm{ext}} = -2.5\,\mathrm{T}$, the skyrmion line sections differ in terms of signal strength: the intensity on hcp-PdFe shows a larger change and a deeper minimum than the fcc-PdFe skyrmion, which shows a shallow minimum at the center.

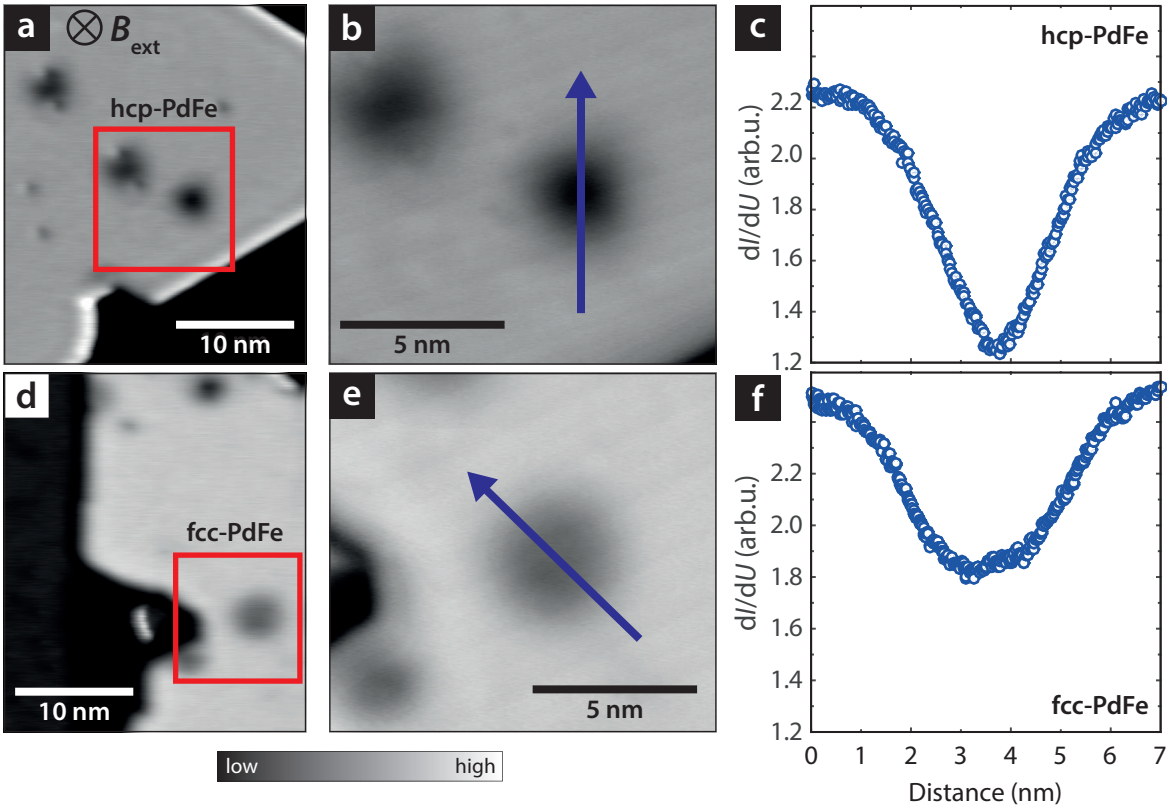

Figure 4.2.: Skyrmions on hcp-PdFe and fcc-PdFe. **a** and **d**, $\mathrm{d}I/\mathrm{d}U$ maps showing isolated skyrmions on a hcp-PdFe (**a**) and a fcc-PdFe (**d**) island and corresponding enlarged regions. The blue arrows in **b** and **e** show the positions of the line sections. **c** and **f**, Line sections through the isolated skyrmions. The measurement parameters were $I_{\mathrm{T}} = 1\,\mathrm{nA}$, $U_{\mathrm{B}} = +700\,\mathrm{mV}$, $U_{\mathrm{mod}} = 40\,\mathrm{mV}$, $B_{\mathrm{ext}} = -2.5\,\mathrm{T}$, and $T = 4.2\,\mathrm{K}$. The measurement was done with a non- or weakly spin-polarized Cr bulk tip.

To further investigate the difference between the two skyrmions, STS measurements were performed on the two skyrmions. The result is shown in Fig. 4.3. The positions where the spectra were measured are marked in Fig. 4.3 **a** and **b** by blue (ferromagnet) and red circles (skyrmion center) and the corresponding spectra are shown in **c** and **d**. The spectra of the ferromagnetic hcp-PdFe and fcc-PdFe are qualitatively the same, the different intensities result most likely from different stabilization heights for hcp-PdFe and fcc-PdFe during the STS measurement. However, the spectra at the skyrmion center significantly deviate from the ferromagnetic surrounding and their specific features depend on the stacking: the hcp-PdFe spectrum exhibits two maxima at around +500 mV and +900 mV compared to the pronounced single ferromagnetic peak at around +700 mV, while the spectrum on fcc-PdFe shows a single peak at a slightly higher energy around +800 mV.

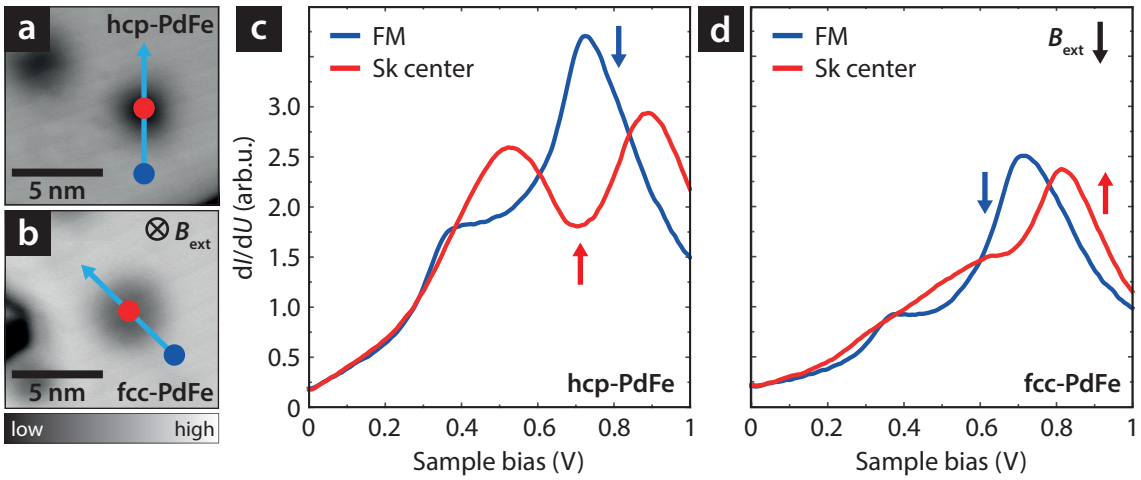

Figure 4.3.: STS data of the FM and the skyrmion center on hcp-PdFe and fcc-PdFe. **a** and **b**, $\mathrm{d}I/\mathrm{d}U$ maps showing the positions where the spectra were measured on the skyrmion center (red circle) and the ferromagnet (blue circle). **c** and **d**, Measured STS on hcp (**c**) and fcc-PdFe (**d**). The measurement parameters were $I_\mathrm{T} = 1\,\mathrm{nA}$, $U_\mathrm{B} = +700\,\mathrm{mV}$, $I_\mathrm{stab} = 1\,\mathrm{nA}$, $U_\mathrm{stab} = -1\,\mathrm{V}$, $U_\mathrm{mod,STS} = 7\,\mathrm{mV}$, $U_\mathrm{mod,map} = 40\,\mathrm{mV}$, $\tau = 10\,\mathrm{ms}$, $B_\mathrm{ext} = -2.5\,\mathrm{T}$, and $T = 4.2\,\mathrm{K}$. The measurement was done with a non- or weakly spin-polarized Cr bulk tip.

The spectra at the skyrmion center are anti-parallelly aligned to the FM (cf. Sec. 2.1). Due to the non–spin-polarized tip, TMR can be excluded as the responsible effect for the large change in the vacuum LDOS. Even if the tip showed a low spin-polarization, the TMR effect would only lead to an intensity change of the peaks in the vacuum LDOS, but not to the observed double peaks (hcp-PdFe) or shifted peak (fcc-PdFe). TAMR can also be ruled out since the STS were taken on TAMR-equivalent sites (collinear, but anti-parallel; cf. Sec. 2.3.2). The only remaining difference between the FM and the skyrmion center is the local magnetic environment. Hence, the explanation of the strongly changed vacuum LDOS resulting from the non-collinear environment of the skyrmion center requires an effect which has not been considered before.

4.1.3. The influence of the magnetic non-collinearity on the local STS

In order to test the effect of the magnetic environment on the vacuum LDOS, STS were taken twice at the same positions on the island, while the magnetic state (and with it the magnetic environment) of the sample changed between the two STS sequences. The result is shown in Fig. 4.4. The initial measurement was done on a skyrmion (**a**), the second subsequent STS sequence was measured along the edge of a skyrmion which moved to the island edge (**c**). In this experiment, a non- or only weakly spin-polarized Cr bulk tip was used. The sample was imaged before each STS sequence showing the current magnetic state (cf. Fig. 4.4 **a** and **c**). Spatially resolved spectra were taken along the blue arrows and are depicted as color-coded waterfall plots in Fig. 4.4 **b** and **d**, the red color marks the position of the high

energy peak. In Fig. 4.4 **b**, the main STS peak of the skyrmion smoothly shifts towards higher energies and back to the ferromagnetic value while moving along the skyrmion. This peak shift is not retrieved in Fig. 4.4 **d**, where the skyrmion has moved towards the island edge. The spectra along the skyrmion edge were measured at a local magnetic environment which only slightly deviates from the ferromagnet, although the STS were measured at the same positions compared to Fig. 4.4 **b**. Except for minor deviations, all spectra in Fig. 4.4 **d** resemble the FM spectra found at 0 nm and 8 nm in both Fig. 4.4 **b** and **d**. This is also found in the inset in Fig. 4.4 **d**, in which spectra at the same position (black dashed line, skyrmion center and skyrmion edge) are compared. The spectrum at the skyrmion center,Fig. 4.4 inset, indicates that the measurement was done on hcp-PdFe due to the two peaks at ∼500 mV to 900 mV (cf. Fig. 4.3).

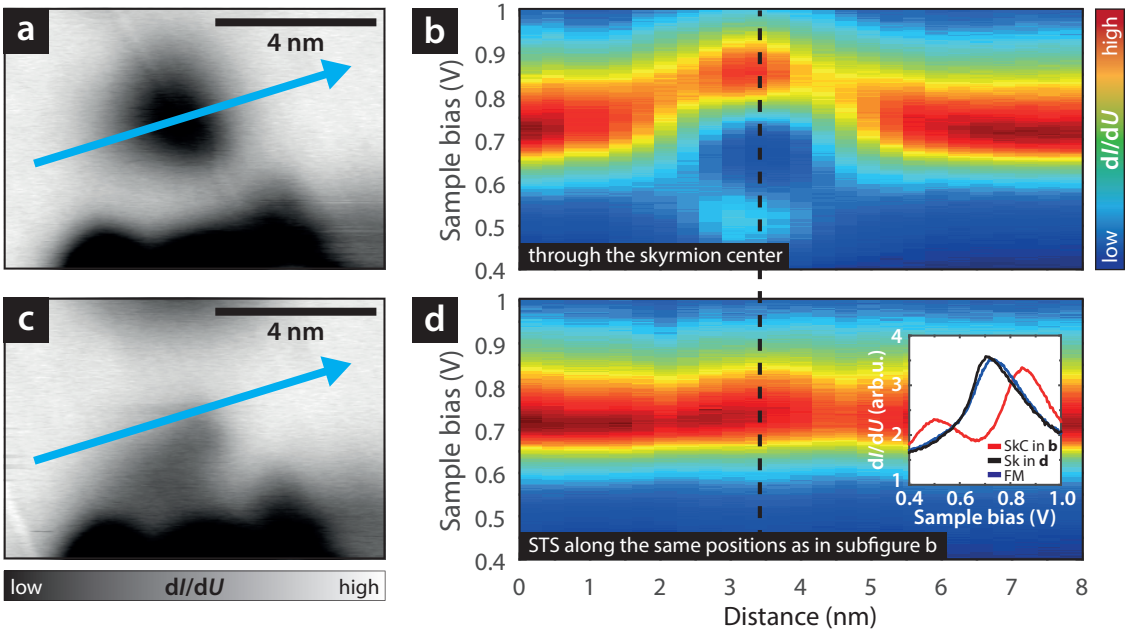

Figure 4.4.: Locally resolved STS along the center and the edge of a skyrmion in hcp-PdFe. **a** and **c**, $\mathrm{d}I/\mathrm{d}U$ maps showing the skyrmion and the moved skyrmion at the island edge, respectively. The arrow illustrates the direction along which the STS sequence was measured. **b** and **d**, Color-coded waterfalls plots of the single point spectra taken along the blue arrow in **a** and **c**. Inset in **d**, Comparison of the spectra at the same position on the PdFe island for the skyrmion center (red) and the skyrmion edge (black). The measurement parameters were $I_\mathrm{T} = 1\,\mathrm{nA}$, $U_\mathrm{B} = +700\,\mathrm{mV}$, $I_\mathrm{stab} = 0.1\,\mathrm{nA}$, $U_\mathrm{stab} = -200\,\mathrm{mV}$, $U_\mathrm{mod,STS} = 13\,\mathrm{mV}$, $U_\mathrm{mod,map} = 40\,\mathrm{mV}$, $\tau = 3\,\mathrm{ms}$. The magnetic field in **a**, **b** was $B_\mathrm{ext} = +2.6\,\mathrm{T}$; in **c**, **d** $B_\mathrm{ext} = +1.8\,\mathrm{T}$. All measurements were done at $T = 4.2\,\mathrm{K}$ with a non- or weakly spin-polarized Cr bulk tip.

The data sets in Fig. 4.4 directly correlate the vacuum LDOS with the magnetic structure of the sample. The presence of the magnetic skyrmion strongly affects the measured spin-averaged vacuum LDOS: the localized non-collinear magnetic environment affects the electronic structure of the sample. This effect is not observed for the magnetic environment

at the skyrmion edge in Fig. 4.4 **d** which only slightly deviates from the collinear ferromagnet. The skyrmion is therefore electronically distinct from its ferromagnetic surroundings. With the STS sequence in Fig. 4.4 **d**, one can also rule out a native defect within the surface as the cause of the LDOS change: if a defect would lead to the observed change of the vacuum LDOS, the change would also be visible in case of the absent skyrmion which is not the case.

4.1.4. STS on the spin spiral

So far, the effect of the magnetic environment on the spin-averaged vacuum LDOS of skyrmions was investigated. In general, this effect should be present in any non-collinear spin structure. A related structure is the spin spiral in PdFe/Ir(111) at $B_{\mathrm{ext}} = 0\,\mathrm{T}$, which serves as another test system. Based on the results of the last sections, the LDOS undergoes a change if the magnetic environment varies. If the magnetic environment is constant as, e.g. in a homogeneous spin spiral, the effect is the same over the whole magnetic structure. An inhomogeneous spiral with varying nearest neighbor angles should therefore exhibit the effect. Furthermore, the observed effect on the vacuum LDOS should be qualitatively similar to the observation of the skyrmion but less distinct compared to Fig. 4.3.

The electronic contrast as in Fig. 4.1 **a** can be observed for the spin spiral on both fcc-PdFe and hcp-PdFe as shown in Fig. 4.5: an overview (**a** and **e**) and zoomed-in regions (**b** and **f**) of a hcp-PdFe (top row) and a fcc-PdFe (bottom row) island are shown together with their corresponding line sections (**c** and **g**)[2]. In addition, single spectra were measured on the maxima and the minima of both spirals as shown in Fig. 4.5 **d** and **h**, together with the ferromagnetic spectrum as a reference[3]. The observed trends are qualitatively similar for both Pd stackings but differ in magnitude. The spectra measured on the spiral's maxima (blue) resemble the FM spectrum (black) but are slightly shifted towards higher energy. The STS on the minima show similar trends as the STS measured at the skyrmion center at low fields and depend on the stacking (cf. Fig. 4.6): a major peak is found at a slightly higher energy with a decreased intensity and a modified shoulder at around +500 mV. The observed spatial variation of the spin spiral vacuum LDOS supports the idea of a locally varying magnetic environment. Dupé *et al.* and Romming *et al.* [12, 14] report about a magnetic anisotropy in PdFe/Ir(111) with an out-of-plane easy axis. The anisotropy leads to a faster rotation of the in-plane spins compared to out-of-plane oriented spins, thereby causing a spatial variation of the magnetic environment which again is observed in the STS data.

[2] The line sections were spatially averaged over 12 lines (hcp-PdFe) and 20 lines (fcc-PdFe) in order to obtain a better signal-to-noise ratio.

[3] The FM spectrum was taken from the skyrmion STS in Sec. 4.1.2 which were measured with the same microtip as the measurements of the spin spiral.

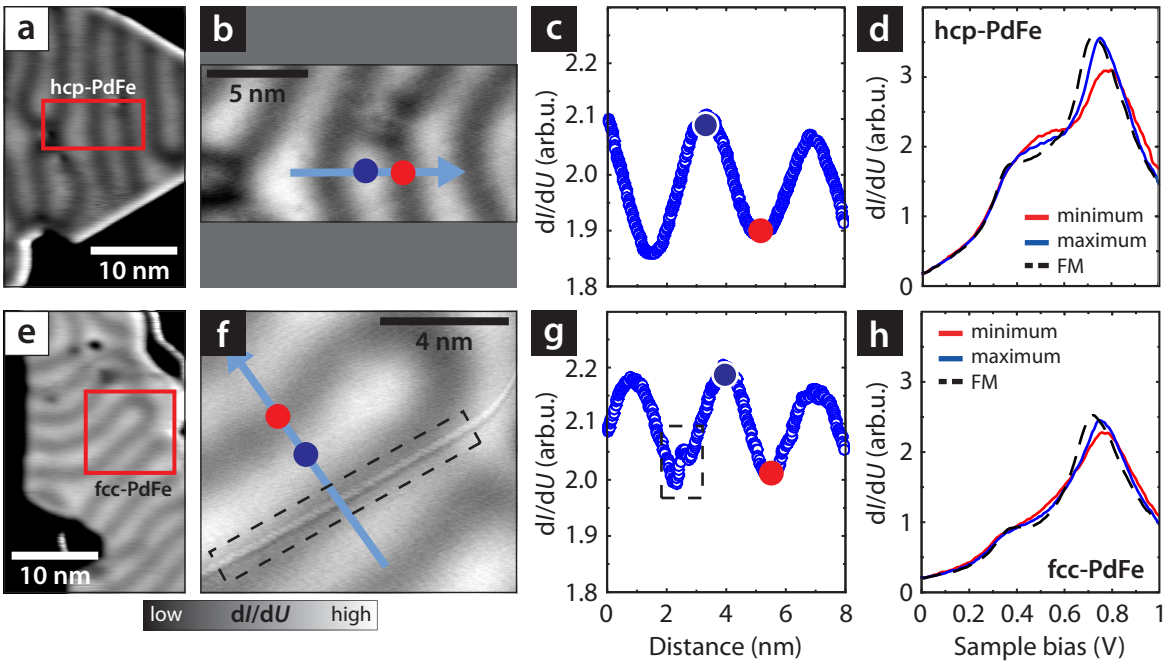

Figure 4.5.: Electronic structure of the spin spiral on hcp-PdFe and fcc-PdFe. **a**, **b** and **e**, **f**, $\mathrm{d}I/\mathrm{d}U$ maps of the spin spiral on hcp-PdFe (top row) and fcc-PdFe (bottom row). The blue arrows mark the positions of the line sections, the blue and red points the position of the STS data. **c** and **g**, line sections of the spin spirals. **d** and **h**, STS measured at the maximum and the minimum of the spin spiral and the FM spectrum as a reference. The dashed boxes in **f** and **g** mark a measurement artefact produced by the Specs Nanonis SPM controller [121]. The line section was averaged over 12 (hcp-PdFe) and 20 (fcc-PdFe) lines. The measurement parameters were $I_\mathrm{T} = 1\,\mathrm{nA}$, $U_\mathrm{B} = +700\,\mathrm{mV}$, $I_\mathrm{stab} = 1\,\mathrm{nA}$, $U_\mathrm{stab} = -1\,\mathrm{V}$, $U_\mathrm{mod,STS} = 7\,\mathrm{mV}$, $U_\mathrm{mod,map} = 40\,\mathrm{mV}$,$\tau = 10\,\mathrm{ms}$, $B_\mathrm{ext} = 0\,\mathrm{T}$, and $T = 4.2\,\mathrm{K}$. The measurement was done with the same non- or weakly spin-polarized Cr bulk tip as in Fig. 4.3.

4.2. The non-collinear magnetoresistance effect (NCMR)

This section introduces the non-collinear magnetoresistance effect (NCMR) which is the origin of the change in the spin-averaged vacuum LDOS due to the non-collinearity of the local magnetic environment. The effect is analyzed and interpreted in terms of a phenomenological model for the skyrmion center and the region around it. In addition, the main results of a theoretical study [26, 125] which were done at the University of Kiel [126] are presented in order to complement the description of the NCMR effect.

4.2.1. A phenomenological approach to NCMR

Section 4.1 describes a large difference between the vacuum LDOS of the FM and the skyrmion center. The sole distinction between the spin-averaged spectra of the FM and the skyrmion center is the magnetic environment around each STS position. All magnetic moments within the ferromagnet are collinear whereas the environment within a skyrmion is always non-collinear and the detailed spin orientation depends on the position on the skyrmion. The connection between the magnetic non-collinearity and the observed resistance change can be called non-collinear magnetoresistance effect (NCMR). This fundamental effect has not yet been considered before in the interpretation of (SP-)STM measurements. The physical origin of the NCMR is a mixing of spin-up and spin-down channels due to the local non-collinear environment (cf. Sec. 4.2.3 and [26]). With this, three main properties of the skyrmion electronic structure can already be identified:

1. The spin-averaged vacuum LDOS is correlated to the magnetic structure of the skyrmion.

2. The skyrmion is electronically different to the environment in which it is embedded.

3. The electronic structure is connected to the non-collinearity of the local environment.

For a quantitative treatment of the NCMR, the spin distribution within the skyrmion is needed. The description of the spins in hcp-PdFe is given in [14]

$$\vec{m}(\vec{r},c,w) = \begin{pmatrix} -\sin\left(\theta\left(\vec{r},c,w\right)\right)\cdot x/\left|\vec{r}\right| \\ -\sin\left(\theta\left(\vec{r},c,w\right)\right)\cdot y/\left|\vec{r}\right| \\ \cos\left(\theta\left(\vec{r},c,w\right)\right) \end{pmatrix} \tag{4.1}$$

with the polar angle $\theta(\vec{r},c,w)$ as

$$\theta(\vec{r},c,w) = \sum_{+,-} \arcsin\left(\tanh\left(\frac{-\left|\vec{r}\right| \pm c}{w/2}\right)\right), \tag{4.2}$$

c and w being free parameters and $r = |\vec{r}| = \sqrt{(x-x_0)^2+(y-y_0)^2}$. In 1D, $\theta(x,c,w)$ describes two 180° domain walls located at $\pm c$ with a width w. The field dependent parameters $c = c(B)$ and $w = w(B)$ have been determined for a skyrmion on hcp-PdFe in [14]. Using the spin distribution in Eq. 4.1, the skyrmion can be analyzed in detail: The central spin of a skyrmion is embedded in an isotropic (symmetric) non-collinear surrounding whereas all other spins have an *an*isotropic (asymmetric) spin distribution around them, i.e. an anisotropic non-collinear environment (cf. Fig. 4.10). These two cases are investigated in the following.

4.2.2. NCMR in a locally isotropic non-collinear environment

The spin at the skyrmion center is embedded in an isotropic (symmetric) non-collinear environment at which all nearest neighbor angles relative to the central spin are the same. The connection between the vacuum LDOS and the local degree of non-collinearity can easily be studied by measuring spectra at the skyrmion center at different magnetic field values (meaning different degrees of non-collinearity). The result of this measurement on hcp-PdFe is shown in Fig. 4.6: **a** shows spectra measured at the skyrmion center and the FM (as a reference) of three differently sized skyrmions (topography and $\mathrm{d}I/\mathrm{d}U$ maps are shown in Fig. 4.6 **b** and **c** to **e**, respectively). Similar to Fig. 4.3, all center STS data show two peaks. The peaks change while increasing the magnetic field. This is in agreement with the $\mathrm{d}I/\mathrm{d}U$ maps, which also show a change at the skyrmion center. In addition, the skyrmion changes its appearance from a large ring-like shape and a low contrast at $-1\,\mathrm{T}$ (**c**) towards a small single depression and a high contrast at $-2.5\,\mathrm{T}$ (**e**). Two major trends are found in the vacuum LDOS for the higher energy peak (relative to the FM peak) in dependence of the decreasing skyrmion size: the peak shifts towards higher energies and decreases in intensity. The lower energy peak shows a minor change: the peak keeps its position and increases slightly in intensity while the skyrmion diameter decreases.

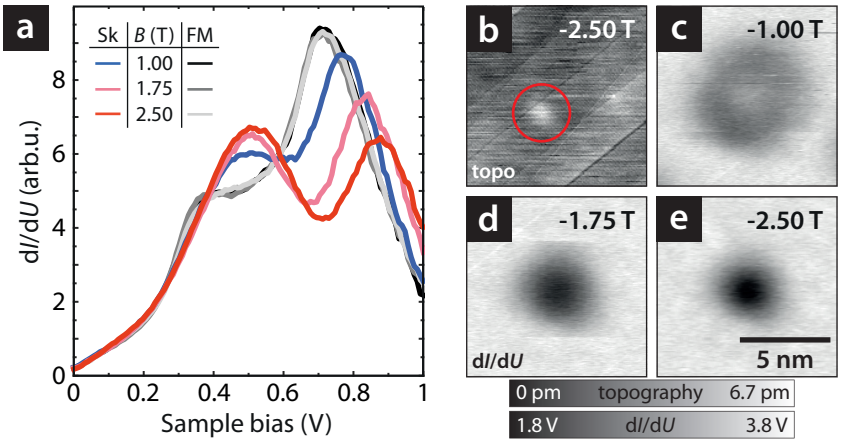

Figure 4.6.: STS measured at the skyrmion center at different magnetic fields on hcp-PdFe. **a**, Single point spectra measured at the skyrmion center at various field values. The FM spectra are also shown as a reference. **b**, constant-current image of the skyrmion on which the STS data in **a** were measured. The red circle marks the in-layer defect to which the skyrmion is pinned. **c** to **e**, $\mathrm{d}I/\mathrm{d}U$ maps with the same contrast range showing the magnetic state of the skyrmion used in **a** at various field values. The measurement parameters of the $\mathrm{d}I/\mathrm{d}U$ maps were: $I_\mathrm{T} = 1\,\mathrm{nA}$, $U_\mathrm{B} = +700\,\mathrm{mV}$, $I_\mathrm{stab} = 0.2\,\mathrm{nA}$; single point STS: $U_\mathrm{stab} = -300\,\mathrm{mV}$, $U_\mathrm{mod} = 20\,\mathrm{mV}$, $\tau = 3\,\mathrm{ms}$, and $T = 4.2\,\mathrm{K}$. The measurement was done with a W tip.

This peak change can be qualitatively understood using Fig. 4.7: the polar angle $\theta(x)$ of the magnetic moments relative to the surface normal (**a**) and the nearest neighbor angle $\alpha_{ij}(\vec{r} = \vec{r}_\mathrm{center}, B) = \alpha_\mathrm{c}$ at the isotropic skyrmion center (**b**) are plotted for various magnetic

field values (calculation according to [14]). The shape of $\theta(x)$ in Fig. 4.7 **a** strongly depends on the magnetic field value: with increasing magnetic field, the in-plane part and the position of the maximal slope moves towards the skyrmion center at $x = 0\,\mathrm{nm}$ and the skyrmion size decreases. The nearest neighbor angle at the skyrmion center at $x = 0\,\mathrm{nm}$ in Fig. 4.7 **b** scales linearly with the magnetic field.

The nearest neighbor angle α_c can be used for a more detailed description of the observed variation of the vacuum LDOS at the skyrmion center, together with two new quantities. The first quantity is the high energy peak's shift $\Delta E(\vec{r}, B)$ which is calculated by

$$\Delta E(\vec{r}, B) = E_\mathrm{Sk}(\vec{r}, B) - E_\mathrm{FM}(\vec{r}_\mathrm{FM}, B) \tag{4.3}$$

with the energy of the higher energy peak of the skyrmion $E_\mathrm{Sk}(\vec{r}, B)$ at position $\vec{r}$, and the energy of the main peak of the ferromagnetic vacuum LDOS $E_\mathrm{FM}(\vec{r}_\mathrm{FM}, B)$ at positon $\vec{r}_\mathrm{FM}$ outside the skyrmion; both measured at the same magnetic field value B. For the isotropic skyrmion center, the energy shift becomes $\Delta E(\vec{r}, B) = \Delta E(\vec{r} = \vec{r}_\mathrm{center}, \alpha_\mathrm{c}(B)) = \Delta E(\alpha_\mathrm{c})$. The second important quantity for the description of the variation of the vacuum LDOS is the intensity change $\Delta I(\vec{r}, B)$ of the high energy peak, which is calculated analogously to $\Delta E(\vec{r}, B)$ in Eq. 4.3. For the isotropic skyrmion center, the intensity change becomes $\Delta I(\vec{r}, B) = \Delta I(\vec{r} = \vec{r}_\mathrm{center}, \alpha_\mathrm{c}(B)) = \Delta I(\alpha_\mathrm{c})$. The peak energies and intensities were obtained from Lorentzian fits[4] to the peaks. The dependence of $\Delta E(\alpha_\mathrm{c})$ and $\Delta I(\alpha_\mathrm{c})$ on the nearest neighbor angle is shown in Fig. 4.8[5]: **a** shows the energy shift $\Delta E(\alpha_\mathrm{c})$ of the high energy peak in dependence of the nearest neighbor angle α_c, **b** links the intensity change $\Delta I(\alpha_\mathrm{c})$ of the same peak to α_c. The intensity change $\Delta I(\alpha_\mathrm{c})$ of each data point in Fig. 4.8 **b** was also normalized to the intensity of each data point's FM peak in order to account for the individual specifics of each microtip.

The energy shift $\Delta E(\alpha_\mathrm{c})$ in Fig. 4.8 **a** seems to increase linearly with an increasing nearest neighbor angle α_c. This scaling is also found for the high peak's intensity $\Delta I(\alpha_\mathrm{c})$ in Fig. 4.8 **b**, but with a decreasing trend. Interestingly, the energy shift $\Delta E(\alpha_\mathrm{c})$ seems not to depend on the individual specifics of the microtip since all data points follow the linear trend in Fig. 4.8 **a**, although they were measured with different microtips. The linearity in α_c is less distinct for $\Delta I(\alpha_\mathrm{c})$ in Fig. 4.8 **b**: only the data points of W tip #1 show a linear dependence with a vanishing intensity change for the FM. The larger variation of $\Delta I(\alpha_\mathrm{c})$ might be due to additional intensity contributions by non-zero spin-polarizations of the different magnetic Cr tips and the W tip #2. Although W is a non-magnetic material, W tip #2 probably picked up magnetic material in a tip crash which led to a non-zero spin-polarization. However, it

[4] The Lorentzian fit was a heuristic choice for the peak shape. The fit was done within a narrow energy interval around a peak. The main goal was the extraction of the peak value and not the reproduction of the whole peak shape. The fitting could also be done with a Gauss fit.

[5] The data points in Fig. 4.8 were extracted from the data in Fig. 4.6 **a**, Fig. 4.3 **c**, Fig. 4.4 **b** and others (not shown) and were obtained using several weakly or non–spin-polarized Cr bulk and W tips.

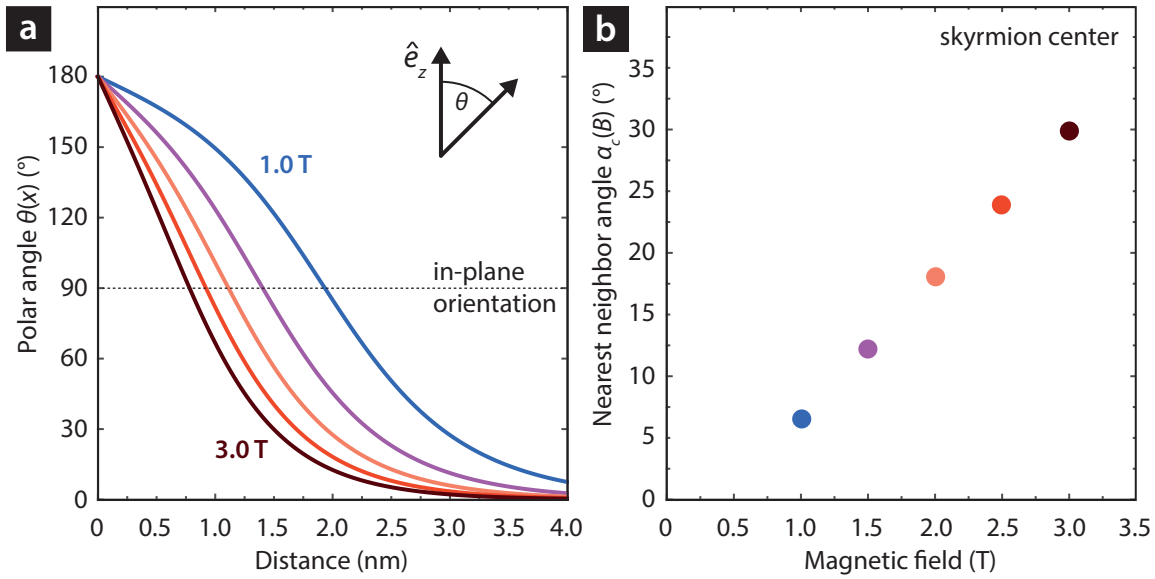

Figure 4.7.: Polar angle in dependence of the distance, and the nearest neighbor angle at the skyrmion center for various magnetic fields. a, The polar angle $\theta(x)$ in dependence of the position on the skyrmion going from the skyrmion center ($x = 0\,\text{nm}$) to the FM. $\theta(x)$ was calculated using Eq. 4.1 which is taken from [14]. **b**, Angle $\alpha_\text{c} = \theta(x_\text{NN})$ between the magnetic moment at the skyrmion center and its nearest neighbor at $x_\text{NN} = 0.27\,\text{nm}$ which is the lattice constant of Ir(111).

seems that at least the linear scaling of the energy shift is an intrinsic property of the NCMR effect of this particular system hcp-PdFe.

To summarize, the changes of the vacuum LDOS which are described by the energy shift $\Delta E(\alpha_\text{c})$ and $\Delta I(\alpha_\text{c})$ at the isotropic skyrmion center scale linearly with the local non-collinearity described by the nearest neighbor angle α_c.

4.2.3. A brief introduction to the theory of NCMR

For the treatment of an anisotropic non-collinear environment it is instructive to briefly present the results of a theoretical study by Fabian Otte, Dr. Bertrand Dupé and Prof. Dr. Stefan Heinze from the University of Kiel [126]. This is done in this short subsection. The details of the theoretical treatment can be found in Hanneken *et al.* [26] and in the PhD thesis of Fabian Otte [125]. The basic idea of the NCMR related change of the vacuum LDOS is a hybridization of both spin channels due to the non-collinearity of nearest neighboring spins. This idea is modelled using a simple tight-binding model, its model parameters were chosen in order to fit the density functional theory (DFT) calculations of the FM vacuum LDOS and the experiment. The tight-binding Hamiltonian H_TB is given by

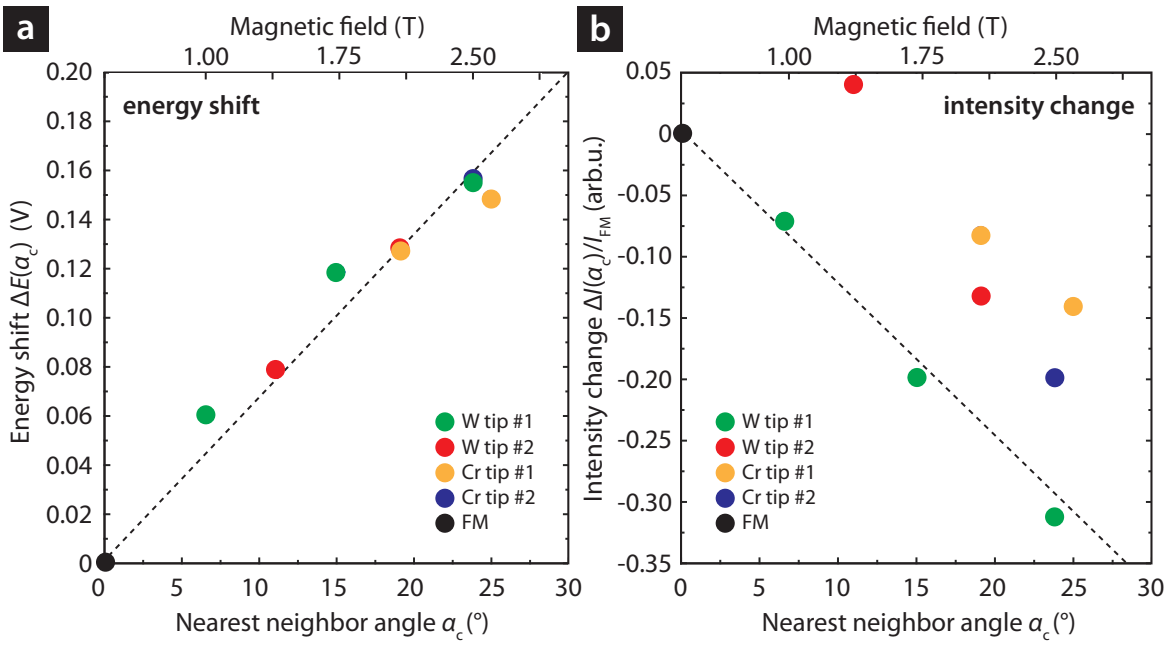

Figure 4.8.: Energy shift and intensity change of the high energy peak in an isotropic non-collinear environment. **a**, Energy shift $\Delta E(\alpha_c)$ of the high energy peak versus various nearest neighbor angles at the skyrmion center. The values were obtained using different microtips. **b**, Normalized intensity change $\Delta I(\alpha_c)/I_{FM}$ in dependence of the nearest neighbor angle at the skyrmion center. Both energies and intensites were obtained by fitting a Lorentzian to the high energy peak of each spectrum. The change of $\Delta E(\alpha_c)$ was obtained by substracting the FM values, $\Delta I(\alpha_c)$ was further normalized to the FM intensity. The mean angle at the skyrmion center was taken from Fig. 4.7 **b**. The dashed lines are a guide to the eye.

$$H_{TB} = \begin{pmatrix} H_0 & V(\alpha_{ij}) \\ V(\alpha_{ij}) & H_0 \end{pmatrix} \tag{4.4}$$

with H_0 as the unperturbed atomic Hamiltonian and $V(\alpha_{ij})$ as the interaction potential between the nearest neighboring sites i and j. The unperturbed Hamiltonian H_0 is given by

$$H_0 = \begin{pmatrix} \epsilon_\uparrow & 0 \\ 0 & \epsilon_\downarrow \end{pmatrix} \tag{4.5}$$

with $\epsilon_\uparrow$ and $\epsilon_\downarrow$ being the on-site energies for the spin-up ($\uparrow$) and spin-down ($\downarrow$) state, respectively. The interaction between neighboring sites is described by the potential $V(\alpha_{ij})$

$$V(\alpha_{ij}) = \begin{pmatrix} t_\uparrow \cos(\alpha_{ij}/2) & -t_{\uparrow\downarrow} \sin(\alpha_{ij}/2) \\ t_{\downarrow\uparrow} \sin(\alpha_{ij}/2) & t_\downarrow \cos(\alpha_{ij}/2) \end{pmatrix} \tag{4.6}$$

with α_{ij} being the angle between neighboring spins i and j, $t_\uparrow$, $t_\downarrow$ being hopping parameters, $t_{\uparrow\downarrow} = -t_{\downarrow\uparrow}$, describing the nearest neighbor hopping matrix element between the spin-up and spin-down states. In the collinear case ($\alpha_{ij} = 0°$), all off-diagonal elements in $V(\alpha_{ij})$ vanish and the electron hopping is restricted to transitions between same bands, no spin-mixing occurs. With an increasing non-collinearity between nearest neighbors ($|\alpha_{ij}| > 0°$), the off-diagonal elements gain importance, a mixing of spin channels occurs and transitions between bands of different spin character are allowed. The mixing is at a maximum for $|\alpha_{ij}| = 180°$ (anti-parallel alignment). The hopping parameters $t_\uparrow$ and $t_\downarrow$ were chosen according to the majority (green) and minority (red) LDOS which were calculated by DFT [12, 26] and are shown in Fig. 4.9 **a**. The spin-resolved LDOS differs for the two spin types in the energy interval of interest between E_F and 1 eV. The majority channel shows minor features, the minority channel exhibits a strong peak around 0.9 eV.

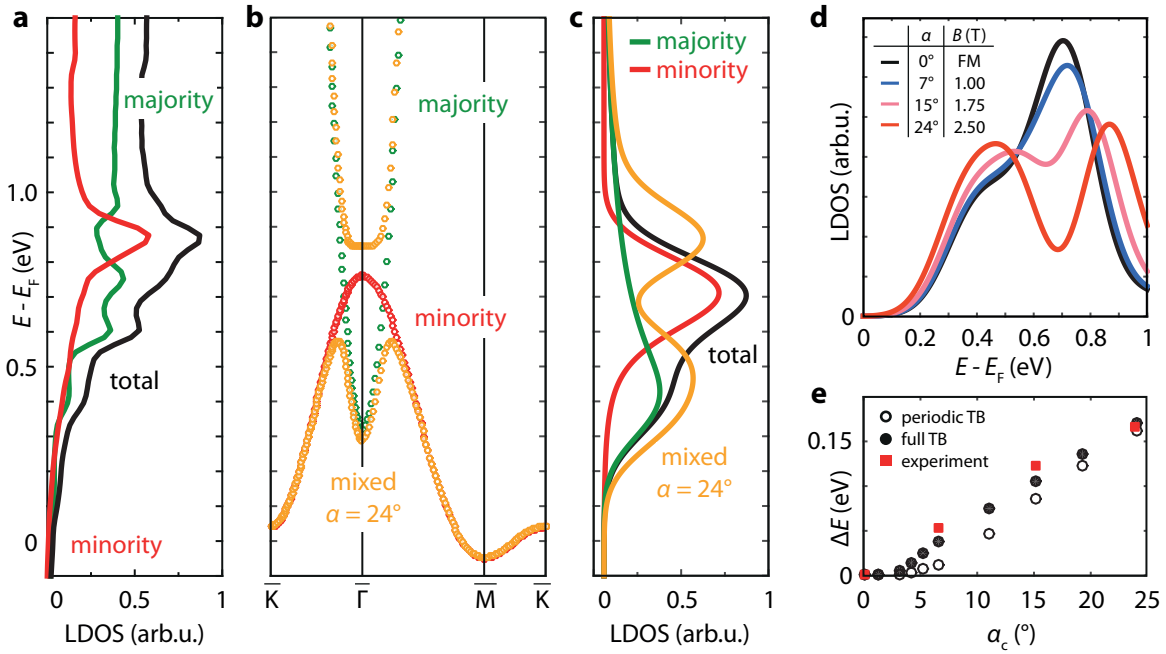

Figure 4.9.: Band structure and corresponding vacuum LDOS of the FM and a 'model skyrmion'. **a**, Spin-resolved (red and green) and spin-averaged (black) vacuum LDOS of hcp-PdFe/Ir(111) obtained by density functional theory calculations. **b**, Band structure calculated from a periodic tight-binding model. **c**, Calculated vacuum LDOS based on the band structure in **b**. The vacuum LDOS shows the spin-resolved (red and green), the spin-averaged (black) and the spin-mixed (orange) contributions. **d**, Calculated spin-mixed vacuum LDOS at the skyrmion center for different magnetic field values. **e**, Spatially resolved energy shift. From Hanneken *et al.*, Nature Nanotechnology 10, 1039-1042 (2015) [26].

To simplify the further analysis, the potential $V(\alpha_{ij})$ is assumed to be equal at all considered sites ('model skyrmion'). The resulting periodic potential leads to the band structure in Fig. 4.9 **b**. For the unperturbed case, the majority (green) and minority (red) bands show two band crossings close to $\overline{\Gamma}$. This is changed in case of a non-zero potential $V(\alpha_{ij} = 24°)$: the mixed bands now show an avoided crossing in the vicinity of $\overline{\Gamma}$. Using this band structure, the vacuum LDOS is calculated and shown in Fig. 4.9 **c**. The resulting spin-mixed vacuum LDOS (orange) exhibits two major peaks compared to the single peak of the spin-averaged unperturbed LDOS (black). This is in good agreement with the measured vacuum LDOS, e.g. in Fig. 4.3 **c**. To study the dependence of the LDOS on the non-collinearity of the environment, the strength of $V(\alpha_{ij})$ was varied by choosing different spin-mixing angles α_{ij}. The result in Fig. 4.9 **d** shows a qualitatively similar trend as the field dependent measurement in Fig. 4.6 **a**: the high energy peak shifts towards higher energies and decreases in intensity with an increasing nearest neighbor angle α_{ij}. This agreement is also found if the shift of the high energy peak $\Delta E(x)$ is linked to α_c at the skyrmion center and the magnetic field is varied (cf. Fig. 4.8). The result is shown in Fig. 4.9 **e**. Both measurement and tight-binding calculation (periodic TB as described in this paragraph and a full TB model considering the full non-collinear spin structure according to Eq. 4.1, see [26]) show a similar linearity with a better agreement of the full TB model to the experiment. To summarize, this simple tight-binding approach reproduces the measured vacuum LDOS not only qualitatively but also quantitatively in good agreement and therefore gives a reasonable explanation of the physical origin of the NCMR effect.

4.2.4. NCMR in a locally *an*isotropic non-collinear environment

The isotropic non-collinear surrounding at the skyrmion center is the special case of the more general *anisotropic* (asymmetric) non-collinear environment. This anisotropic environment is the typical environment within the skyrmion besides its center and the FM. The difference between the isotropic and anisotropic non-collinear environment is illustrated in Fig. 4.10. At the isotropic skyrmion center, the non-collinearity is sufficiently well described by the simple nearest neighbor angle α_c, due to the six-fold symmetry of the environment (cf. Fig. 4.10 **a**). Besides the skyrmion center, the local environment typically does not exhibit any symmetry (cf. Fig. 4.10 **b**). The nearest neighbor angles α_{ij} (angles between the central magnetic moment i and its six nearest neighbors j) vary within the local environment which is now anisotropically non-collinear. The description of the NCMR by the high peak's energy shift $\Delta E(\vec{r}, B)$ and intensity change $\Delta I(\vec{r}, B)$ becomes more complicated in this case due to a different spin-mixing. In the locally varying complex environment, a more general description of NCMR requires two quantities in order to account for the local variation of the nearest neighbor angles α_{ij}. The first quantity describes the *non-collinearity*. In a simple approach, the non-collinearity is the deviation from $\alpha_{ij} = 0$, which describes the deflection of the spins within the local environment from a collinear alignment. The non-collinearity is described by using the *mean* nearest neighbor angle $\langle\alpha\rangle$ which is the average value of the six angles α_{ij} as a simple heuristic model

$$\langle\alpha\rangle = \langle\alpha_i(\vec{r},B)\rangle = \frac{1}{6}\sum_{j=1}^{6}\alpha_{ij}(\vec{r},B) = \frac{1}{6}\sum_{j=1}^{6}\angle\left[\vec{m}_i(\vec{r},B),\vec{m}_j(\vec{r}+\vec{r}_j,B)\right] \tag{4.7}$$

with α_{ij} as the angle between the central reference magnetic moment $\vec{m}_i(\vec{r},B)$[6] and the nearest neighbor moment $\vec{m}_j(\vec{r}+\vec{r}_j,B)$ within the hexagonal environment of $\vec{m}_i(\vec{r},B)$. This generalized description of the non-collinearity by the mean angle $\langle\alpha\rangle$ simplifies to the nearest neighbor angle α_c in case of an isotropic environment as it is found at the skyrmion center (cf. Sec. 4.2.2): $\langle\alpha_i(\vec{r}=\vec{r}_\mathrm{center},B)\rangle = \frac{1}{6}\sum_{j=1}^{6}\alpha_{i=\mathrm{c},j}(B) = \alpha_\mathrm{c}(B)$.

The second important quantity accounts for the *anisotropy* of the non-collinearity which is the deviation of all six α_{ij} from $\langle\alpha\rangle$. Again, as a simple heuristic model the anisotropy of the non-collinearity can be characterized by the mean angle's standard deviation $\sigma_{\langle\alpha\rangle}$ as e.g. in [127], section 4.4.9, pages 74-77:

$$\sigma_{\langle\alpha\rangle} = \sigma_{\langle\alpha_i(\vec{r},B)\rangle} = \sqrt{\frac{1}{6}\sum_{j=1}^{6}\left|\alpha_{ij}(\vec{r},B) - \langle\alpha(\vec{r},B)\rangle\right|^2} \tag{4.8}$$

with $\langle\alpha(\vec{r},B)\rangle$ as the mean angle, $\alpha_{ij}(\vec{r},B)$ as the angle between the central reference moment i and its j-th nearest neighbor. The standard deviation of the mean angle suits well for the description of the anisotropic non-collinearity as it results to zero for the collinear FM and the isotropically non-collinear skyrmion center, and is non-zero everywhere else.

Using the definitions in Eq. 4.7 and Eq. 4.8 together with the spin distribution given in Eq. 4.1, the theoretical non-collinearity $\langle\alpha\rangle$ and anisotropy of the non-collinearity $\sigma_{\langle\alpha\rangle}$ can be calculated for the field range of 1 T to 3 T. The result is shown in Fig. 4.11 as color-coded waterfall plots: **a** shows the polar angle θ which is shown for comparison (cf. Fig. 4.7), **b** shows the mean angle $\langle\alpha\rangle$ whereas **c** shows the mean angle's standard deviation $\sigma_{\langle\alpha\rangle}$. At a low magnetic field of 1 T, the maximal mean angle $\langle\alpha\rangle$ is $\sim$15° and is found around the in-plane part ($|x| = \sim$1.8 nm) of the skyrmion (black lines), the magnetic moments at the skyrmion center are only slightly tilted relative to the surrounding moments ($\langle\alpha\rangle = \sim$7°). The highest spin mixing is therefore outside the skyrmion center which is in agreement with the observed ring-like shape of a skyrmion at -1 T in Fig. 4.6 **c**. The position and the maximal value of the mean angle changes with increasing magnetic field: the maximum (and with it the maximal spin-mixing) moves towards the skyrmion center and increases from a value of $\sim$15° at 1 T outside the skyrmion center to $\sim$30° at 3 T at the center. This trend is in agreement with the observed depression-like shape of a skyrmion at -2.5 T in Fig. 4.6 **e**. In contrast to the mean angle, the standard deviation in Fig. 4.11 **c** changes differently: the maximum of $\sigma_{\langle\alpha\rangle}$ is clearly found off the center in the vicinity of the in-plane area for

[6] not to be confused with the magnetic moment at the skyrmion center

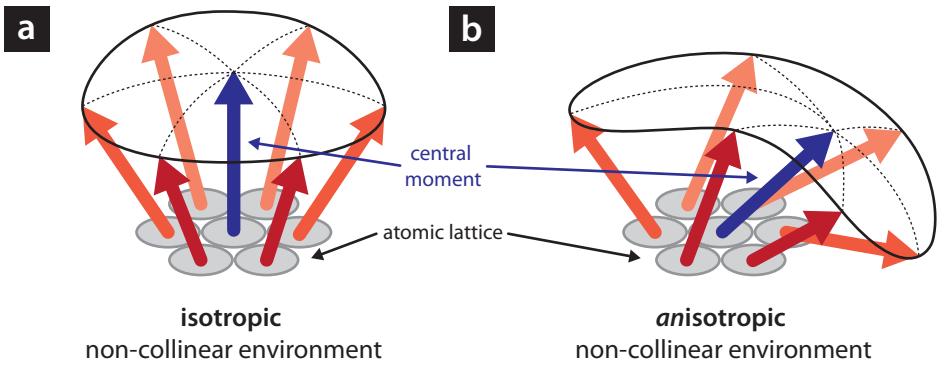

Figure 4.10.: Schematic illustrating the difference between an isotropic and an anisotropic non-collinear environment. **a**, Isotropic non-collinear environment as found at the skyrmion center (same angles to nearest neighbors). **b**, Example of an *an*isotropic non-collinear environment (different angles to nearest neighbors). The blue arrow depicts a magnetic moment which is surrounded by six nearest neighbors (red).

the whole calculated field range. Furthermore, $\sigma_{\langle\alpha\rangle}$ separates the isotropic regions of the FM and the skyrmion center. The value of $\sigma_{\langle\alpha\rangle}$ does only weakly depend on the magnetic field compared to $\langle\alpha\rangle$. While the maximum of $\sigma_{\langle\alpha\rangle}$ increases by ∼14 % from 3.8° to 4.4°, the maximum value of $\langle\alpha\rangle$ doubles from ∼15° to ∼30° if B is raised from 1 T to 3 T.

The consequences of this rather theoretical discussion of $\langle\alpha\rangle$ and $\sigma_{\langle\alpha\rangle}$ for $\Delta E(x, B)$ and $\Delta I(x, B)$[7] are investigated in the following. Two skyrmions at $B_{\text{ext}} = -1$ T (big skyrmion) and at $B_{\text{ext}} = -2.5$ T (small skyrmion) are compared. In order to get access to the spatial variation of $\Delta E(x, B)$ and $\Delta I(x, B)$, spectra were measured at various positions along a mirror plane of the skyrmion using the same W tip as in Fig. 4.6. In addition, STS data were measured on a second skyrmion at −2.5 T using the non–spin-polarized Cr bulk tip of Fig. 4.3 and Fig. 4.5. The W tip spectra are shown as waterfall plots in Fig. 4.12 **a** and **b**. For both skyrmions, a smooth transition from the FM vacuum LDOS (plot edges) to the spin-mixed LDOS (towards the center of the plot) is observed. The intensity drop in Fig. 4.12 **b** close to the skyrmion center (left side) is most likely due to a native defect within the surface. However, the defect only seems to affect the intensity and not the energy shift (cf. Fig. 4.13). Figure 4.12 **c** and **d** show the spatially resolved energy shift $\Delta E(x, B)$ of the high energy peak measured with the W tip (red) and the Cr bulk tip (blue)[8]. The big skyrmion at −1 T in Fig. 4.12 **c** shows a smaller energy shift with two maxima off the center compared to a larger shift and a centered maximum for both small skyrmions in **d**. The energy shift of the skyrmions at −2.5 T measured with the W and the Cr tip look basically

[7] Similar to Sec. 4.2.2, the energy shifts and intensity changes were obtained from Lorentzian fits to the high energy peak. In a second step, the energy's and intensity's reference value of the FM peak were substracted from the fit result.

[8] The plotted values are raw values and were not rescaled or shifted in energy in order to fit the W tip data.

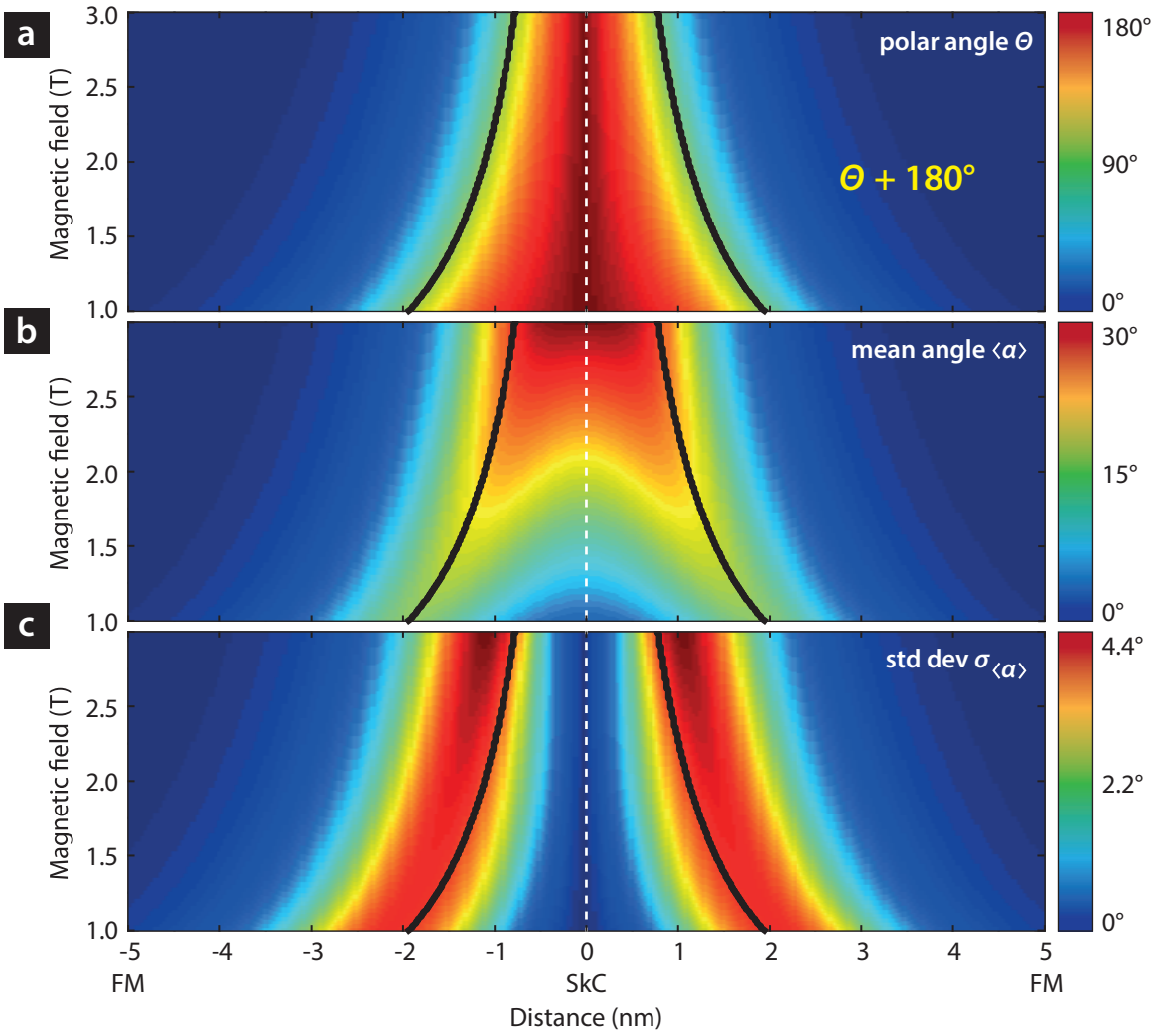

Figure 4.11.: Calculated polar angle, mean angle and its standard deviation in an anisotropic non-collinear environment for various magnetic fields. **a**, Polar angle θ as in Fig. 4.7, calculated for various magnetic field values. Note that the offset of θ of 180° at the right side of the plot was omitted in order to maintain the symmetric features of θ. **b**, Theoretical mean angle $\langle\alpha\rangle$ as a measure of the non-collinearity. The values were obtained using Eq. 4.7. **c**, Theoretical standard deviation $\sigma_{\langle\alpha\rangle}$ as a measure of the anisotropy of the non-collinearity, calculated by Eq. 4.8. The black lines indicate the positions of the maximal in-plane component in the skyrmion. The skyrmion center (SkC) is found at the center of the plot at $x = 0\,\mathrm{nm}$.

the same, which is in agreement with the analysis of the isotropic environment showing that $\Delta E(\vec{r} = \vec{r}_{\text{center}}, B)$ does not depend on the microtip used.

The spatial variation of the energy shift can be explained by the calculated mean angles in Fig. 4.12 **e** and **f** (which are line sections of Fig. 4.11 **b**). Using the mean angle for the description of the energy shift is reasonable based on the following arguments: according to Fig. 4.8 **a**, the energy shift measured at the skyrmion center is proportional to the nearest neighbor angle α_{c}. Considering the fact that the skyrmion center is surrounded by six nearest neighbors, the energy shift actually scales with all six nearest neighbor angles α_{ij}, which can be simplified to an "effective" angle, the mean angle $\langle\alpha\rangle$. The spatial variation of the energy shift $\Delta E(\vec{r} = \vec{r}_{\text{center}}, B)$ should therefore depend on the mean angle $\langle\alpha\rangle$, even if the environment is not isotropic anymore.

The relationship between the experimental energy shift $\Delta E(x, B)$ and the theoretical mean angle $\langle\alpha\rangle$ becomes obvious, if Fig. 4.12 **c**, **d** and **e**, **f** are compared. The maximal mean angle of the big skyrmion in Fig. 4.12 **e** is $\sim$15° and found at the in-plane position which is the same as the experimentally observed position of the maximal $\Delta E(x, B)$ in Fig. 4.12 **c**. The smaller skyrmion at $-2.5\,\text{T}$ has a larger maximal mean angle of $\sim$25° which is located in the vicinity of the skyrmion center. Again, the experimental maximum of $\Delta E(x, B)$ matches the position of the calculated overall maximal mean angle $\langle\alpha\rangle$ (disregarding the two minor maxima). The difference of $\sim$10° between the maximal mean angles of the large and small skyrmion explains the difference in the respective maximal values of $\Delta E(x, B)$. The low local non-collinearity within the big skyrmion results in a lower NCMR effect and therefore in a lower energy shift $\Delta E(x, B)$ compared to the small skyrmion with a higher local non-collinearity and a higher NCMR effect. The matching positions of the maxima of $\langle\alpha\rangle$ and $\Delta E(x, B)$ and a qualitatively similar behavior of the experimental data in Fig. 4.12 **c** and **d**, as well as the calculated curves in Fig. 4.12 **e** and **f**, demonstrate that the mean angle reasonably describes the energy shift. The fact, that the experimental energy shift only shows one maximum instead of the two maxima in the calculated mean angle in Fig. 4.12 **f** might be due to a lack of spatial resolution between the STS positions or a lack of accuracy of the model which was used for the description of the magnetization of the skyrmion in the vicinity of the skyrmion center.

The description of the spatial intensity change $\Delta I(x, B)$ in Fig. 4.13 is more complex than the description of the spatial energy shift $\Delta E(x, B)$. For both skyrmion sizes, the extracted high-energy peak's intensities in Fig. 4.13 **c** and **d** decrease towards the skyrmion center and show two pronounced minima off the center. Due to the observed intensity change by a defect at the left side of Fig. 4.13 **b**, this side should be ignored in the following. However, in order to study the intensity change of a full skyrmion at this field value, the Cr tip data is evaluated[9]. This seems to be reasonable since the energy shifts of both Cr and W tip

[9]The intensity change of the Cr tip data was rescaled in order to account for different lock-in parameters, the different microtip and a possible (low) spin-polarization compared to the data of the W tip, and to fit the W tip data in Fig. 4.13 **d**.

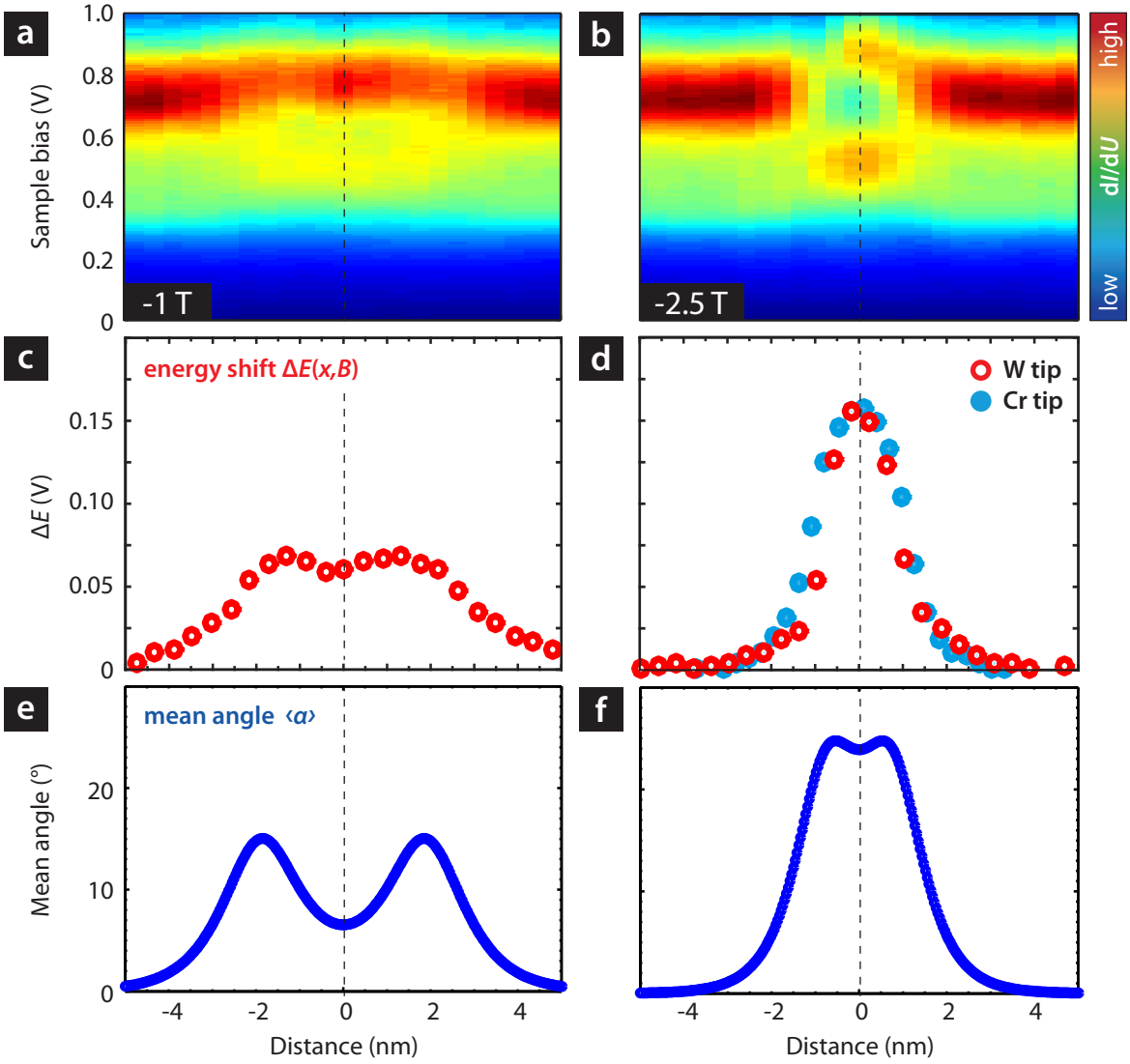

Figure 4.12.: Energy shift $\Delta E(x, B)$ of the high energy peak of the vacuum LDOS in dependence of the position on the skyrmion for two differently sized skyrmions on hcp-PdFe. **a** and **b**, Color-coded waterfall plots of a skyrmion at $-1\,\mathrm{T}$ (**a**) and $-2.5\,\mathrm{T}$ (**b**) measured with a W tip. The intensity drop in **b** close to the skyrmion center (left side) is probably due to a defect within the surface. **c** and **d**, Energy shift $\Delta E(x, B)$ calculated as the difference between the measured high peak's energy and the energy of the FM peak for a skyrmion measured with a W tip (red, same tip as in Fig. 4.6) and a Cr bulk tip (blue, same tip as in Fig. 4.3). **e** and **f**, Calculated mean angle using Eq. 4.7 and Eq. 4.1. The STS parameters for the W tip and Cr tip measurement are the same as in Fig. 4.6 and Fig. 4.3, respectively. The W tip data in **a** and **b** were measured with the same tip.

measurements in Figure 4.12 **d** are basically the same, although completely different tips were used. Based on this agreement, the intensity changes measured with the Cr tip (blue) and the W tip (red) are assumed to be comparable. Interestingly, $\Delta E(x, B)$ and $\Delta I(x, B)$ show a different behavior for the two differently sized skyrmions. While $\Delta E(x, B)$ and $\Delta I(x, B)$ resemble each other in case of the big skyrmion (cf. Fig. 4.12 **c** and Fig. 4.13 **c**, two extrema at similar positions), $\Delta E(x, B)$ and $\Delta I(x, B)$ differ for the small skyrmion (cf. Fig. 4.12 **d** and Fig. 4.13 **d**): $\Delta E(x, B)$ shows a single central extremum (maximum) whereas $\Delta I(x, B)$ shows two extrema (minima) off the skyrmion center for both W tip (only right side) and Cr tip (both sides).

The general intensity change can be explained using Fig. 4.8: $\Delta E(x, B)$ and $\Delta I(x, B)$ show a linear dependency on the non-collinearity of the isotropic environment (besides the microtip dependent offset of $\Delta I(x, B)$). Hence, the energy shift and intensity change are linked to each other in a way. The spatial variation of the energy shift $\Delta E(x, B)$ is well described by the mean angle $\langle\alpha\rangle$, the intensity change $\Delta I(x, B)$ should therefore scale similarly. Hence, the general intensity reduction of the high energy peak is an intrinsic property of the peak's behavior in a non-collinear environment and presumably a result of the spin mixing. This explanation of the spatial variation of $\Delta I(x, B)$ is supported by the similar behavior of $\Delta I(x, B)$ and $\langle\alpha\rangle$ for the big skyrmion at $-1\,\mathrm{T}$ in Fig. 4.13 **c** and **e**. However, the qualitative scaling of $\Delta I(x, B)$ with the mean angle $\langle\alpha\rangle$ fails to explain the occurance of the two minima in the vicinity of the skyrmion center at $-2.5\,\mathrm{T}$ in Fig. 4.13 **d**.

The explanation of these additional minima at $-2.5\,\mathrm{T}$ requires the anisotropy of the non-collinearity $\sigma_{\langle\alpha\rangle}$. The minima of $\sigma_{\langle\alpha\rangle}$ and $\langle\alpha\rangle$ in Fig. 4.13 **e** and **f**[10] match the minima of $\Delta I(x, B)$ in **c** and **d**. At the minima of $\sigma_{\langle\alpha\rangle}$ in Fig. 4.13 **e** and **f**, the angles to the nearest neighboring moments along the radial direction of the skyrmion are much larger than angles to nearest neighboring moments along the tangential direction. The minima of $\sigma_{\langle\alpha\rangle}$ therefore describe the positions of a maximal local anisotropy within the local non-collinear environment. As a consequence, the vacuum LDOS consists of contributions from the maximal variety of angles to the nearest neighbors around the maxima of $\sigma_{\langle\alpha\rangle}$.

With this correlation between $\Delta I(x, B)$ and $\sigma_{\langle\alpha\rangle}$ in mind, the physical reason behind the minimal intensity might be explained by a simple gedankenexperiment. Assuming the vacuum LDOS was separable into six peaks. Each peak results from the spin-mixing due to one of the six nearest neighbor's angles. In an isotropic environment with six equal nearest neighbor angles, all directions contribute the same way to the vacuum LDOS. The consequence is a sharp peak with a high intensity. In an anisotropic environment, the composed vacuum LDOS consists of six peaks with differently shifted energies due to the six different next neighbor angles. The resulting peak is therefore broadened and has a lower intensity than the sharp peak of the isotropic environment (cf. Fig. 4.15). This additional intensity decrease is always maximal outside the skyrmion center where the anisotropy of the

[10] Figure 4.13 **e** and **f** are line sections of the calculated standard deviation $\sigma_{\langle\alpha\rangle}$ in Fig. 4.11 **c**. Note that the y axis is inverted.

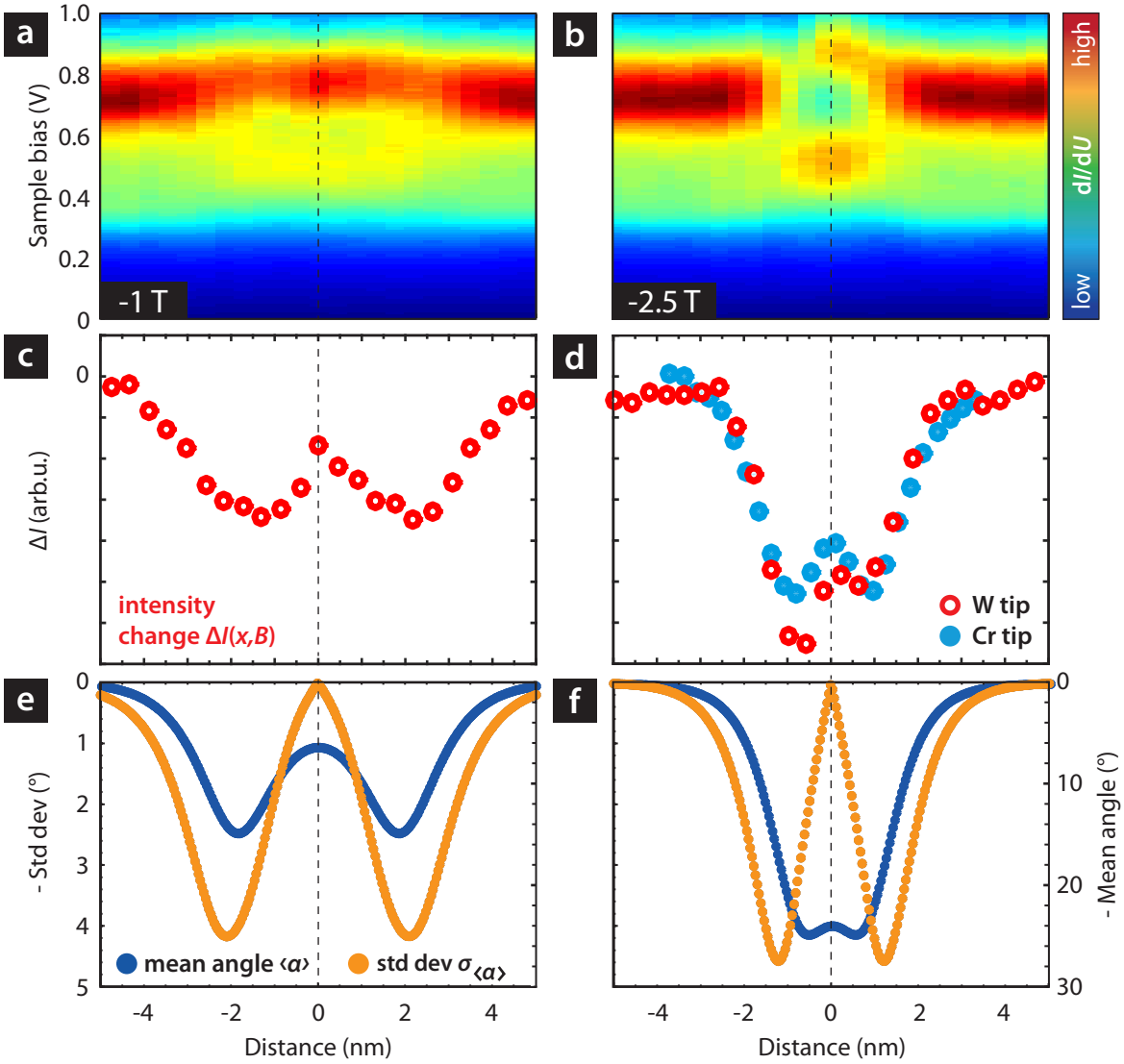

Figure 4.13.: Intensity change $\Delta I(x, B)$ of the high energy peak in dependence of the position on the skyrmion for two differently sized skyrmions on hcp-PdFe. **a** and **b**, Color-coded waterfall plots of a skyrmion at $-1\,\mathrm{T}$ (**a**) and $-2.5\,\mathrm{T}$ (**b**) measured with a W tip. The intensity drop in **b** close to the skyrmion center (left side) is probably due to a defect within the surface. **c** and **d**, Intensity change calculated as the difference between the measured high peak's intensity and the intensity of the FM peak. In contrast to the energy shift in Fig. 4.12 **d**, the intensity change of the W tip data is strongly affected by the defect in the left half of **d**. **e** and **f**, Calculated mean angle (blue) and standard deviation (orange). Note that the y axis is inverted in **e** and **f**. The STS parameters for the W tip and Cr tip measurements are the same as in Fig. 4.6 and Fig. 4.3, respectively.

non-collinearity $\sigma_{\langle\alpha\rangle}$ is maximal. As a consequence, the total intensity $\Delta I(x, B)$ change is a combination of the inherent intensity decrease of the high energy peak within an increasingly non-collinear environment (which scales with $\langle\alpha\rangle$) and an additional intensity decrease by a peak broadening due to the anisotropy of this non-collinear environment (which scales with $\sigma_{\langle\alpha\rangle}$). The effect of the anisotropy of the non-collinearity is not strong for the big skyrmion at $-1\,\mathrm{T}$: the additional intensity decrease only affects the depth and the width of the minima of $\Delta I(x, B)$, since the positions of the minima of $\sigma_{\langle\alpha\rangle}$ and $\langle\alpha\rangle$ match. The effect becomes important if $\langle\alpha\rangle$ and $\sigma_{\langle\alpha\rangle}$ change qualitatively different as in the case of the skyrmion at $-2.5\,\mathrm{T}$.

To summarize, the description of NCMR by the high peak's energy and intensity variation seems to be reasonable for both isotropic and anisotropic non-collinear environments. The energy shift $\Delta E(x, B)$ and intensity change $\Delta I(x, B)$ are linked to the local non-collinearity which is described by the mean angle $\langle\alpha\rangle$. This ansatz seems to be a good approach to quantify NCMR. However, in order to explain the positions of the additional centro-symmetric minima of $\Delta I(x, B)$ at high magnetic fields, the standard deviation of the mean angle $\sigma_{\langle\alpha\rangle}$ which is a measure of the local anisotropy of the non-collinearity is needed. This additional contribution to $\Delta I(x, B)$ is due to a peak broadening and decrease at positions with a maximal value of $\sigma_{\langle\alpha\rangle}$. This simple description of NCMR is a good means for a qualitative explanation of this effect without the need to perform complex calculations.

4.3. Contrast mechanisms in (SP-)STM: TMR, TAMR and NCMR

In the last sections, the effect of the NCMR on the vacuum LDOS was investigated. Theoretical STM images of skyrmions with a NCMR contrast can now be simulated by a Tersoff-Hamann model [106] and the mean angle $\langle\alpha\rangle$ description of Sec. 4.2.4. The spin distribution together with the parameters c and w were taken from [14]. A sketch of the atomic magnetic moments and the resulting contrasts of two simulated skyrmions at out-of-plane magnetic fields of $-1\,\mathrm{T}$ and at $-2.5\,\mathrm{T}$ are shown in Fig. 4.14 **a** and **b**. The field values (and skyrmion sizes) were chosen in order to facilitate the comparison to the measurements in Fig. 4.6 **c** and **e**. The simulated STM images were calculated using simple models for each effect: the TAMR was chosen to reduce the signal for the maximal value and was modelled with $\cos^2(\angle[\vec{m}, \vec{e}_z])$ with $\vec{m}$ as the local magnetic moment and $\vec{e}_z$ as the unit vector along the $+z$ direction. The TMR effect was implemented using Eq. 2.14 with an out-of-plane magnetized tip in $+z$ direction leading to a reduced contrast for the skyrmion center. The NCMR contrast was employed by calculating the mean angles of the six nearest neighbors according to Eq. 4.7. The NCMR was chosen to reduce the intensity in case of a large NCMR value in accordance with the experimental observation in $\mathrm{d}I/\mathrm{d}U$ maps at $+700\,\mathrm{mV}$. The contrast levels of all effects were chosen to facilitate a qualitative comparison of the appearance of the skyrmion and not to model the realistic absolute expected and measured intensities. As a result, the simulated TMR contrast (Fig. 4.14 **c** and **d**) leads to depressions for both field values whereas the simulated TAMR contrast (**e** and **f**) always shows a ring. Only the NCMR contrast in Fig. 4.14 **g** and **h** can qualitatively reproduce

the field dependent appearance of the skyrmion at a low magnetic field (ring at −1 T) and a high magnetic field (depression at −2.5 T) as it is shown in the experimental data (**i** and **j**).

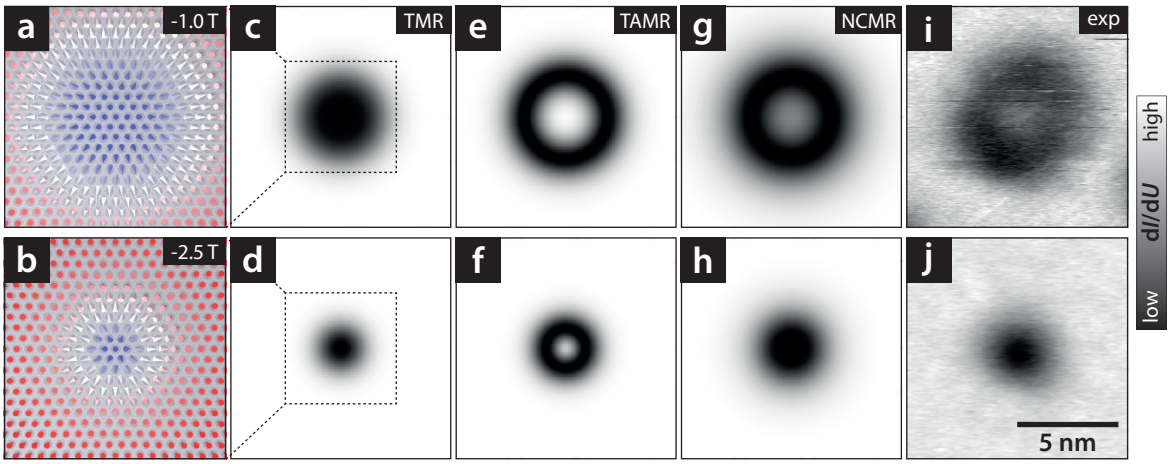

Figure 4.14.: Simulation of STM images of TMR, TAMR and NCMR for two differently sized skyrmions. **a** and **b**, Schematic of two skyrmions at −1 T (upper row) and −2.5 T (lower row) showing the atomic magnetic moments. **c** and **d**, Simulated TMR contrast. **e** and **f**, Simulated TAMR contrast. **g** and **h**, Simulated NCMR contrast. **i** and **j**, Experimental data on hcp-PdFe, color range individually adjusted (data from Fig. 4.6). For further details, see text. The simulation was done by A. Kubetzka.

The observed NCMR contrast of skyrmions in $\mathrm{d}I/\mathrm{d}U$ maps as, e.g. in Fig. 4.14 **i** and **j** is an indirect consequence of the peak shift. The $\mathrm{d}I/\mathrm{d}U$ maps in this work were recorded at a fixed sample bias of +700 mV; this spatially dependent intensity change $\Delta I_{+700\,\mathrm{mV}}(x, B)$ can be explained by the three spectra of the FM, at the skyrmion center and at the position of the maximal anisotropic non-collinearity as shown in Fig. 4.15. The dashed lines in Fig. 4.15 mark the sample bias at which the $\mathrm{d}I/\mathrm{d}U$ maps in this work were typically recorded. At a low magnetic field of −1 T in Fig. 4.15 **a**, the spectrum at the position of the maximal anisotropic non-collinearity (green, spatially separated from the skyrmion center) shows the lowest intensity at the sample bias of the $\mathrm{d}I/\mathrm{d}U$ map. At a high magnetic field of −2.5 T in Fig. 4.15 **b**, the spectrum at the skyrmion center (red) shows the lowest intensity.

4.4. Why is it difficult to distinguish between NCMR and TAMR?

Three main conditions facilitated the discovery of the NCMR effect in the vacuum LDOS of skyrmions in PdFe/Ir(111):

1. The sample system exhibits a band structure and an LDOS for spin-up and spin-down channels in the energy range of interest which leads to a large effect in the NCMR-affected vacuum LDOS (cf. Fig. 4.9 **a**).

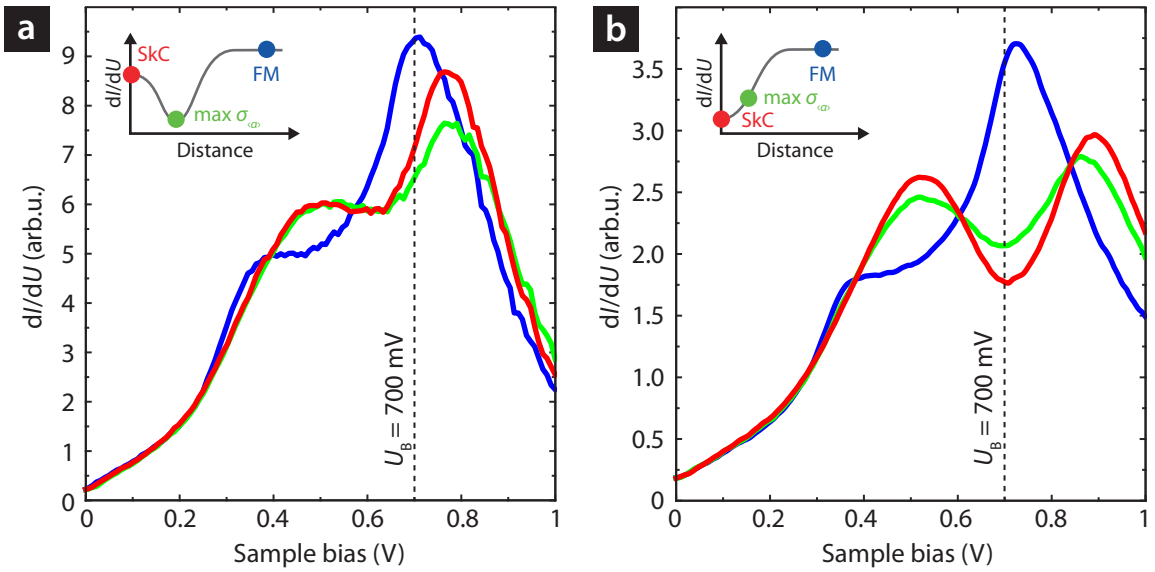

Figure 4.15.: Comparison of single spectra on the FM, at the skyrmion center and at the position of the maximal anisotropy of the non-collinearity on hcp-PdFe. **a**, Spectra on the FM, at the skyrmion center (SkC) and the position of maximal anisotropy of the non-collinearity (off the center); all measured at −1 T. The inset shows a schematic line section in a hypothetical $\mathrm{d}I/\mathrm{d}U$ map at +700 mV. **b**, Same as **a**, but at −2.5 T. The spectra in **a** are the same as in Fig. 4.12 **a**, the spectra in **b** are the same as in Fig. 4.3 **c**.

2. The magnetic skyrmion exhibits TAMR-equivalent sites in different magnetic environments (collinear ferromagnet and anti-parallel non-collinear skyrmion center).

3. The size of the skyrmion and therefore the non-collinearity of one TAMR-equivalent position on the skyrmion (center) can be tuned by the external magnetic field independently from the other TAMR-equivalent positions.

Could a STS study on the spin spiral also have led to the discovery of NCMR? The spin spiral was measured on the same sample system of PdFe/Ir(111), condition one is therefore fulfilled. The spin spiral also satisfies the second condition, e.g. by a comparison of the spectra measured at a maximum (low non-collinearity) and a minimum (high non-collinearity) on the spin spiral at +700 mV in $\mathrm{d}I/\mathrm{d}U$ maps. However, the angles and therefore the NCMR-related effect on the vacuum LDOS is low and of a similar magnitude as typically observed TAMR related changes of the LDOS [60]. Furthermore, the spin spiral in PdFe/Ir(111) does not fulfill the third condition. In case of the spin spiral on hcp-PdFe, the maxima of TAMR and NCMR are expected to be at the same positions and scale similarly with the external magnetic field as shown in Fig. 4.16 **a**. The spin spiral was modelled by the sum of two 180° domain walls according to [131] and [130] on pages 45-50:

Table 4.1.: Comparison and summary of main properties of TMR, TAMR and NCMR. [26, 27, 60, 75, 119, 128–130]

	TMR	**TAMR**	**NCMR**
range	on-site effect	on-site effect	effect of the local environment
physical origin	tunneling into different spin channels	spin-orbit coupling	hybridization between majority and minority spin channels due to non-collinear spins in the environment
scaling	$I_{\mathrm{TMR}} \propto cos(\angle[\vec{m}_{\mathrm{tip}}, \vec{m}_{\mathrm{surf}}])$	$I_{\mathrm{TAMR}} \propto cos^2(\angle[\vec{m}_{\mathrm{local}}, \vec{e}_z])$	$I_{\mathrm{NCMR}} \propto \frac{1}{6}\sum_{j=1}^{6}(\angle[\vec{m}_i, \vec{m}_j])$
contrast	contrast between $\uparrow\uparrow$ and $\uparrow\downarrow$ alignment of tip and sample magnetization	contrast between in-plane and out-of-plane alignment of surface magnetization	contrast shows differences in the local non-collinearity of the spins
electrode	spin-polarized	non-magnetic	non-magnetic
LDOS change (STS signal change; = low/high value)	∼40 % to 50 %	∼5 % to 10 %	∼50 %

$$\theta_{360^\circ}(x, c, w) = \arcsin\left(\tanh\left(\frac{-x-c}{w/2}\right)\right) + \arcsin\left(\tanh\left(\frac{-x+c}{w/2}\right)\right) \tag{4.9}$$

with the wall position c and the wall width w according to [131]

$$\begin{aligned} c &= \frac{w}{2} \cdot \operatorname{arcsinh}\left(\sqrt{\frac{2K_{\mathrm{eff}}}{M_{\mathrm{s}}B}}\right) \\ w &= 2\sqrt{\frac{A}{K_{\mathrm{eff}} + M_{\mathrm{s}}B/2}} \end{aligned} \tag{4.10}$$

with $A = 2.0 \times 10^{-12}\,\mathrm{J\,m^{-1}}$ as the exchange stiffness, $K_{\mathrm{eff}} = 2.5 \times 10^{6}\,\mathrm{J\,m^{-3}}$ as the effective anisotropy constant and $M_{\mathrm{s}} = 1.1 \times 10^{6}\,\mathrm{A\,m^{-1}}$ as the saturation magnetization [14]. The calculated maxima of TAMR and NCMR in Fig. 4.16 **a** are found nearly at the same position over the whole field range between 0.1 T to 1.0 T in which the spin spiral potentially exists. Considering the STM inherent signal broadening, it is not possible to distinguish between the different contrasts of the spin spiral. This is different for the skyrmion as shown in Fig. 4.16 **b**. At low magnetic field values of −1 T, both calculated maxima of NCMR and TAMR are found at nearly the same positions relative to the skyrmion

center. Increasing the magnetic field results in a spatial separation of the maxima of the two effects.

To summarize, the discovery of NCMR was possible due to the unique characteristics of isolated magnetic skyrmions in combination with the specific LDOS of hcp-PdFe. These properties allow a separation of the TAMR and the NCMR effect. In addition, the large observed NCMR-related effect on the vacuum LDOS of the skyrmion on hcp-PdFe rejects the TAMR effect as the physical origin of the change. Typical changes of the vacuum LDOS due to TAMR are found in the range of a few percent [27, 60]. The spin spiral on PdFe/Ir(111) show the same properties as the skyrmion, but the NCMR-related change in the vacuum LDOS of the spin spiral was not large enough to discriminate the observed change clearly from a possible TAMR contribution. However, a spin spiral in a different sample system also could have led to the discovery of NCMR.

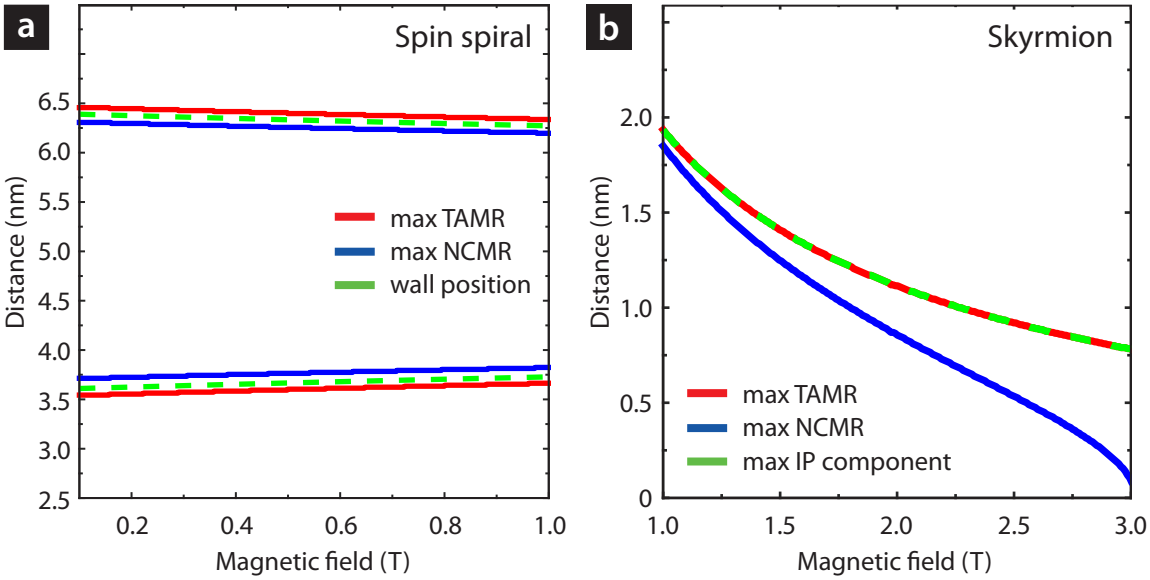

Figure 4.16.: Calculated positions of the maxima of the NCMR, the TAMR and the in-plane component, calculated for the two 180° **domain walls and the skyrmion.** **a**, Positions of the maxima of NCMR, TAMR and the wall positions of the two 180° domain walls. **b**, Same as **a** but for the skyrmion and the maximal in-plane component instead of the wall positions. The position of the different effects were calculated using Eq. 4.1, Eq. 4.7, Eq. 4.9 and Eq. 4.10.

4.5. Summary and outlook

The magnetic non-collinear environment leads to a local change of the spin-averaged (vacuum) LDOS and is measured by a resistance change. Hence, this effect is called non-collinear magnetoresistance (NCMR). The NCMR is a result of the hybridization between different spin channels and can be described within a simple phenomenological

model by the mean angle of the six nearest neighboring moments relative to a central moment. The effect was discovered in scanning tunneling spectroscopy measurements on 2D magnetic skyrmions in hcp-PdFe/Ir(111). Also, the 1D spin spiral on PdFe/Ir(111) shows the effect, but with less pronounced features due to the lower change of the non-collinearity which is in good agreement with the proposed model. In general, this effect should be present in all non-collinear magnetic systems which show local differences in their non-collinearity. However, the detailed characteristics strongly depend on the sample system.

The discovery of the NCMR effect might improve the understanding of the resistance change in transport measurements through magnetic domain walls as reported, e.g. in [62–65]. Although vacuum tunneling is fundamentally different, the observed vacuum LDOS change results from an LDOS change at the atom positions. This modified LDOS within the bulk should in turn have an effect on transport measurements through non-collinear magnetic domain walls.

The NCMR effect can be quite large as shown in Fig. 4.3 **c**. The relative intensity change $\Delta I^{\mathrm{pt}}_{+700\,\mathrm{mV}}(\vec{r}, B)$ at a point $\vec{r}$ is calculated by

$$\Delta I^{\mathrm{pt}}_{+700\,\mathrm{mV}}(\vec{r}, B) = \frac{I^{\mathrm{FM}}_{+700\,\mathrm{mV}}(\vec{r}, B) - I^{\mathrm{SkC}}_{+700\,\mathrm{mV}}(\vec{r}, B)}{I^{\mathrm{FM}}_{+700\,\mathrm{mV}}(\vec{r}, B)} \tag{4.11}$$

with $I^{\mathrm{x}}_{+700\,\mathrm{mV}}(\vec{r}, B)$ as the intensity of the ferromagnet ($x = \mathrm{FM}$) or the skyrmion center ($x = \mathrm{SkC}$) at point $\vec{r}$ and a sample bias of $U_{\mathrm{B}} = +700\,\mathrm{mV}$. For hcp-PdFe, the relative intensity change between the FM and the skyrmion center is $\sim$50 % ($B_{\mathrm{ext}} = -2.5\,\mathrm{T}$, $U_{\mathrm{B}} = +700\,\mathrm{mV}$). This change in the vacuum LDOS is much larger compared to the typically observed relative changes of TAMR ($\sim$5 % to 10 %, cf. [27, 60]), and is similar compared to the observed values of TMR (up to $\sim$40 % to 50 %, cf. e.g. [75, 119, 128–130]).

In the context of (tunnel) spintronic devices, the *areal* intensity change $\Delta I^{\mathrm{A}}_{+700\,\mathrm{mV}}(A, B)$ is more relevant. To calculate this value, the intensities of the FM and the skyrmion are integrated over the area A and their relative difference is calculated as in Eq. 4.11. For an area of $A = 7 \times 7\,\mathrm{nm}^2$, the relative areal intensity change $\Delta I^{\mathrm{A}}_{+700\,\mathrm{mV}}(A, B)$ results to $\sim$15 % at $B_{\mathrm{ext}} = +2.3\,\mathrm{T}$[11]. Lower magnetic fields lead to even higher values for $\Delta I^{\mathrm{A}}_{+700\,\mathrm{mV}}(A, B)$ since $\Delta I^{\mathrm{A}}_{+700\,\mathrm{mV}}(A, B)$ shows a stronger dependency on the number of contributing magnetic moments (larger for low fields) than on the value of the angles (larger for high fields) within the same area A. Due to this large change of the differential conductance (measured by *non*-magnetic electrodes!), the NCMR effect might be highly interesting for an application in future data storage devices like, e.g. racetrack-type devices [42].

[11] This value was experimentally obtained by calculating the ratio of the areal average value of a $\mathrm{d}I/\mathrm{d}U$ map with a skyrmion present and absent.

5. Interaction of skyrmions with native defects, adatoms or clusters in and on PdFe/Ir(111)

For a technical application of skyrmions, e.g. as information carriers, their maximal achievable degree of control needs to be demonstrated. Examples of desired properties are:

Controlled creation and annihilation of skyrmions. Fundamental requirement for using magnetic skyrmions as bit of information.

Control over the position of a skyrmion. Requirement for the realization of data storage devices, e.g. in a racetrack-type setup.

Distortion of skyrmions. Needed in order to increase the skyrmion-to-background signal ratio for a readout in a planar tunnel junction in case the junction is much larger compared to the size of the skyrmion.

Movement of skyrmions. Needed for a potential transport of a skyrmion to a readout position.

The experimental demonstration of these features by a pinning of skyrmions to immobile defects (native defects within the surface) and mobile clusters (adatoms or clusters on top of the surface) is shown in the following chapter in a proof-of-principle type study.

5.1. Creation and annihilation of single skyrmions

To demonstrate the controlled local creation and annihilation of skyrmions, an island with four defects, which are located within the surface layer, was used in this experiment[1] and is shown in Fig. 5.1. The nature of the defects is unknown, e.g. the defects might be Fe atoms which diffused from the Fe layer into the Pd layer. The result of the consecutive writing

[1]The measurement described in this section was published in N. Romming, C. Hanneken, M. Menzel *et al.*, [9] and was performed by me within the framework of this thesis.

and deleting of single skyrmions is demonstrated in Fig. 5.1 as a sequence of difference constant-current images (**c** to **j**). The difference images are used in order to focus on the magnetism. The constant-current image in **f'** shows four pinning sites without magnetic skyrmions attached to them. In order to remove the electronic contrast of the pinning defects in the measurement series, Fig. 5.1 **f'** was subtracted from each image of the image series. The resulting images in Fig. 5.1 **c** to **g** show the remaining magnetic signal. The tip magnetization had a strong in-plane and and a small out-of-plane component, the used color range accounts for the tilted tip magnetization in this measurement: a white color in Fig. 5.1 **c** to **g** corresponds to a sole out-of-plane component (no in-plane component), a full blue/red color to a sole in-plane component of the magnetization (no out-of-plane component).

The measurement was conducted as follows: the external magnetic field was set to $B_{\mathrm{ext}} = +3.25\,\mathrm{T}$ at which the two magnetic states of skyrmion and ferromagnet have approximately the same probability in the vicinity of the defects. A mostly in-plane magnetized spin-polarized Cr bulk tip[2] was used for the creation and annihilation procedure: the tip was positioned in the vicinity of a defect, the feedback loop was opened at 1 nA and the voltage was slowly increased from the scanning bias of $U_{\mathrm{B}} = +250\,\mathrm{mV}$ up to $U_{\mathrm{B}} = +850\,\mathrm{mV}$ while recording the current and the $\mathrm{d}I/\mathrm{d}U$ signal. A switching event leads to a jump in the recorded $\mathrm{d}I/\mathrm{d}U$ signal which typically occured above $\sim$500 mV. In this case, the voltage sweep was stopped and the former scanning parameters were restored after closing the feedback loop. A subsequently taken constant-current image verifies the change of the magnetic state. Due to the strong pinning to the defects, skyrmions can independently be created and destroyed in close vicinity to each other ($\sim$5 nm) which is demonstrated by a different order in the annihilation and creation sequence (cf. Fig. 5.1 **b** to **f** and **g** to **j**).

In contrast to skyrmions in the lattice phase, isolated skyrmions are only observed by STM if they are pinned, e.g. to a native defect. From the results in Fig. 5.1 it can be concluded, that the native defects lead to a modification of the potential landscape. This modification can be illustrated in a simple two-level model in Fig. 5.2: the high magnetic field of +3.25 T favors the FM state over the skyrmion state (**a**). This preference changes in the vicinity of the native defects (Fig. 5.2 **b**): the skyrmion and the ferromagnetic state are equally likely for the chosen field value of +3.25 T. The energy barrier which separates the two states can be overcome by injecting high energy electrons into the system. By this energy injection, the island can be locally transformed from the FM to the skyrmion state and vice versa. However, the detailed switching mechanism is unknown but shows a strong dependence on the applied sample bias with a small contribution by the spin transfer torque [9]. An NCMR-related contribution to the switching mechanism due to the locally changed LDOS can also not be excluded. In any case, the data demonstrates an independent switching of individual skyrmions.

[2]The strong in-plane component of the tip leads to the observed asymmetric dark-bright contrast of the skyrmion although its spin structure is centro-symmetric. One should keep in mind that at $B_{\mathrm{ext}} = +3.25\,\mathrm{T}$ (out-of-plane) only an antiferromagnetic tip like the used Cr tip is able to maintain an in-plane magnetization. The tip did not change during the measurement.

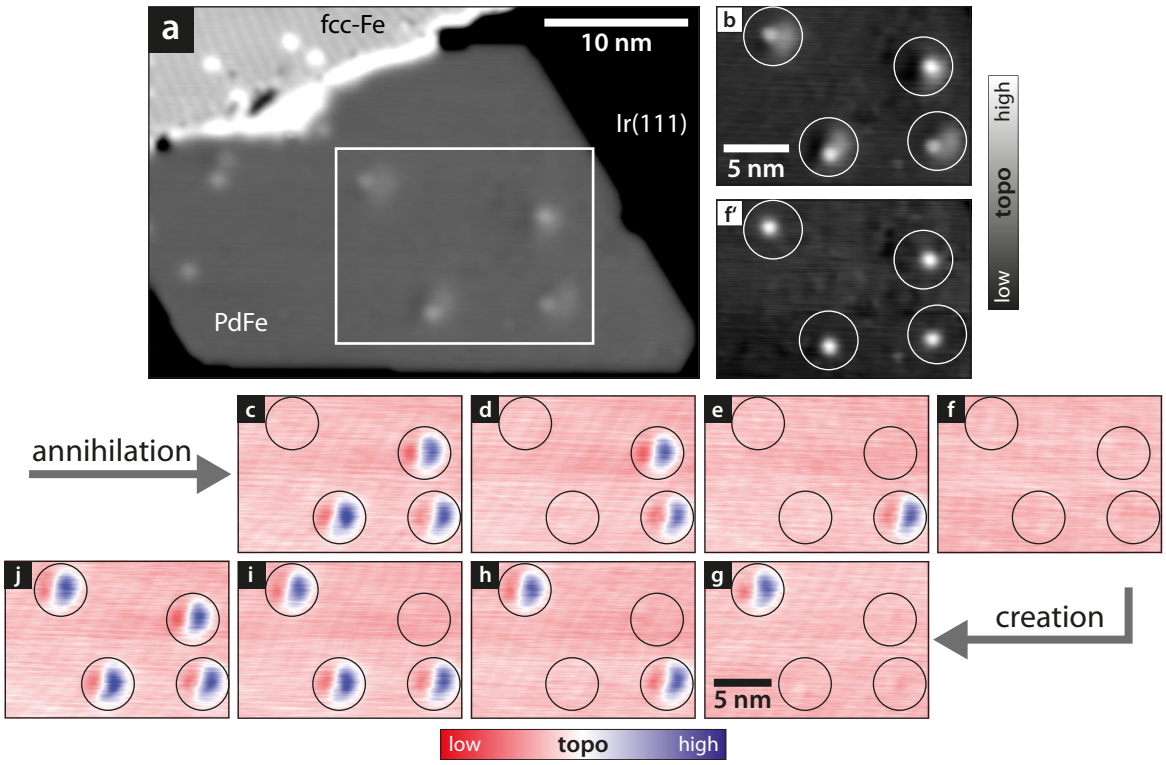

Figure 5.1.: Experimental demonstration of the controlled creation and annihilation of isolated skyrmions which are pinned to in-layer defects. **a**, Overview constant-current image of a PdFe island showing four pinning defects (white box). **b** and **f'**, Enlarged constant-current images of the four pinning defects of **a** with four skyrmions (**a**) and without skyrmions (**f'**). **b** to **j**, Result of subsequent skyrmion annihilation (**b** to **f**) and creation (**g** to **j**) processes. The images in **c** to **j** are difference constant-current images with the image in **f'** subtracted from each image. The circles indicate the positions of the skyrmions. The measurement parameters were $I_T = 1\,\mathrm{nA}$, $U_B = +250\,\mathrm{mV}$, $B_{ext} = +3.25\,\mathrm{T}$, and $T = 4.2\,\mathrm{K}$. The measurement was done with an in-plane spin-polarized Cr bulk tip. **b** to **j** and **f'** were published in [9].

5.2. Pinning of skyrmions: in-layer defects versus single Co adatoms

Figure 5.3 **a** and **b** show constant-current images of different PdFe islands before and after the deposition of single Co atoms; **c** and **d** show constant-current images of the enlarged fcc-PdFe and hcp-PdFe island before the Co atom deposition, the contrast is adjusted in order to highlight the native in-layer defects (blue circles). The $\mathrm{d}I/\mathrm{d}U$ maps in Fig. 5.3 **e** and **g** show the fcc-PdFe island, the $\mathrm{d}I/\mathrm{d}U$ maps in **f** and **h** show the hcp-PdFe island before and after the deposition. All skyrmions in the $\mathrm{d}I/\mathrm{d}U$ maps in Fig. 5.3 **e** to **h** show a dominant NCMR contrast. The external magnetic field was not changed during the deposition of the

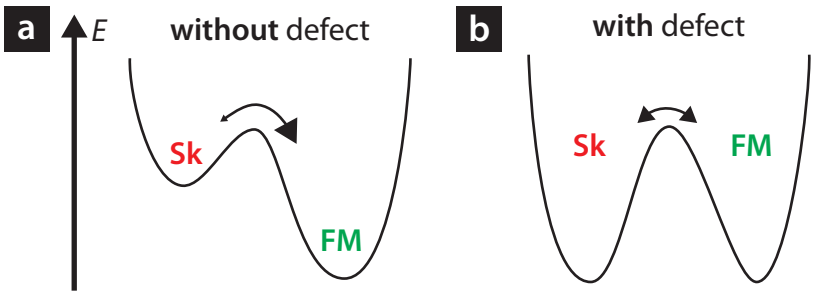

Figure 5.2.: Schematic of a two-level model which illustrates the change of the potential landscape in the close vicinity of an (in-layer) defect. **a**, Energetic levels for a magnetic field value which favors the ferromagnetic state over the skyrmion state. **b**, Energetic levels in the vicinity of a pinning defect at the same magnetic field as in **a**. At the magnetic field value of +3.25 T, the ferromagnetic state and the skyrmion state are equally favored.

single Co atoms.

Both the fcc-PdFe and hcp-PdFe islands in Fig. 5.3 **c** and **d** show native defects within the surface layer (blue circles). These native defects act as pinning sites for skyrmions as can be seen in the corresponding $\mathrm{d}I/\mathrm{d}U$ maps in Fig. 5.3 **e** and **f**: skyrmions are found in the close vicinity of the corresponding positions of all defects. The only exception of the pinning of skyrmions at a native defect site is found for the fcc-PdFe island in Fig. 5.3 **e** (red circle): the corresponding position of the marked skyrmion in **e** does not show an in-layer defect in the constant-current image in **c**. The observation of single skyrmions in the vicinity of nearly each defect indicates a strong interaction between the skrymions and the in-layer defects.

In order to qualitatively compare the interaction strength between skyrmions and native in-layer defects with the interaction strength between skyrmions and adatoms on top of the PdFe island, single Co atoms were deposited and the same islands as in Fig. 5.3 **e** and **f** were imaged again. The result is shown in the $\mathrm{d}I/\mathrm{d}U$ maps in Fig. 5.3 **g** and **h**. The deposited Co atoms do not change the magnetic states of both fcc-PdFe and hcp-PdFe islands except at two positions: the marked skyrmion in Fig. 5.3 **e** (red circle), which did not exhibit a corresponding native defect in the constant-current map in **c**, disappeared after a single atom was deposited in its vicinity (**g**). In contrast, the hcp-PdFe island shows a new skyrmion in Fig. 5.3 **h** which is pinned to a Co adatom although the marked position (red circle) does not show a corresponding in-layer defect in the constant-current map in Fig. 5.3 **d**.

Interestingly, although several single Co atoms are found on the fcc-PdFe and hcp-PdFe islands after the deposition, the overal magnetic state is not affected (except for the two above described cases). The specific sample bias of +700 mV in this experiment was chosen for two reasons: besides the typically observed NCMR contrast at this sample bias, the provided energy should be sufficient for the formation of new skyrmions in the vicinity of the Co atoms. This idea is based on the strong bias-dependence of the switching probability between the ferromagnetic and the skyrmion state as described in [9]. However, the formation

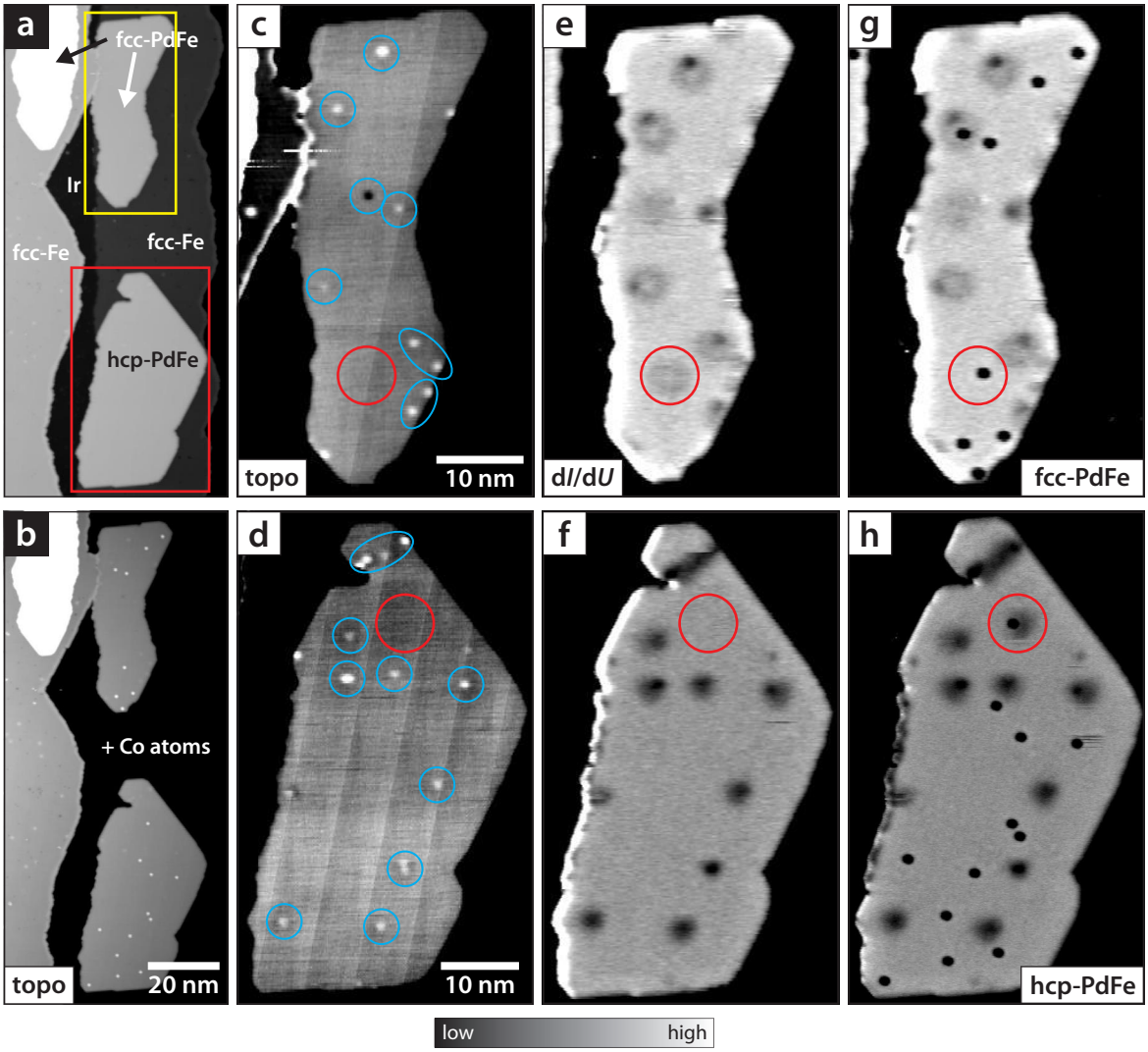

Figure 5.3.: Skyrmions pinned to in-layer defects before and after the deposition of single Co atoms. **a** and **b**, Constant-current images showing an overview of three PdFe islands before and after the deposition of single Co atoms, respectively. **c** and **d**, Constant-current images of two enlarged fcc-PdFe and hcp-PdFe islands in **a** before the deposition of single Co atoms. The contrast is adjusted to highlight the in-layer defects (blue circles), the parallel straight lines are a result of the digital signal from the Specs Nanonis SPM controller [121] which controls the tip height. **e** and **f**, $\mathrm{d}I/\mathrm{d}U$ maps of the two PdFe islands in **c** and **d** before the Co atom deposition. **g** and **h**, Same as **e** and **f**, but after the deposition. The skyrmions in all $\mathrm{d}I/\mathrm{d}U$ maps show a dominant NCMR contrast. The measurement parameters were $I_\mathrm{T} = 1\,\mathrm{nA}$, $U_\mathrm{B} = +700\,\mathrm{mV}$, $U_\mathrm{mod} = 40\,\mathrm{mV}$, $B_\mathrm{ext} = +1.8\,\mathrm{T}$, and $T = 8\,\mathrm{K}$. The measurement was done with a Cr bulk tip.

of new skyrmions is only observed in one case on the hcp-PdFe island (cf. Fig. 5.3 **f** and **h**). The interaction strength between skyrmions and single Co atoms on top of the surface is therefore much lower compared to the interaction between skyrmions and defects within the layer.

The reason for the weaker coupling between skyrmions and adatoms might be due to the different separation distances between the adatoms and in-layer defects, and the Fe layer beneath. The magnetism originates mainly from the Fe layer on top of Ir(111) [12]. Native defects are closer to the Fe layer and can directly couple to the Fe atoms, whereas the Co adatoms on top of the surface only indirectly couple to the Fe layer via the Pd layer. The strength of this indirect coupling is presumably lower compared to the direct coupling of the in-layer defects. This leads to the observed weak interaction for single Co atoms and skyrmions compared to the strong coupling between in-layer defects and skyrmions.

To summarize, skyrmions are strongly pinned to defects within the Pd layer for both fcc-PdFe and hcp-PdFe. The overall magnetic state did not change after the deposition of single Co atoms, except for two cases. The interaction between skyrmions and single Co adatoms is therefore weak compared to the interaction between skyrmions and in-layer defects.

5.3. Skyrmion distortion due to the interaction with in-layer defects and surface clusters

Each skyrmion in Fig. 5.3 **e** and **f** is pinned to a single defect (except one). If the skyrmion is pinned to more than one pinning site, the shape of the skyrmion is modified as shown in Fig. 5.4: **a** and **b** show constant-current images, **c** and **d** the corresponding $\mathrm{d}I/\mathrm{d}U$ maps of the skyrmions. Figure 5.4 **e** and **f** show unperturbed axisymmetric reference skyrmions. The top and the bottom row of Fig. 5.4 were measured with two different microtips on two different islands. The sample bias was chosen so that the skyrmions exhibit a dominant NCMR contrast in the measured $\mathrm{d}I/\mathrm{d}U$ maps. The external magnetic field values were chosen in the way that the electron energy does not destabilize the skyrmions in the experiments in Fig. 5.4 (and Fig. 5.5).

Figure 5.4 **c** shows a skyrmion which exhibits two in-layer defects (circles) in its region of maximal NCMR contrast. The two-fold pinned skyrmion in Fig. 5.4 **c** is elongated along one direction compared to the axisymmetric reference skyrmion in **e**. Interestingly, the same distortion effect is found for Co clusters[3] on top of the surface in Fig. 5.4 **d**: the skyrmion exhibits three Co clusters at its region of maximal NCMR contrast and is severely stretched

[3]The number of atoms within the cluster is unknown due to partial cluster formation during or after the deposition process.

in one direction compared to the reference skyrmion in **f**. This strong interaction between the Co *clusters* and the skyrmion is in contrast to the weak interaction between the Co *adatoms* and the skyrmions in Fig. 5.3 **g** and **h**. Apparently, the coupling strength between the skyrmion and the Co cluster on top of the surface depends on the number of (magnetic) constituents within the cluster.

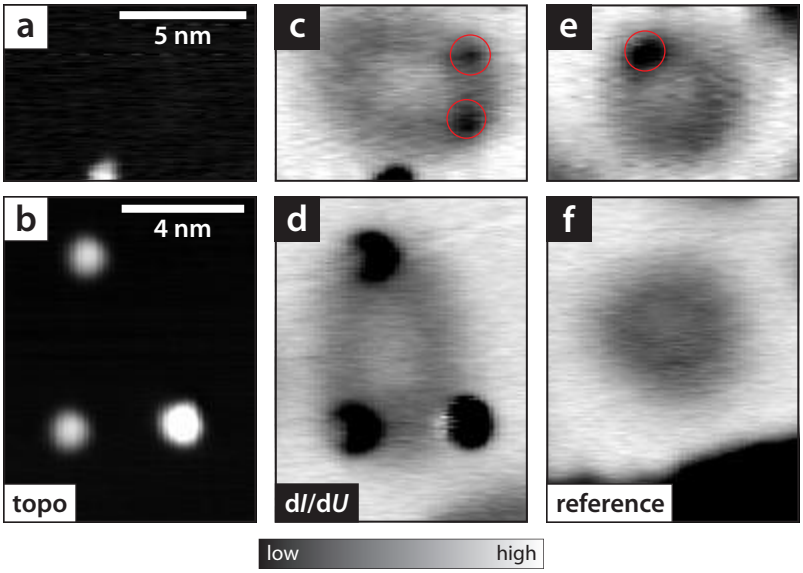

Figure 5.4.: Distortion of the skyrmion shape by defects and surface clusters. **a** and **b**, Constant-current images showing the positions of Co clusters on top of the surface (white spots). **c** and **d**, $\mathrm{d}I/\mathrm{d}U$ maps showing the pinned and distorted skyrmions. The red circles mark in-layer defects. **e** and **f**, $\mathrm{d}I/\mathrm{d}U$ maps showing axisymmetric reference skyrmions. The top and the bottom row were measured with two different microtips on two different PdFe islands. All skyrmions show an NCMR contrast. The measurement parameters were $I_\mathrm{T} = 1\,\mathrm{nA}$, $U_\mathrm{B} = +700\,\mathrm{mV}$, $U_\mathrm{mod} = 40\,\mathrm{mV}$, $B_\mathrm{ext} = +1.2\,\mathrm{T}$ (top row) and $B_\mathrm{ext} \approx +1.0\,\mathrm{T}$ (bottom row). All measurements were done at $T = 4.2\,\mathrm{K}$ using a Cr bulk tip, but different microtips for the top and the bottom row.

The strong coupling between the skyrmion and the Co clusters on top of the surface can be exploited for the controlled distortion of the skyrmion shape. This was done in Fig. 5.5: constant-current images (top row) and corresponding $\mathrm{d}I/\mathrm{d}U$ maps (middle row) show the same skyrmion with differently positioned Co clusters on top. The bottom row shows $\mathrm{d}I/\mathrm{d}U$ maps of single-pinned axisymmetric skyrmions (reference skyrmion) measured on the same island with the same microtip as in the corresponding images in the rows above. In all $\mathrm{d}I/\mathrm{d}U$ maps, the skyrmions show a dominant NCMR contrast. Between Fig. 5.5 **d** and **f**, different clusters were moved by the STM tip[4]. Depending on the positions of the clusters relative to

[4]The tip has changed several times during the measurement. However, these changes seem to be of minor

the skyrmion, the skyrmion in Fig. 5.5 **d** to **f** shows a changing appearance compared to the reference skyrmion (**h** to **j**): the skyrmion is either enlarged and shows a white spot at its center (**d**), has a small diameter without a white center (**e**) or is distorted from its circular shape (**f**). Although this measurement was done at a constant field value, the skyrmion changes its appearance from a ring-like shape (Fig. 5.5 **d**) to a depression (**e**) due to the re-arrangement of the clusters on top of the surface. The skyrmions in Fig. 5.5 **d** and **e** resemble skyrmions which were measured at different magnetic field values as in Fig. 4.6 **c** and **d**. The comparison of the changed appearance of the multiple-pinned skyrmion and the nearly unchanged appearance of the reference skyrmion indicate that the appearance change is due to the repositioning of the clusters and not due to tip changes.

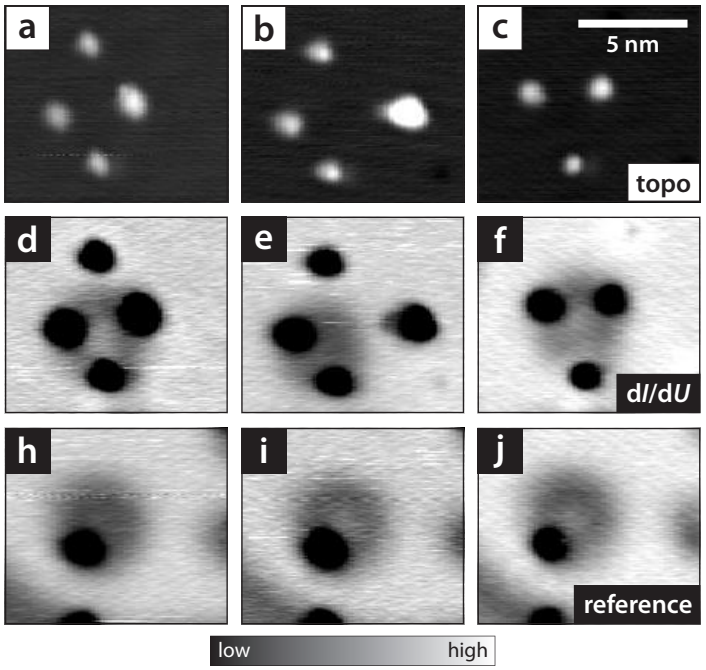

Figure 5.5.: Distortion of the skyrmion shape by differently positioned clusters. Top row, a to c, Constant-current images showing the positions of the clusters (white spots). **Middle row, d to f**, $\mathrm{d}I/\mathrm{d}U$ maps showing the distorted skyrmions and their pinning to the clusters (black spots). **Bottom row, h to j**, $\mathrm{d}I/\mathrm{d}U$ maps showing a single pinned reference skyrmion for comparison with the strongly pinned skyrmion. All skyrmions show a dominant NCMR contrast. The measurement parameters were $I_\mathrm{T} = 1\,\mathrm{nA}$, $U_\mathrm{B} = +700\,\mathrm{mV}$, $U_\mathrm{mod} = 40\,\mathrm{mV}$, $I_\mathrm{manip} = 35\,\mathrm{nA}$ to $75\,\mathrm{nA}$, $U_\mathrm{manip} = +1\,\mathrm{mV}$ to $+6\,\mathrm{mV}$, $B_\mathrm{ext} = +2.0\,\mathrm{T}$, and $T = 4.2\,\mathrm{K}$. The measurement was done with a Cr bulk tip.

importance in this experiment as can be seen from a comparison of the reference skyrmions in Fig. 5.5 **h** to **j**: the imaged shapes of the clusters remained nearly the same, the observed contrast only slightly changed.

To summarize, Co clusters show a significant coupling to the skyrmion in contrast to the weak coupling of single Co atoms in Fig. 5.3 **g** and **h**. The shape of the skyrmion can be manipulated using different positions of Co clusters relative to the skyrmion. By this re-arrangement of the cluster positions on the skyrmion, the effect of an external magnetic field can be mimicked or the skyrmion can be stretched along one direction.

5.4. Skyrmion movement by pinning to a cluster

The previous section demonstrates the pinning of skyrmions to Co clusters on top of the surface. This pinning can be exploited for the lateral movement of a single skyrmion. An empty area with few Co clusters on top was chosen for this experiment as presented in Fig. 5.6: the area's topography is shown in **a**[5], the $\mathrm{d}I/\mathrm{d}U$ maps of the moved skyrmion imaged by an NCMR contrast in **b** to **e**. Both magnetic field value and sample bias were chosen in the way that the pinned skyrmion was stable and did not switch between the FM and the skyrmion state while imaging the skyrmion. During the experiment, the pinning cluster was moved by the STM tip from the bottom of the area towards the upper right corner of the area (Fig. 5.6 **b** to **e**). After each manipulation step, a skyrmion is found at the new cluster position[6]. The skyrmion was moved by more than 10 nm by the lateral movement of the cluster.

For the lateral movement of the cluster, a very low sample bias of +1 mV to +6 mV was used. This low sample bias is important since at a low sample bias the switching probability between the skyrmion and the ferromagnetic state approaches zero according to [9]. This vanishing switching probability should also be the case for this skyrmion movement experiment even though the current during the cluster movement was relatively high (35 nA to 75 nA). Hence, by using this parameter set it should be unlikely to create or destroy the pinned skyrmion during the lateral manipulation; the moved skyrmion is likely to be the same skyrmion rather than a destroyed and newly created skyrmion. The general effect of the cluster is a local lowering of the energy landscape of the PdFe island. This local potential minimum leads to the favoring of the skyrmion state over the ferromagnetic state within the vicinity of the Co cluster. While moving the Co cluster with the STM tip, the skyrmion follows this local potenial minimum. The physical origin of the attractive force between the cluster and the skyrmion is unknown. This observation and its explanation resembles atom manipulation in a way. In order to move an atom, the tip approaches the atom and establishes a chemical bond which is strong enough to move the atom by moving the STM tip as e.g. in [80, 113, 114]. This tip-atom bond is comparable to the cluster related

[5] to be precise, this is the topography of Fig. 5.6 **b**

[6] The tip has changed several times during the measurement. However, these changes seem to be of minor importance in this particular experiment. The main differences before and after the tip changes were variations of the intensity in the $\mathrm{d}I/\mathrm{d}U$ maps. The imaged shapes of, e.g. the adatoms remained nearly the same as can be seen by a comparison of Fig. 5.6 **b** to **e**.

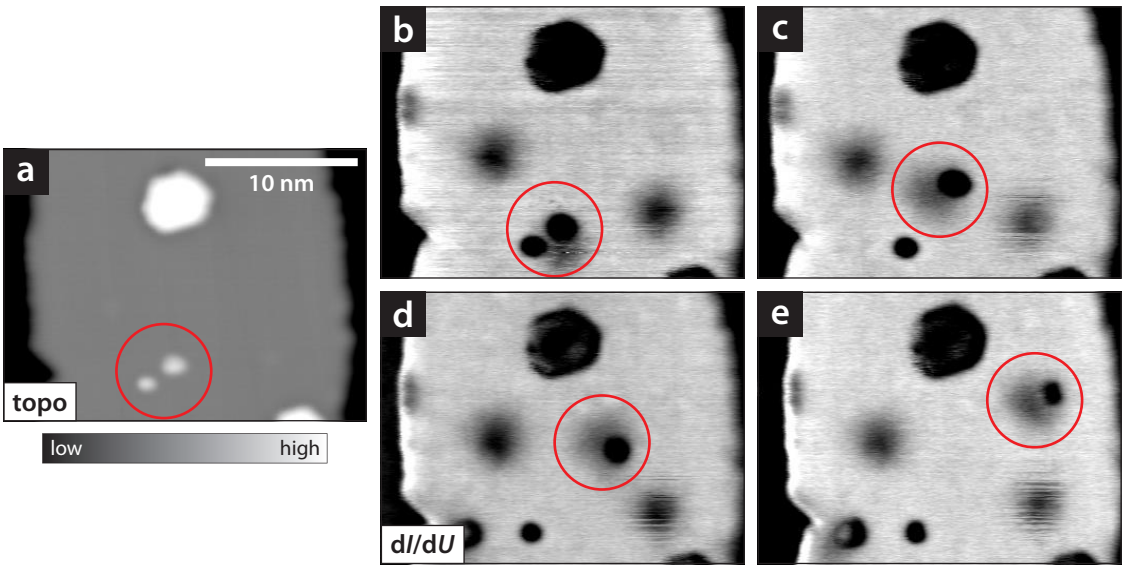

Figure 5.6.: Skyrmion movement by repositioning a surface cluster. **a**, Constant-current image of **b** showing two Co clusters in the lower part of the area (red circle). **b** to **e**, sequence of $\mathrm{d}I/\mathrm{d}U$ maps showing magnetic skyrmions (red circles, NCMR contrast) which are pinned to a Co cluster. The cluster was moved between **b** to **e** by the STM tip towards the upper right corner of the area. The measurement parameters were $I_\mathrm{T} = 1\,\mathrm{nA}$, $U_\mathrm{B} = +700\,\mathrm{mV}$, $U_\mathrm{mod} = 40\,\mathrm{mV}$, $I_\mathrm{manip} = 35\,\mathrm{nA}$ to $75\,\mathrm{nA}$, $U_\mathrm{manip} = +1\,\mathrm{mV}$ to $+6\,\mathrm{mV}$, $B_\mathrm{ext} = +2.1\,\mathrm{T}$, and $T = 8\,\mathrm{K}$. The measurement was done with a Cr bulk tip.

minimum of the energy landscape of the PdFe island. Moving the cluster, i.e. moving the energy minimum, allows the skyrmion to move while moving the Co cluster.

5.5. Summary and outlook

The controlled individual creation and annihilation of four skyrmions at in-layer defects was demonstrated. The skyrmions were created and annihilated by the local injection of a high current at a high voltage in the vicinity of four in-layer defects. Furthermore, the pinning strengths between skyrmions and in-layer defects and skyrmions and single adatoms on top of the surface were qualitatively compared. As a result, skyrmions show a strong pinning to in-layer defects, but couple only weakly to single Co adatoms. The coupling strength is different for Co clusters on top of the surface, Co clusters show a clear interaction with skyrmions. If three Co clusters are located above the skyrmion, the strong coupling can result in a distortion of the axisymmetric skyrmion shape. By moving the Co clusters using the STM tip, the skyrmion can be asymmetrically stretched along one direction, compressed or expanded. The strong coupling between the skyrmion and the Co cluster can also be used for the lateral movement of a skyrmion: moving the Co cluster to which a single skyrmion

is pinned (by using the STM tip) leads to the simultaneous lateral movement of the pinned skyrmion.

In the following, a general consideration of potential pinning mechanisms is done. The overall effect was already illustrated in Fig. 5.2: the defect within the layer or the Co adatom or cluster on top of the layer, which are called pinning centers in the following, lead to a modification of the potential landscape in the vicinity of the pinning center. As a consequence, the skyrmions align themselves relative to the pinning centers in order to minimize their total energy. The physical origin of the local potential minimization is unknown. One could think of various origins like, e.g. a coupling of the magnetic pinning centers via the exchange interaction to the Fe layer. A coupling by the exchange interaction might explain the increasing coupling strength between the skyrmions and an increasing number of magnetic atoms within the Co cluster (single adatom: weak coupling, larger clusters: stronger coupling). The exchange interaction could also explain the strong effect of in-layer defects on the skyrmions compared to the weak effect of single adatoms. The short distance to the Fe layer results to a stronger (direct) interaction compared to the larger distance between the Co adatoms and the Fe layer via the Pd spacer layer with its (indirect) weaker coupling. Another interaction which might contribute to the skyrmion pinning is a change of the local magnetocrystalline anisotropy. Furthermore, a pinning due to the local change of the electronic band structure by the NCMR effect could be possible. A good experiment which would give a first idea of the dominant pinning interaction could be done by the deposition of non-magnetic atoms like, e.g. Pd. If a pinning to these atoms or (artificially) built clusters is still observed, the exchange interaction between the non-magnetic adatoms and the Fe layer can most likely be excluded as the driving pinning mechanism.

To summarize, this proof-of-principle type study demonstrates a high degree of control over isolated skyrmions. However, a more detailed study is needed in order to investigate the mechanisms which contribute to the pinning of magnetic skyrmions.

6. Summary and outlook

In the framework of this thesis, a detailed STS study of the different magnetic states of (hcp-)PdFe/Ir(111) was performed. As a result of this experimental study, a new fundamental physical effect called non-collinear magnetoresistance (NCMR) is described for the first time. This effect causes a variation of the (spin-averaged) LDOS due to the mixing of spin channels and results from a locally non-collinear magnetic environment. The characteristic NCMR-affected LDOS of hcp-PdFe shows two peaks (skyrmion center) compared to a single FM peak. The NCMR effect can be described by a shift and a decrease of the higher energy peak which scale with an increasing degree of the local non-collinearity and the spatial anisotropy of the non-collinearity. The scaling of NCMR is different for an isotropic (all nearest neighbor angles are equal) and an anisotropic non-collinear magnetic environment (the nearest neighbor angles vary). The NCMR effect was observed for both hcp and fcc stackings of PdFe. The effect on the vacuum LDOS is lower for a 1D spin spiral and higher for a 2D skyrmion which is in agreement with the proposed simple phenomenological model of NCMR. This new magnetoresistance enables an *electrical* detection of non-collinear *magnetic* structures which is similar to TAMR, but roughly one order of magnitude larger (TAMR: ∼5 % to ∼10 %; NCMR: ∼50 %). This effect is believed to be a universal effect in non-collinear magnetic systems and should not only be restricted to a tunnel geometry. For example, the NCMR affected LDOS at the atomic sites should contribute to the observed resistance change in transport experiments through magnetic domain walls as e.g. in [62–64]. However, its specific impact on the LDOS strongly depends on the details of the sample system.

In the second part of this thesis, the interaction between magnetic skyrmions and native defects within the layer, and adatoms and clusters on top of the surface were investigated in a proof-of-principle type study. As a result, skyrmions in PdFe show a strong interaction with defects within the layer and larger clusters on top of the surface. The coupling between skyrmions and single Co adatoms is negligibly weak. By using larger Co clusters, it is possible to distort the shape of a skyrmion or even move an isolated skyrmion by moving the cluster using atom manipulation. These experiments demonstrate the high degree of control which can be obtained over magnetic skyrmions.

Future experiments should go in the direction of a technical implementation of NCMR into device-type designs. For this, physical systems which show a large NCMR-dependent signal change need to be identified. Also, it would be interesting to investigate the influence of the NCMR effect on the creation and annihilation process of isolated skyrmions. The question about the fundamental effects which lead to the pinning of skyrmions need to be answered in order to get a deeper understanding of the interplay of skyrmions and their interaction with small clusters. All proposed experimental ideas are interesting in view of a technical

application of magnetic skyrmions as well as they are of particular scientific interest. This work presents steps in both directions, if only tiny ones.

A. Appendix: Stacking identification of Pd on fcc-Fe/Ir(111)

A typical sample preparation as described in Sec. 3.3 yields two different stackings of PdFe/Ir(111), which are distinguishable by two different contrast levels in $\mathrm{d}I/\mathrm{d}U$ maps if imaged at $U_\mathrm{B} = +700$ mV in constant-current mode. The stacking of the step-flow grown Fe layer beneath the Pd layer is known to be face-centered cubic [66, 132]. This knowledge about the stacking is now used to determine the stacking of the Pd layer on top of the fcc-Fe/Ir(111). For this purpose, the Fe layer needs to be homoplanar and directly connected to a PdFe bilayer, which is the case if the PdFe is found on a lower terrace than the Fe layer. The simultaneously obtained atomic resolution on both the Fe layer and the PdFe bilayer allows to distinguish between an hcp and an fcc stacking of Pd. The resulting atomic resolution between fcc-Fe and a bright PdFe island is shown in Fig. A.1: the $\mathrm{d}I/\mathrm{d}U$ map in **a** and the current image in **b** show overview images of the region with atomic resolution in **b** and the zoomed constant-current image in **c**. Figure A.1 **d** shows a sketch of the layer stacking of Ir, fcc-Fe and PdFe, and **e** shows STS data on a skyrmion on a bright island on which the atomic resolution was obtained. As it can be seen in Fig. A.1 **c**, the pattern of the atoms on the fcc-Fe lattice is continued in the Pd layer as indicated by the yellow lines. This means that the Pd layer grows in the same fcc stacking as the Fe layer (fcc-PdFe). This argumentation assumes that the observed atomic corrugation does not show a contrast inversion. This is a reasonable assumption since the observed contrast of the atomic structure of Fe on Ir(111) is in accordance with the previously reported contrast of Fe on Ir [7]. In addition, the contrast of Fe and Pd in Fig. A.1 **c** shows a hexagonal lattice of white spots on a dark background instead of an inverted contrast. Therefore, the bright contrast in $\mathrm{d}I/\mathrm{d}U$ maps at $U_\mathrm{B} = +700\,\mathrm{mV}$ corresponds to fcc-PdFe, the dark contrast to hcp-PdFe stacking.

Knowing that fcc-PdFe islands exhibit a brighter contrast than hcp-PdFe islands in $\mathrm{d}I/\mathrm{d}U$ maps at $+700\,\mathrm{mV}$, point spectroscopy data at the skyrmion center can be used as a complementary way in addition to $\mathrm{d}I/\mathrm{d}U$ maps to discriminate between the two stackings. Figure 4.3 **c** and **d** show a huge difference in the STS at the skyrmion center between the two different Pd stackings (two peaks for hcp-PdFe versus a shifted single peak for fcc-PdFe at the same magnetic field value). An example of STS data measured on fcc-PdFe is shown in Fig. A.1 **e**: spectra were taken on both the ferromagnetic region (black) and the skyrmion center (blue and red, with a tip change between the two measurements). The observed shifted single peak at the skyrmion center on fcc-PdFe in Fig. A.1 **e** is in agreement with the STS data measured in Fig. 4.3 **d**. Therefore, spectra resembling Fig. A.1 **e** and Fig. 4.3 **d** indicate an fcc-PdFe island, spectra showing two peaks at the skyrmion center as in Fig. 4.3 **c** are measured on a hcp-PdFe island.

To summarize, PdFe islands showing a dark contrast in $\mathrm{d}I/\mathrm{d}U$ maps at +700 mV are hcp-Pd on fcc-Fe and show two peaks in the spectroscopy at the skyrmion center (at least if B_{ext} ∼1.4 T or above, cf. Sec. 4.3). Bright islands are fcc-PdFe islands and show a single shifted peak at the skyrmion center (within the investigated magnetic field range of up to ±2.5 T).

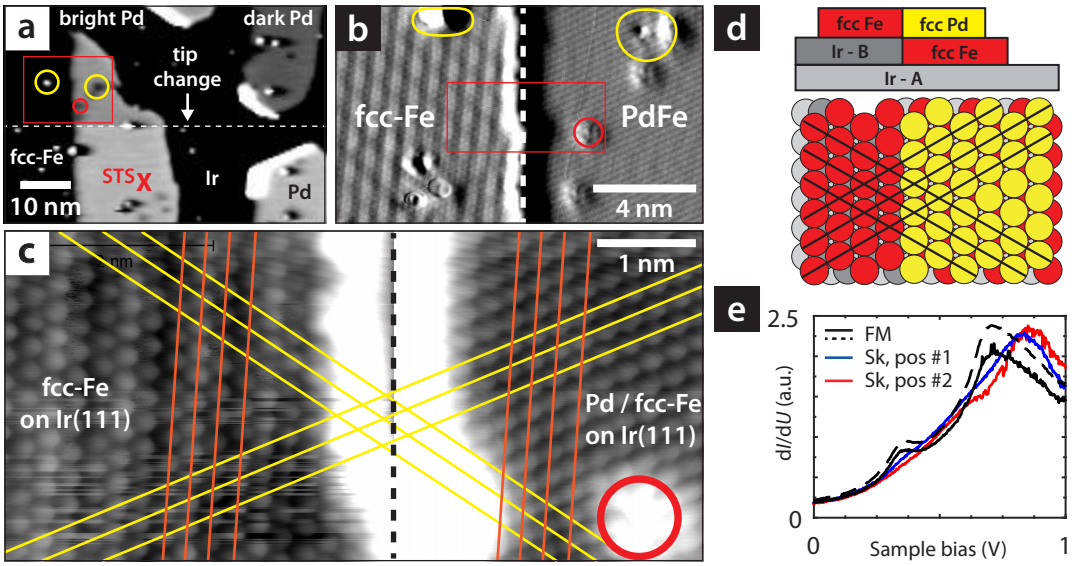

Figure A.1.: Stacking identification of Pd on the fcc-Fe layer. **a**, Overview $\mathrm{d}I/\mathrm{d}U$ map of PdFe islands of different stackings showing the position where atomic resolution was obtained (red box) and the skyrmion center STS were measured (red cross). **b** and **c**, Enlarged regions (current image (**b**) and constant-current image (**c**)) of the marked region in **a** showing an atomic corrugation on both the Fe layer and PdFe island. In order to compensate for the height difference between the two layers in **c**, the contrasts of the left (fcc-Fe) and the right half (PdFe) were adjusted separately (the cut between the images is indicated by the dashed line). The yellow and red lines in **c** are a guide to the eye; the yellow lines highlight the continuation of the atomic lattice on the Pd layer. The additional superstructure on the Fe layer in **b** is due to a contrast by spin-orbit coupling [7]. The same defects in **a**, **b** and **c** are marked with circles (red, yellow). **d**, Schematic of the layering of the sample in **c**, seen from the side. **e**, STS measured on the skyrmion center on a bright Pd island. The measurement parameters for **a** were $I_\mathrm{T} = 1\,\mathrm{nA}$, $U_\mathrm{B} = +700\,\mathrm{mV}$, $B_\mathrm{ext} = +5\,\mathrm{T}$; for **b**, $I_\mathrm{T} = 7.3\,\mathrm{nA}$, $U_\mathrm{B} = +6.4\,\mathrm{mV}$, $B_\mathrm{ext} = +5\,\mathrm{T}$; for **c**, $I_\mathrm{T} = 9.2\,\mathrm{nA}$, $U_\mathrm{B} = +2.5\,\mathrm{mV}$, $B_\mathrm{ext} = +5\,\mathrm{T}$ and for **e**, $I_\mathrm{stab} = 1\,\mathrm{nA}$, $U_\mathrm{stab} = -200\,\mathrm{mV}$, $U_\mathrm{mod} = 13\,\mathrm{mV}$, $\tau = 3\,\mathrm{ms}$, $B_\mathrm{ext} = +2.5\,\mathrm{T}$. All measurements were done at $T = 4.2\,\mathrm{K}$ using a Cr bulk tip.

Bibliography

[1] A. N. Bogdanov and D. A. Yablonsky, "Thermodynamically stable vortexes in magnetically ordered crystals - mixed state of magnetics," *Zhurnal Eksperimentalnoi I Teoreticheskoi Fiziki*, vol. 95, no. 1, pp. 178–182, 1989.

[2] A. N. Bogdanov and A. Hubert, "Thermodynamically stable magnetic vortex states in magnetic crystals," *Journal of Magnetism and Magnetic Materials*, vol. 138, no. 3, pp. 255–269, 1994.

[3] U. K. Roessler, A. A. Leonov, and A. N. Bogdanov, "Chiral skyrmionic matter in non-centrosymmetric magnets," *Journal of Physics: Conference Series*, vol. 303, no. 1, p. 012105, 2011.

[4] S. Muehlbauer, B. Binz, F. Jonietz, C. Pfleiderer, A. Rosch, A. Neubauer, R. Georgii, and P. Boeni, "Skyrmion lattice in a chiral magnet," *Science*, vol. 323, no. 5916, pp. 915–919, 2009.

[5] X. Yu, Y. Onose, N. Kanazawa, H. S. Park, J. H. Han, Y. Matsui, N. Nagaosa, and Y. Tokura, "Real-space observation of a two-dimensional skyrmion crystal," *Nature*, vol. 465, no. 7300, pp. 901–904, 2010.

[6] N. S. Kiselev, A. N. Bogdanov, R. Schaefer, and U. K. Roessler, "Comment on giant skyrmions stabilized by dipole-dipole interactions in thin ferromagnetic films," *Physical Review Letters*, vol. 107, no. 17, p. 179701, 2011.

[7] S. Heinze, K. von Bergmann, M. Menzel, J. Brede, A. Kubetzka, R. Wiesendanger, G. Bihlmayer, and S. Blügel, "Spontaneous atomic-scale magnetic skyrmion lattice in two dimensions," *Nature Physics*, vol. 7, no. 9, pp. 713–718, 2011.

[8] A. Fert, V. Cros, and J. Sampaio, "Skyrmions on the track," *Nature Nanotechnology*, vol. 8, no. 3, pp. 152–156, 2013.

[9] N. Romming, C. Hanneken, M. Menzel, J. E. Bickel, B. Wolter, K. von Bergmann, A. Kubetzka, and R. Wiesendanger, "Writing and deleting single magnetic skyrmions," *Science (New York, N.Y.)*, vol. 341, no. 6146, pp. 636–639, 2013.

[10] J. Sampaio, V. Cros, S. Rohart, A. Thiaville, and A. Fert, "Nucleation, stability and current-induced motion of isolated magnetic skyrmions in nanostructures," *Nature Nanotechnology*, vol. 8, no. 11, pp. 839–844, 2013.

[11] N. Nagaosa and Y. Tokura, "Topological properties and dynamics of magnetic skyrmions," *Nature Nanotechnology*, vol. 8, no. 12, pp. 899–911, 2013.

[12] B. Dupé, M. Hoffmann, C. Paillard, and S. Heinze, "Tailoring magnetic skyrmions in ultra-thin transition metal films," *Nature communications*, vol. 5, p. 4030, 2014.

[13] K. von Bergmann, A. Kubetzka, O. Pietzsch, and R. Wiesendanger, "Interface-induced chiral domain walls, spin spirals and skyrmions revealed by spin-polarized scanning tunneling microscopy," *Journal of Physics: Condensed Matter*, no. 26, p. 394002, 2014.

[14] N. Romming, A. Kubetzka, C. Hanneken, K. von Bergmann, and R. Wiesendanger, "Field-dependent size and shape of single magnetic skyrmions," *Physical Review Letters*, no. 114, p. 177203, 2015.

[15] Y. Tchoe and J. H. Han, "Skyrmion generation by current," *Physical Review B*, vol. 85, no. 17, 2012.

[16] J. Iwasaki, M. Mochizuki, and N. Nagaosa, "Current-induced skyrmion dynamics in constricted geometries," *Nature Nanotechnology*, vol. 8, no. 10, pp. 742–747, 2013.

[17] M. Finazzi, M. Savoini, A. R. Khorsand, A. Tsukamoto, A. Itoh, L. Duò, A. Kirilyuk, T. Rasing, and M. Ezawa, "Laser-induced magnetic nanostructures with tunable topological properties," *Physical Review Letters*, vol. 110, no. 17, 2013.

[18] M. Ezawa, "Giant skyrmions stabilized by dipole-dipole interactions in thin ferromagnetic films," *Physical Review Letters*, vol. 105, no. 19, 2010.

[19] Y. Zhou and M. Ezawa, "A reversible conversion between a skyrmion and a domain-wall pair in a junction geometry," *Nature communications*, vol. 5, p. 4652, 2014.

[20] J. Iwasaki, A. J. Beekman, and N. Nagaosa, "Theory of magnon-skyrmion scattering in chiral magnets," *Physical Review B*, vol. 89, no. 6, 2014.

[21] O. Boulle, L. D. Buda-Prejbeanu, E. Jué, I. M. Miron, and G. Gaudin, "Current induced domain wall dynamics in the presence of spin orbit torques," *Journal of Applied Physics*, vol. 115, no. 17, p. 17D502, 2014.

[22] S. Rohart and A. Thiaville, "Skyrmion confinement in ultrathin film nanostructures in the presence of Dzyaloshinskii-Moriya interaction," *Physical Review B*, vol. 88, no. 18, 2013.

[23] R. Tomasello, E. Martinez, R. Zivieri, L. Torres, M. Carpentieri, and G. Finocchio, "A strategy for the design of skyrmion racetrack memories," *Scientific reports*, vol. 4, p. 6784, 2014.

[24] X. Zhang, G. P. Zhao, H. Fangohr, J. P. Liu, W. X. Xia, J. Xia, and F. J. Morvan, "Skyrmion-skyrmion and skyrmion-edge repulsions in skyrmion-based racetrack memory," *Scientific reports*, vol. 5, p. 7643, 2015.

[25] J. Iwasaki, M. Mochizuki, and N. Nagaosa, "Universal current-velocity relation of skyrmion motion in chiral magnets," *Nature communications*, vol. 4, p. 1463, 2013.

[26] C. Hanneken, F. Otte, A. Kubetzka, B. Dupé, N. Romming, K. von Bergmann, R. Wiesendanger, and S. Heinze, "Electrical detection of magnetic skyrmions by tunneling non-collinear magnetoresistance," *Nature Nanotechnology*, vol. 10, pp. 1039–1042, 2015.

[27] K. von Bergmann, M. Menzel, D. Serrate, Y. Yoshida, S. Schröder, P. Ferriani, A. Kubetzka, R. Wiesendanger, and S. Heinze, "Tunneling anisotropic magnetoresistance on the atomic scale," *Physical Review B*, vol. 86, no. 13, 2012.

[28] A. N. Bogdanov and U. K. Rößler, "Chiral symmetry breaking in magnetic thin films and multilayers," *Physical Review Letters*, vol. 87, no. 3, p. 037203, 2001.

[29] T. H. R. Skyrme, "A non-linear theory of strong interactions," *Proceedings of the Royal Society A: Mathematical, Physical and Engineering Sciences*, vol. 247, no. 1249, pp. 260–278, 1961.

[30] T. H. R. Skyrme, "A unified field theory of mesons and baryons," *Nuclear Physics*, vol. 31, no. 4, p. 556, 1962.

[31] U. Al Khawaja and H. Stoof, "Skyrmions in a ferromagnetic Bose-Einstein condensate," *Nature*, vol. 411, no. 6840, pp. 918–920, 2001.

[32] L. Brey, H. A. Fertig, R. Côté, and A. H. MacDonald, "Skyrme crystal in a two-dimensional electron gas," *Physical Review Letters*, vol. 75, no. 13, pp. 2562–2565, 1995.

[33] R. Durrer, M. Kunz, and A. Melchiorri, "Cosmic structure formation with topological defects," *Physics Reports*, vol. 364, no. 1, pp. 1–81, 2002.

[34] W. Muenzer, A. Neubauer, T. Adams, S. Muehlbauer, C. Franz, F. Jonietz, R. Georgii, P. Böni, B. Pedersen, M. Schmidt, A. Rosch, and C. Pfleiderer, "Skyrmion lattice in the doped semiconductor $Fe_{1-x}Co_xSi$," *Physical Review B*, vol. 81, no. 4, p. 041203, 2010.

[35] X. Yu, N. Kanazawa, Y. Onose, K. Kimoto, W. Z. Zhang, S. Ishiwata, Y. Matsui, and Y. Tokura, "Near room-temperature formation of a skyrmion crystal in thin-films of the helimagnet FeGe," *Nature Materials*, vol. 10, no. 2, pp. 106–109, 2011.

[36] H. Du, J. P. DeGrave, F. Xue, D. Liang, W. Ning, J. Yang, M. Tian, Y. Zhang, and S. Jin, "Highly stable skyrmion state in helimagnetic MnSi nanowires," *Nano Letters*, vol. 14, no. 4, pp. 2026–2032, 2014.

[37] L. Sun, R. X. Cao, B. F. Miao, Z. Feng, B. You, D. Wu, W. Zhang, A. Hu, and H. F. Ding, "Creating an artificial two-dimensional skyrmion crystal by nanopatterning," *Physical Review Letters*, vol. 110, no. 16, 2013.

[38] Y. Y. Dai, H. Wang, P. Tao, T. Yang, W. J. Ren, and Z. D. Zhang, "Skyrmion ground state and gyration of skyrmions in magnetic nanodisks without the Dzyaloshinsky-Moriya interaction," *Physical Review B*, vol. 88, no. 5, 2013.

[39] M. Mochizuki, X. Z. Yu, S. Seki, N. Kanazawa, W. Koshibae, J. Zang, M. Mostovoy, Y. Tokura, and N. Nagaosa, "Thermally driven ratchet motion of a skyrmion microcrystal and topological magnon hall effect," *Nature Materials*, vol. 13, no. 3, pp. 241–246, 2014.

[40] B. F. Miao, L. Sun, Y. W. Wu, X. D. Tao, X. Xiong, Y. Wen, R. X. Cao, P. Wang, D. Wu, Q. F. Zhan, B. You, J. Du, R. W. Li, and H. F. Ding, "Experimental realization of two-dimensional artificial skyrmion crystals at room temperature," *Physical Review B*, vol. 90, no. 17, 2014.

[41] G. E. Brown and M. Rho, *The multifaceted skyrmion.* Hackensack, N.J: World Scientific, 2010.

[42] S. S. Parkin, M. Hayashi, and L. Thomas, "Magnetic domain-wall racetrack memory," *Science*, vol. 320, no. 5873, pp. 190–194, 2008.

[43] F. Jonietz, S. Muehlbauer, C. Pfleiderer, A. Neubauer, W. Muenzer, A. Bauer, T. Adams, R. Georgii, P. Boeni, R. A. Duine, K. Everschor, M. Garst, and A. Rosch, "Spin transfer torques in MnSi at ultralow current densities," *Science*, vol. 330, no. 6011, pp. 1648–1651, 2010.

[44] C. Pappas, E. Lelièvre-Berna, P. Falus, P. M. Bentley, E. Moskvin, S. Grigoriev, P. Fouquet, and B. Farago, "Chiral paramagnetic skyrmion-like phase in MnSi," *Physical Review Letters*, vol. 102, no. 19, p. 197202, 2009.

[45] A. Neubauer, C. Pfleiderer, B. Binz, A. Rosch, R. Ritz, P. G. Niklowitz, and P. Böni, "Topological hall effect in the a phase of MnSi," *Physical Review Letters*, vol. 102, no. 18, p. 186602, 2009.

[46] H. S. Park, X. Yu, S. Aizawa, T. Tanigaki, T. Akashi, Y. Takahashi, T. Matsuda, N. Kanazawa, Y. Onose, D. Shindo, A. Tonomura, and Y. Tokura, "Observation of the magnetic flux and three-dimensional structure of skyrmion lattices by electron holography," *Nature Nanotechnology*, vol. 9, no. 5, pp. 337–342, 2014.

[47] S. X. Huang and C. L. Chien, "Extended skyrmion phase in epitaxial FeGe(111) thin films," *Physical Review Letters*, vol. 108, no. 26, p. 267201, 2012.

[48] K. Shibata, X. Yu, T. Hara, D. Morikawa, N. Kanazawa, K. Kimoto, S. Ishiwata, Y. Matsui, and Y. Tokura, "Towards control of the size and helicity of skyrmions in helimagnetic alloys by spin–orbit coupling," *Nature Nanotechnology*, vol. 8, no. 10, pp. 723–728, 2013.

[49] S. Seki, X. Yu, S. Ishiwata, and Y. Tokura, "Observation of skyrmions in a multiferroic material," *Science*, vol. 336, no. 6078, pp. 198–201, 2012.

[50] X. Yu, J. P. DeGrave, Y. Hara, T. Hara, S. Jin, and Y. Tokura, "Observation of the magnetic skyrmion lattice in a MnSi nanowire by Lorentz TEM," *Nano Letters*, vol. 13, no. 8, pp. 3755–3759, 2013.

[51] X. Yu, N. Kanazawa, W. Z. Zhang, T. Nagai, T. Hara, K. Kimoto, Y. Matsui, Y. Onose, and Y. Tokura, "Skyrmion flow near room temperature in an ultralow current density," *Nature Communications*, vol. 3, p. 988, 2012.

[52] I. Dzyaloshinsky, "A thermodynamic theory of weak ferromagnetism of antiferromagnetics," *Journal of Physics and Chemistry of Solids*, vol. 4, no. 4, pp. 241–255, 1958.

[53] T. Moriya, "Anisotropic superexchange interaction and weak ferromagnetism," *Physical Review*, vol. 120, no. 1, pp. 91–98, 1960.

[54] U. K. Roessler, A. N. Bogdanov, and C. Pfleiderer, "Spontaneous skyrmion ground states in magnetic metals," *Nature*, vol. 442, no. 7104, pp. 797–801, 2006.

[55] M. N. Baibich, J. M. Broto, A. Fert, Van Dau, F. Nguyen, F. Petroff, P. Etienne, G. Creuzet, A. Friederich, and J. Chazelas, "Giant magnetoresistance of (001)Fe/(001)Cr magnetic superlattices," *Physical Review Letters*, vol. 61, no. 21, pp. 2472–2475, 1988.

[56] G. Binasch, P. Grünberg, F. Saurenbach, and W. Zinn, "Enhanced magnetoresistance in layered magnetic structures with antiferromagnetic interlayer exchange," *Physical Review B*, vol. 39, no. 7, pp. 4828–4830, 1989.

[57] M. Jullière, "Tunneling between ferromagnetic films," *Phys. Lett. A*, no. 54, p. 225, 1975.

[58] R. Wiesendanger, H. J. Guntherodt, G. Guntherodt, R. J. Gambino, and R. Ruf, "Observation of vacuum tunneling of spin-polarized electrons with the scanning tunneling microscope," *Physical Review Letters*, vol. 65, no. 2, pp. 247–250, 1990.

[59] T. R. McGuire and R. I. Potter, "Anisotropic magnetoresistance in ferromagnetic 3d alloys," *IEEE Trans. Magn*, no. 11, p. 1018, 1975.

[60] M. Bode, S. Heinze, A. Kubetzka, O. Pietzsch, X. Nie, G. Bihlmayer, S. Blügel, and R. Wiesendanger, "Magnetization-direction-dependent local electronic structure probed by scanning tunneling spectroscopy," *Physical Review Letters*, vol. 89, no. 23, p. 237205, 2002.

[61] C. Gould, C. Rüster, T. Jungwirth, E. Girgis, G. M. Schott, R. Giraud, K. Brunner, G. Schmidt, and L. W. Molenkamp, "Tunneling anisotropic magnetoresistance: A spin-valve-like tunnel magnetoresistance using a single magnetic layer," *Physical Review Letters*, vol. 93, no. 11, p. 117203, 2004.

[62] P. M. Levy and S. Zhang, "Resistivity due to domain wall scattering," *Physical Review Letters*, vol. 79, no. 25, pp. 5110–5113, 1997.

[63] A. D. Kent, J. Yu, U. Rüdiger, and Parkin, S S P, "Domain wall resistivity in epitaxial thin film microstructures," *Journal of Physics: Condensed Matter*, vol. 13, no. 25, pp. R461–R488, 2001.

[64] C. H. Marrows and B. C. Dalton, "Spin mixing and spin-current asymmetry measured by domain wall magnetoresistance," *Physical Review Letters*, vol. 92, no. 9, p. 97206, 2004.

[65] K. M. Seemann, F. Garcia-Sanchez, F. Kronast, J. Miguel, A. Kákay, C. M. Schneider, R. Hertel, F. Freimuth, Y. Mokrousov, and S. Blügel, "Disentangling the physical contributions to the electrical resistance in magnetic domain walls: A multiscale study," *Physical Review Letters*, vol. 108, no. 7, p. 77201, 2012.

[66] K. von Bergmann, S. Heinze, M. Bode, G. Bihlmayer, S. Blügel, and R. Wiesendanger, "Complex magnetism of the Fe monolayer on Ir(111)," *New Journal of Physics*, vol. 9, no. 10, p. 396, 2007.

[67] R. Wiesendanger, *Scanning Probe Microscopy and Spectroscopy - Methods and Applications*. Cambridge University Press, 1994.

[68] C. J. Chen, *Introduction to Scanning Tunneling Microscopy*. Oxford University Press, 1993.

[69] N. D. Lang, "Spectroscopy of single atoms in the scanning tunneling microscope," *Physical Review B*, vol. 34, no. 8, pp. 5947–5950, 1986.

[70] Y. Hasegawa and P. Avouris, "Direct observation of standing wave formation at surface steps using scanning tunneling spectroscopy," *Physical Review Letters*, vol. 71, no. 7, pp. 1071–1074, 1993.

[71] M. Bode, S. Heinze, A. Kubetzka, O. Pietzsch, M. Hennefarth, M. Getzlaff, R. Wiesendanger, X. Nie, G. Bihlmayer, and S. Blügel, "Structural, electronic, and magnetic properties of a Mn monolayer on W(110)," *Physical Review B*, vol. 66, no. 1, p. 014425, 2002.

[72] K. von Bergmann, S. Heinze, M. Bode, E. Vedmedenko, G. Bihlmayer, S. Blügel, and R. Wiesendanger, "Observation of a complex nanoscale magnetic structure in a hexagonal Fe monolayer," *Physical Review Letters*, vol. 96, no. 16, p. 167203, 2006.

[73] S. Meckler, N. Mikuszeit, A. Preßler, E. Y. Vedmedenko, O. Pietzsch, and R. Wiesendanger, "Real-space observation of a right-rotating inhomogeneous cycloidal spin spiral by spin-polarized scanning tunneling microscopy in a triple axes vector magnet," *Physical Review Letters*, vol. 103, no. 15, 2009.

[74] A. Wachowiak, J. Wiebe, M. Bode, O. Pietzsch, M. Morgenstern, and R. Wiesendanger, "Direct observation of internal spin structure of magnetic vortex cores," *Science (New York, N.Y.)*, vol. 298, no. 5593, pp. 577–580, 2002.

[75] R. Wiesendanger, "Spin mapping at the nanoscale and atomic scale," *Reviews of Modern Physics*, vol. 81, no. 4, pp. 1495–1550, 2009.

[76] A. Kubetzka, O. Pietzsch, M. Bode, R. Ravlic, and R. Wiesendanger, "Spin-polarized STM investigation of magnetic domain walls," *Acta Physica Polonica A*, vol. 104, no. 3-4, 2003.

[77] R. Wiesendanger, H. J. Guntherodt, G. Guntherodt, R. J. Gambino, and R. Ruf, "Measurement of the local electron-spin polarization by the scanning tunneling microscope," *Helvetica Physica Acta*, vol. 63, no. 6, pp. 778–782, 1990.

[78] R. Wiesendanger, H. J. Guntherodt, G. Guntherodt, R. J. Gambino, and R. Ruf, "Scanning tunneling microscopy with spin-polarized electrons," *Zeitschrift Fur Physik B-condensed Matter*, vol. 80, no. 1, pp. 5–6, 1990.

[79] M. Menzel, Y. Mokrousov, R. Wieser, J. E. Bickel, E. Vedmedenko, S. Blügel, S. Heinze, K. von Bergmann, A. Kubetzka, and R. Wiesendanger, "Information transfer by vector spin chirality in finite magnetic chains," *Physical Review Letters*, vol. 108, no. 19, p. 197204, 2012.

[80] D. M. Eigler and E. K. Schweizer, "Positioning single atoms with a scanning tunnelling microscope," *Nature*, vol. 344, no. 6266, pp. 524–526, 1990.

[81] H. C. Manoharan, C. P. Lutz, and D. M. Eigler, "Quantum mirages formed by coherent projection of electronic structure," *Nature*, vol. 403, no. 6769, pp. 512–515, 2000.

[82] C. F. Hirjibehedin, "Spin coupling in engineered atomic structures," *Science*, vol. 312, no. 5776, pp. 1021–1024, 2006.

[83] D. Serrate, P. Ferriani, Y. Yoshida, S.-W. Hla, M. Menzel, K. von Bergmann, S. Heinze, A. Kubetzka, and R. Wiesendanger, "Imaging and manipulating the spin direction of individual atoms," *Nature Nanotechnology*, vol. 5, no. 5, pp. 350–353, 2010.

[84] A. A. Khajetoorians, J. Wiebe, B. Chilian, and R. Wiesendanger, "Realizing all-spin-based logic operations atom by atom," *Science*, vol. 332, no. 6033, pp. 1062–1064, 2011.

[85] A. A. Khajetoorians, J. Wiebe, B. Chilian, S. Lounis, S. Blügel, and R. Wiesendanger, "Atom-by-atom engineering and magnetometry of tailored nanomagnets," *Nature Physics*, vol. 8, no. 6, pp. 497–503, 2012.

[86] H. J. Lee, "Single-bond formation and characterization with a scanning tunneling microscope," *Science*, vol. 286, no. 5445, pp. 1719–1722, 1999.

[87] S.-W. Hla, L. Bartels, G. Meyer, and K.-H. Rieder, "Inducing all steps of a chemical reaction with the scanning tunneling microscope tip: Towards single molecule engineering," *Physical Review Letters*, vol. 85, no. 13, pp. 2777–2780, 2000.

[88] J. R. Hahn and W. Ho, "Oxidation of a single carbon monoxide molecule manipulated and induced with a scanning tunneling microscope," *Physical Review Letters*, vol. 87, no. 16, 2001.

[89] A. A. Khajetoorians, B. Baxevanis, C. Hübner, T. Schlenk, S. Krause, T. O. Wehling, S. Lounis, A. Lichtenstein, D. Pfannkuche, J. Wiebe, and R. Wiesendanger, "Current-driven spin dynamics of artificially constructed quantum magnets," *Science*, vol. 339, no. 6115, pp. 55–59, 2013.

[90] B. Bryant, A. Spinelli, Wagenaar, J. J. T., M. Gerrits, and A. F. Otte, "Local control of single atom magnetocrystalline anisotropy," *Physical Review Letters*, vol. 111, no. 12, 2013.

[91] A. Spinelli, B. Bryant, F. Delgado, J. Fernández-Rossier, and A. F. Otte, "Imaging of spin waves in atomically designed nanomagnets," *Nature Materials*, vol. 13, no. 8, pp. 782–785, 2014.

[92] S. Loth, M. Etzkorn, C. P. Lutz, D. M. Eigler, and A. J. Heinrich, "Measurement of fast electron spin relaxation times with atomic resolution," *Science*, vol. 329, no. 5999, pp. 1628–1630, 2010.

[93] S. Loth, C. P. Lutz, and A. J. Heinrich, "Spin-polarized spin excitation spectroscopy," *New Journal of Physics*, vol. 12, no. 12, p. 125021, 2010.

[94] S. Loth, S. Baumann, C. P. Lutz, D. M. Eigler, and A. J. Heinrich, "Bistability in atomic-scale antiferromagnets," *Science*, vol. 335, no. 6065, pp. 196–199, 2012.

[95] S. Blundell, *Magnetism in Condensed Matter*. Oxford Master Series in Condensed Matter Physics, Oxford: Oxford University Press, 2001.

[96] N. W. Ashcroft and N. D. Mermin, *Solid state physics*. South Melbourne: Brooks/Cole Thomson Learning, repr ed., 2012.

[97] A. Fert and P. A. Levy, "Role of anisotropic exchange interactions in determining the properties of spin glasses.," *Physical Review Letters*, no. 44, pp. 1538–1541, 1980.

[98] A. Butenko, *Phenomenological theory of chiral states in magnets with Dzyaloshinskii-Moriya*. PhD thesis, 2013.

[99] W. Nolting and A. Ramakanth, *Quantum Theory of Magnetism*. Berlin, Heidelberg: Springer Berlin Heidelberg, 2009.

[100] G. Binnig and H. Rohrer, "Scanning tunneling microscopy," *Helvetica Physica Acta*, vol. 55, no. 6, pp. 726–735, 1982.

[101] J. Bardeen, "Tunnelling from a many-particle point of view," *Physical Review Letters*, vol. 6, no. 2, pp. 57–&, 1961.

[102] J. Tersoff and D. R. Hamann, "Theory and application for the scanning tunneling microscope," *Physical Review Letters*, vol. 50, no. 25, pp. 1998–2001, 1983.

[103] J. Tersoff and D. R. Hamann, "Theory of the scanning tunneling microscope," *Physical Review B*, vol. 31, no. 2, pp. 805–813, 1985.

[104] C. J. Chen, "Theory of scanning tunneling spectroscopy," *Journal of Vacuum Science & Technology A-vacuum Surfaces and Films*, vol. 6, no. 2, pp. 319–322, 1988.

[105] C. J. Chen, "Origin of atomic resolution on metal surfaces in scanning tunneling microscopy," *Physical Review Letters*, vol. 65, no. 4, pp. 448–451, 1990.

[106] S. Heinze, "Simulation of spin-polarized scanning tunneling microscopy images of nanoscale non-collinear magnetic structures," *Applied Physics A-materials Science & Processing*, vol. 85, no. 4, pp. 407–414, 2006.

[107] S. S. Parkin, C. Kaiser, A. Panchula, P. M. Rice, B. Hughes, M. Samant, and S.-H. Yang, "Giant tunnelling magnetoresistance at room temperature with MgO(100) tunnel barriers," *Nature Materials*, vol. 3, no. 12, pp. 862–867, 2004.

[108] R. Wiesendanger, I. V. Shvets, D. Bürgler, G. Tarrach, H.-J. Guntherodt, and Coey, J. M. D., "Magnetic imaging at the atomic level," *Z. Physik B - Condensed Matter (Zeitschrift für Physik B Condensed Matter)*, vol. 86, no. 1, pp. 1–2, 1992.

[109] D. Wortmann, S. Heinze, P. Kurz, G. Bihlmayer, and S. Blügel, "Resolving complex atomic-scale spin structures by spin-polarized scanning tunneling microscopy," *Physical Review Letters*, vol. 86, no. 18, pp. 4132–4135, 2001.

[110] M. Menzel, *Non-collinear magnetic ground states observed in Iron Nanostructures on Iridium Surfaces*. PhD thesis, University of Hamburg, Hamburg, Germany, 2011.

[111] A. Kubetzka, O. Pietzsch, M. Bode, and R. Wiesendanger, "Determining the spin polarization of surfaces by spin-polarized scanning tunneling spectroscopy," *Applied Physics A-materials Science & Processing*, vol. 76, no. 6, pp. 873–877, 2003.

[112] S.-W. Hla, "Scanning tunneling microscopy single atom/molecule manipulation and its application to nanoscience and technology," *Journal of Vacuum Science & Technology B: Microelectronics and Nanometer Structures*, vol. 23, no. 4, p. 1351, 2005.

[113] J. A. Stroscio and D. M. Eigler, "Atomic and molecular manipulation with the scanning tunneling microscope," *Science (New York, N.Y.)*, vol. 254, no. 5036, pp. 1319–1326, 1991.

[114] L. Bartels, G. Meyer, and K.-H. Rieder, "Basic steps of lateral manipulation of single atoms and diatomic clusters with a scanning tunneling microscope tip," *Physical Review Letters*, vol. 79, no. 4, pp. 697–700, 1997.

[115] N. Romming, "Einfluss nicht-magnetischer adlagen auf nicht-kollineare magnetische zustände," Master's thesis, University of Hamburg, Hamburg, Germany, 2013.

[116] N. Yoshimura, *Vacuum Technology: Practice for Scientific Instruments*. Berlin, Heidelberg: Springer-Verlag Berlin Heidelberg, 2008.

[117] Scienta Omicron GmbH, Limburger Strasse 75, 65232 Taunusstein, Germany, 2015.

[118] A. Kubetzka, M. Bode, O. Pietzsch, and R. Wiesendanger, "Spin-polarized scanning tunneling microscopy with antiferromagnetic probe tips," *Physical Review Letters*, vol. 88, no. 5, p. 057201, 2002.

[119] A. Schlenhoff, S. Krause, G. Herzog, and R. Wiesendanger, "Bulk Cr tips with full spatial magnetic sensitivity for spin-polarized scanning tunneling microscopy," *Applied Physics Letters*, vol. 97, no. 8, p. 083104, 2010.

[120] O. Pietzsch, A. Kubetzka, D. Haude, M. Bode, and R. Wiesendanger, "A low-temperature ultrahigh vacuum scanning tunneling microscope with a split-coil magnet and a rotary motion stepper motor for high spatial resolution studies of surface magnetism," *Review of Scientific Instruments*, vol. 71, no. 2, p. 424, 2000.

[121] SPECS Zurich GmbH, Technoparkstrasse 1, 8005 Zurich, Switzerland, 2015.

[122] MaTecK GmbH, Im Langenbroich 20, 52428 Juelich, Germany, 2015.

[123] Surepure Chemetals Inc., 5 Nottingham Drive, Florham Park, NJ 07932, USA, 2015.

[124] tectra GmbH Physikalische Instrumente, Reuterweg 65, D-60323 Frankfurt/M, Germany, 2015.

[125] F. Otte, *Electronic structure theory of magnetoresistive effects in atomic-scale junctions induced by spin-orbit coupling and spin non-collinearity.* PhD thesis, Christian-Albrechts-Universität zu Kiel, Kiel, Germany, 2016.

[126] Institute of Theoretical Physics and Astrophysics, University of Kiel, Leibnizstr. 15, D-24098 Kiel, Germany, 2015.

[127] W. Kohn, *Statistik: Datenanalyse und Wahrscheinlichkeitsrechnung.* Statistik und ihre Anwendungen, Berlin, Heidelberg: Springer-Verlag Berlin Heidelberg, 2005.

[128] O. Pietzsch, A. Kubetzka, M. Bode, and R. Wiesendanger, "Spin-polarized scanning tunneling spectroscopy of nanoscale cobalt islands on Cu(111)," *Physical Review Letters*, vol. 92, no. 5, 2004.

[129] O. Pietzsch, S. Okatov, A. Kubetzka, M. Bode, S. Heinze, A. Lichtenstein, and R. Wiesendanger, "Spin-resolved electronic structure of nanoscale cobalt islands on Cu(111)," *Physical Review Letters*, vol. 96, no. 23, 2006.

[130] A. Kubetzka, *Spinpolarisierte Rastertunnelmikroskopie an magnetischen Nanostrukturen: Fe\W(110).* PhD thesis, University of Hamburg, Hamburg, Germany, 2002.

[131] A. Kubetzka, O. Pietzsch, M. Bode, and R. Wiesendanger, "Spin-polarized scanning tunneling microscopy study of 360 degrees walls in an external magnetic field," *Physical Review B*, vol. 67, no. 2, p. 020401, 2003.

[132] K. von Bergmann, M. Menzel, A. Kubetzka, and R. Wiesendanger, "Influence of the local atom configuration on a hexagonal skyrmion lattice," *Nano Letters*, vol. 15, no. 5, pp. 3280–3285, 2015.

Publications

Publications

Electrical detection of magnetic skyrmions by tunneling non-collinear magnetoresistance
C. Hanneken, F. Otte, A. Kubetzka, B. Dupé, N. Romming, K. von Bergmann, R. Wiesendanger, and S. Heinze
Nature Nanotechnology **10** 1039-1042 (2015)

Field-dependent size and shape of single magnetic skyrmions
N. Romming, A. Kubetzka, C. Hanneken, K. von Bergmann, and R. Wiesendanger
Phys. Rev. Lett. **114** 177203 (2015)

Magnetische Knoten auf der Festplatte
C. Hanneken, and N. Romming
Spektrum der Wissenschaft **Okt. 2013** 22 (2013)

Writing and deleting single magnetic skyrmions
N. Romming, C. Hanneken, M. Menzel, J. E. Bickel, B. Wolter, K. von Bergmann, A. Kubetzka, and R. Wiesendanger
Science **341** 6146 (2013)

Contributed talks

Writing and deleting single magnetic skyrmions
C. Hanneken, N. Romming, M. Menzel, J. E. Bickel, B. Wolter, K. von Bergmann, A. Kubetzka, and R. Wiesendanger
ICN+T, 2014 Vail (CO), USA

Poster

Spatial variation of a skyrmion's electronic band structure observed with scanning tunneling spectroscopy
C. Hanneken, N. Romming, K. von Bergmann, A. Kubetzka, and R. Wiesendanger
ICN+T 2014, Vail (CO), USA

Spatial variation of a skyrmion's electronic band structure observed with scanning tunneling spectroscopy
C. Hanneken, N. Romming, K. von Bergmann, A. Kubetzka, and R. Wiesendanger
SP-STM 2014, Huron (OH), USA

Spatial variation of a skyrmion's electronic band structure observed with scanning tunneling spectroscopy
C. Hanneken, N. Romming, K. von Bergmann, A. Kubetzka, and R. Wiesendanger
SKYMAG 2014, Paris, France

Recent developments in the manipulation of single magnetic skyrmions by SP-STM
C. Hanneken, N. Romming, M. Menzel, J. E. Bickel, B. Wolter, K. von Bergmann, A. Kubetzka, and R. Wiesendanger
544. WEH-Seminar 2013, Bad Honnef, Germany

Chromium bulk tips for spin-polarized scanning tunneling microscopy
C. Hanneken, A. Kubetzka, K. von Bergmann, S.-W. Hla, and R. Wiesendanger
SP-STM 12 SP-STS 8 2012, Timmendorfer Strand, Germany

Chromium bulk tips for spin-polarized scanning tunneling microscopy
C. Hanneken, A. Kubetzka, K. von Bergmann, and R. Wiesendanger
DPG 2012, Berlin, Germany

Acknowledgements

As the custom is, I would like to thank several persons without whom this work would not have been possible:

- Prof. Dr. Dr. h.c. Prof. h.c. Roland Wiesendanger for the possibility to do my PhD thesis in one of the top groups in the field of nanomagnetism,
- Dr. Kirsten von Bergmann and Dr. André Kubetzka for their scientific and moral support, many fruitful discussions and constructive criticism,
- Fabian Otte, Dr. Bertrand Dupé and Prof. Dr. Stefan Heinze for insightful discussions,
- Niklas Romming for his moral support and the great time at conferences and in the lab,
- all colleagues of Lab013 for the help I received during my work,
- everyone in Group R for a friendly working atmosphere,
- Andrea Beese, Sigrid Schmidtke, Ute Brenger, Norbert Dix and Michael Langer for their excellent support in administrative and technical questions,
- the DFG via SFB 668 and Graduiertenkolleg 1286,
- both teams in the mechanical and the electronic workshop for their excellent and uncomplicated support,
- the Helium team for always supplying me with liquid helium, even on a short notice,
- allen guten Geistern der Verwaltung der Universität Hamburg, die jeden Tag voller Elan und Freude Studenten und Mitarbeiter in ihrer Arbeit nach Kräften unterstützen,
- all friends for supporting me,
- my family, especially my parents Martina and Hubert for their moral support and confidence during the time of my studies,
- and Lynni.

Thank you all.

Eidesstattliche Versicherung gemäß §7 (4) MIN-PromO

Hiermit erkläre ich an Eides statt, dass ich die vorliegende Dissertationsschrift selbst verfasst und keine anderen als die angegebenen Quellen und Hilfsmittel benutzt habe.

Ort, Datum

Unterschrift